Investigating the current/voltage/power/stability capabilities of enzyme-based membrane-less hydrogen fuel cells

A thesis submitted to the Board of the Faculty of Physical
Sciences, for the degree of Doctor of Philosophy,
University of Oxford

Lang Xu

St. John’s College

Trinity Term 2014

To My Parents

Abstract

Fuel cell is a device that can directly convert chemical energy into electrical energy. For low-temperature fuel cells, catalysts are required. Fuel cells using Pt-based or other non-biological materials as catalysts are known as conventional fuel cells. Inspired from Nature, enzymes can be used as catalysts in fuel cells known as enzyme-based fuel cells. The conventional and enzymatic fuel cells share the same underlying electrochemical principles, while enzyme-based fuel cells have their intrinsic advantages and disadvantages due to enzyme properties. The objective of this thesis is to investigate the current/voltage/power/stability capabilities of enzyme-based membrane-less H_2 fuel cells in order to design the enzymatic fuel cells with improved performance.

This thesis presents a facile, effective method for the construction of 3D porous carbon electrodes. The 3D porous carbon electrodes are constructed by compacting suitable carbon nanomaterials into discs. The 3D porous carbon electrodes, with large roughness, high specific surface area, and optimized pore size distribution, are able to increase the loading density of enzymes, that is, reaction sites per unit geometric electrode area. The high loading density of enzymes can result in the high current/power density of the enzyme-based membrane-less H_2 fuel cells. Moreover, the large enzyme loading can bring about the improvement in fuel cell stability because current becomes limited by mass transport of dissolved gases rather than enzyme immobilization so that neither inactivation nor desorption of enzymes would influence the current output. Based on one type of 3D porous carbon electrodes, the maximum power density of enzyme-based membrane-less

H_2 fuel cells has increased to the mW·cm^{-2} level by at least one order of magnitude and the half-life has also increased from several hours to one week.

This thesis presents a method for the increase in power density otherwise limited by low cathodic currents due to meagre O_2 in non-explosive H_2-rich H_2-air mixtures. The power density of enzyme-based membrane-less H_2 fuel cells can be increased by re-proportioning cathode/anode geometric area ratio to balance the cathodic and anodic currents under such an unusual H_2-air mixture.

This thesis also demonstrates that the 3D porous carbon electrode can improve the apparent O_2 tolerance of anodic catalysts – hydrogenases, which are very important for the fuel cell performance. The degrees of apparent O_2 tolerance for both O_2-tolerant and O_2-sensitive [NiFe]-hydrogenases are greatly increased based on the 3D porous carbon electrodes, so that even an O_2-sensitive [NiFe]-hydrogenase can be used as an anodic catalyst in the enzyme-based membrane-less H_2 fuel cell under a non-explosive H_2-rich H_2-air mixture.

This thesis presents a design of a test bed in which series and parallel connections of sandwich-like electrode stacks can be varied. The fuel cell test bed has demonstrated low-loss interconnects and efficient stack configuration. Operated under a non-explosive H_2-air mixture containing only 4.6% O_2 at 20 °C, the maximum volume power density of the fuel cell test bed exceeds 2 mW·cm^{-3}, capable of powering electronic gadgets, which is a good demonstration of electricity that originates from the buried active sites of enzymes and is transmitted by long-range electron hopping in accordance with Marcus theory.

Acknowledgements

I would like to thank my supervisor Professor Fraser Armstrong FRS for providing me with the opportunity to work in his group and letting me conduct such an interesting research into enzyme-based fuel cells. I am very grateful to him for giving me so much help, advice and support throughout my doctoral study at Oxford University.

I would also like to thank the present and past members of the Armstrong Group for many helpful discussions, especially Dr Sadagopan Krishnan, the past post-doctor in the group, who helped me with fuel cell experiments when I began my research.

I want to thank the Supergen Fuel Cell Consortium which provides excellent chances for the fellow researchers doing fuel cells or related areas to communicate and discuss with each other. The works containing in this thesis are supported by the Supergen project.

I also thank St. John's College and Chemistry Department Oxford for providing me with the travel grants for international conferences, which have benefited me a lot.

And finally, I want to express my deepest gratitude to my mother and father, who love me, nurture me, and educate me throughout my whole life. I feel very lucky and happy as my parents are never absent in every stage of my growth. Without their spiritual and material supports, I could not complete my doctoral course. Therefore, I would like to dedicate this thesis to them.

Symbols and Abbreviations

a	Activity of species
ABTS	2,2-azinobis(3-ethylbenzothiazoline-6-sulfonate)
AFC	Alkaline fuel cell
BET	Brunauer-Emmett-Teller
BJH	Barrett-Joyner-Halenda
BOD	Bilirubin oxidase from *Myrothecium verrucaria*
C^*	(Bulk) reactant concentration
CMC	Compacted mesoporous carbon
CNT	Multi-walled carbon nanotube
CPC	Compacted porous carbon
CV	Cyclic voltammogram
EPR	Electron paramagnetic resonance
FTIR	Fourier-transform infrared
G	Gibbs free energy
$\Delta G^{\ddagger}$	Free energy of activation
GT	Graphite
HOR	Hydrogen oxidation reaction
Hyd-1	Hydrogenase-1 from *E. Coli*
Hyd-2	Hydrogenase-2 from *E. Coli*
j	Current density
j_0	Exchange current density
LDR	Light dependent resistor
LED	Light-emitting device
MBH	Membrane-bound hydrogenase

MCFC	Molten carbonate fuel cell
MEA	Membrane electrode assembly
MFC	Microbial fuel cell
n	Number of moles of electrons
n_g	Number of moles of gas
OCV	Open circuit voltage
ORR	Oxygen reduction reaction
p	Pressure
PAFC	Phosphoric acid fuel cell
PEM	Proton exchange membrane
PGE	Pyrolytic graphite edge
PTFE	Polytetrafluoroethylene
S	Entropy
SHE	Standard hydrogen electrode
SOFC	Solid oxide fuel cell
T	Temperature
U	Internal energy
V	Volume
W	Work
W_e	Electrical work
WGS	Water-gas shift reaction
YSZ	Yttria-stabilized zirconia

Greek alphabets or number

α	Transfer coefficient
η_{act}	Activation overpotential

η_{conc}	Concentration overpotential
η_{ohm}	Ohmic overpotential
λ	Mean free paths
2D	Two dimensional
3D	Three dimensional

Table of Contents

Chapter 1

Fuel Cell Principles and Technologies

Abstract

This chapter introduces the fundamental principles and technologies of fuel cells, including basic fuel cell operation, thermodynamics, kinetics, charge transport, mass transport, and an overview of the major fuel cell types. Based on such basic knowledge, we can then understand how fuel cells work, how fuel cell performance is dictated, and how a good fuel cell can be designed.

1.1 Introduction

Energy is the foundation of growth and development of the national economy, and every breakthrough in energy science and technology has been exerting considerable and far-reaching influence over the productivity, social changes, and human well-being throughout history.[1,2] On the other hand, the conventional production and utilization of energy are closely connected to climate changes, global warming and air pollution caused by greenhouse gases including CO_2 and atmospheric particulate matter released by the combustion of fossil fuels which now provides >85% of the current global energy demand.[3,4] The conventional energy technologies cannot keep abreast of the efficient, economic and sustainable demands for the future's energy, thus it is necessary to develop renewable, clean energy technologies as well as improve the energy efficiency.[5-7]

Internal combustion engines have been long used for converting the chemical energy stored in a fuel into useful mechanical or electrical energy. Described by the Carnot cycle, the reversible efficiency of a combustion engine depends on the difference between the operating maximum temperature and minimum temperature (that is, increasing the operating temperature can enhance the efficiency), thus its efficiency is limited by the operating temperature.[8] Combustion engines will also produce noise, dust and harmful substances such as carbon oxides, sulphur oxides and nitrogen oxides when they operate.

Fuel cells can directly convert chemical energy into electrical energy without passing through the Carnot cycle, and the reversible efficiency of a fuel cell is given by the ratio of the Gibbs free energy change to the enthalpy change of the fuel cell reaction.[9]

Compared to combustion engines, increasing the operating temperature would reduce the reversible efficiency of fuel cells, but the fuel cell efficiency remains much higher than the combustion engine efficiency when the operation temperature is below 700 °C.[9,10] Moreover, the fuel cell can continue generating electricity with minimized emissions of the above-mentioned harmful products as long as the fuel is supplied. For example, the only product of a hydrogen fuel cell is water. Therefore, the fuel cell technology is considered as a renewable, clean and efficient method for energy conversion and electricity generation. To date, the most widely-used and the best fuel used in fuel cells is H_2.[11] As an energy carrier, H_2 reacting with O_2 in the atmosphere can allow the chemical energy stored in H_2 to be transformed into electrical energy, powering domestic appliances and automobiles.[12]

In a hydrogen fuel cell, the reaction can be divided into two electrochemical half reactions occurring at anode and cathode, respectively, shown as:

$$\text{Anode:} \qquad H_2 \rightarrow 2H^+ + 2e^- \tag{1.1}$$

$$\text{Cathode:} \qquad \tfrac{1}{2} O_2 + 2H^+ + 2e^- \rightarrow H_2O \tag{1.2}$$

$$\text{Overall cell reaction:} \qquad H_2 + \tfrac{1}{2} O_2 \rightarrow H_2O \tag{1.3}$$

Based on catalysts, H_2 undergoes the oxidation reaction at the anode, producing protons and free electrons; O_2 undergoes the reduction reaction at the cathode, consuming protons and electrons and producing water. The two electrochemical half reactions are known as the hydrogen oxidation reaction (HOR) and the oxygen reduction reaction (ORR), respectively.[13] The protons produced at the anode transfer to the cathode through the proton-conductivity, electron-insulate electrolyte, while the electrons flow to the cathode through an external circuit, making the whole reaction achieve the balance of both substances and charges and allowing external appliances to obtain electrical energy. In other words, the chemical energy is passed from the fuel (H_2) to the electrons (constituting the electric current), which are forced to flow through external circuits to do useful work by spatially separating the two half reactions by the electrolyte.

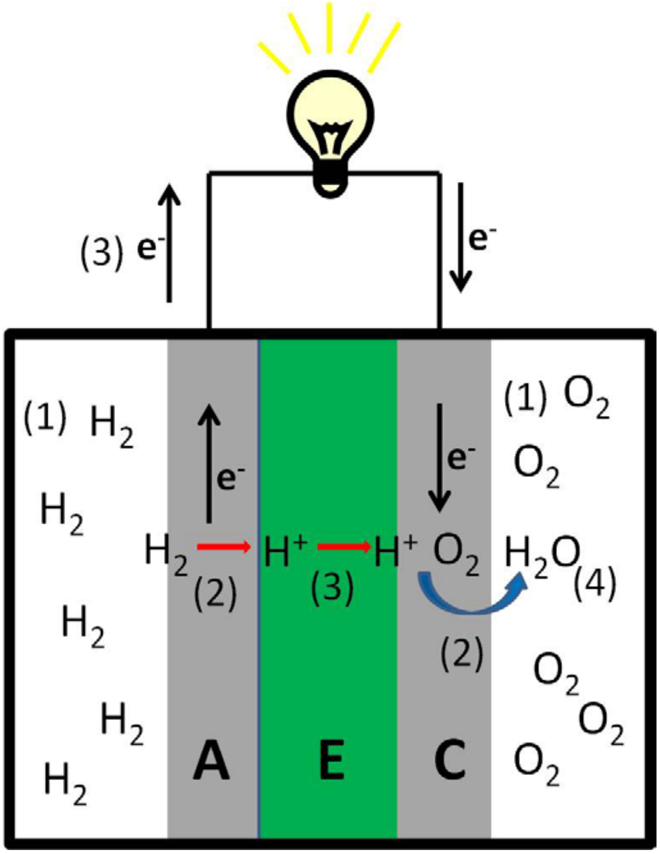

Figure 1.1. Schematic principles of operation of a hydrogen fuel cell: (1) reactant transport, (2) electrochemical reactions, (3) proton and electronic conductions, and (4) product removal. (A = Anode, E = Electrolyte, C = Cathode). Adapted from Reference 14.

Figure 1.1 shows the basic operation processes of the hydrogen fuel cell. There are four major steps in producing electricity in the fuel cell: reactant transport, electrochemical reactions, ionic/electronic conductions, and product removal.[14] *(1) Reactant transport*: H_2 and O_2 must be continuously supplied in order to generate electricity in the hydrogen fuel cell. The consumption rates of the reactants will be very fast when the fuel cell runs at high current outputs, thus the efficiency of reactant transport has an important effect on the performance of the fuel cell. Such efficiency depends upon flow-domain structures as well as physical, chemical and mechanical properties and geometries of electrodes, which need considering and optimizing when designing a fuel cell.[15-22] *(2) Electrochemical reactions*: the current produced by the fuel cell has the positive correlation with the rate of the electrochemical reactions; that is, faster electrochemical reactions lead to higher current outputs. The electrochemical reactions occurring at the interface between electrodes and electrolytes can be improved by using various kinds of catalysts.[23-29] The kinetics of electrochemical reactions will be further discussed in Section 1.3. *(3) Electronic and ionic conductions*: electrons and ions must be transported from one electrode where they are produced to the other where they are consumed in order to maintain the substance and charge balance. Ionic transport is more difficult and less efficient than electronic transport for the reason that ions are much more massive than electrons. In many cases, ions flow through the electrolyte via 'hopping' mechanisms.[30-35] Because electrodes, electrolytes and interconnectors in fuel cells have their intrinsic resistances, the electronic and ionic transport will lead to voltage loss, called the ohmic loss (η_{ohm}).[36-39] To minimize the resistance of ionic conduction, the electrolyte of the fuel cell should be as thin as possible to shorten the travel distance of ions. *(4) Product removal*: if the product of a proton exchange membrane (PEM) hydrogen fuel cell – water is not effectively removed, ‘flooding’ will occur and the electrochemical reaction rates will drop sharply.[40-44] However, for enzyme-based fuel cells, the ‘flooding’ is not a problem as the enzymatic electrodes are always dipped into aqueous electrolyte solution. Both *(1)* and *(4)* share the same principles of mass transport, which will be further discussed in Section 1.4.

1.2 Thermodynamics of fuel cells

The principles of thermodynamics provide the theoretical limits for the performance of fuel cells and any practical fuel cells work below such thermodynamic limits.[45] The maximum work output of a chemical reaction is related to the free-energy change of the reaction.[46] As most fuel cell reactions such as Equation 1.3 perform at constant temperature and pressure instead of at constant temperature and volume, Gibbs free energy (G) is a more useful term than Helmholtz free energy to describe the work potential of the system. The Gibbs free energy is defined as:

$$G = U + pV - TS \tag{1.4}$$

where U is the internal energy, p is pressure, V is volume, T is temperature, and S is entropy of a system. Since G is a function of p and T, the variation of G (dG) gives:

$$dG = dU + p\,dV + V\,dp - T\,dS - S\,dT \tag{1.5}$$

Based on the first law of thermodynamics, the term dU gives:

$$dU = T\,dS - dW \tag{1.6}$$

In the fuel cell, the work term (W) can be divided into mechanical work and electrical work (W_e), thus dU gives:

$$dU = T\,dS - (p\,dV + d\,W_e) \tag{1.7}$$

Substituting Equation 1.7 into Equation 1.5, the change in Gibbs free energy gives:

$$dG = V\,dp - S\,dT - d\,W_e \tag{1.8}$$

Under constant temperature and pressure, Equation 1.8 reduces to:

$$dG = -\,d\,W_e \tag{1.9}$$

For a fuel cell reaction using molar quantities, Equation 1.9 can be re-written as:

$$W_e = -\Delta G \tag{1.10}$$

Therefore, the maximum W_e that the fuel cell can provide is given by the negative of ΔG in the process of constant temperature and pressure. The electrical work can be expressed as:

$$W_e = nFE \tag{1.11}$$

where n is the number of moles of electrons involved, E is the reversible voltage, and F is Faraday's constant. Combining Equations 1.10 and 1.11, the reversible voltage of the fuel cell is related to the molar Gibbs free energy, shown as:

$$\Delta G = -\,nFE \tag{1.12}$$

According to the thermodynamic data under standard-state conditions (298K, 101325 Pa),[46] the ΔG values of the cell reaction (Equation 1.3) in the hydrogen fuel cell are −237 kJ/mol for liquid water product and −229 kJ/mol for gas water product, thus the reversible voltages of the fuel cell are calculated to be 1.23 V and 1.19 V, respectively, based on Equation 1.12. This means that the highest cell voltage of a hydrogen fuel cell is 1.23 V or 1.19 V.

Thermodynamic variables such as temperature, pressure and gas concentrations have considerable influence over the reversible voltage of fuel cells.[45,47,48] *(1) Temperature factor*: under a constant pressure, the relationship between ΔG and temperature can be written as:

$$(\partial \Delta G / \partial T)_p = -\Delta S \qquad (1.13)$$

Combining Equations 1.12 and 1.13 yields:

$$(\partial E / \partial T)_p = \Delta S / (nF) \qquad (1.14)$$

Equation 1.14 shows that the variation of the reversible cell voltage with temperature is related to the entropy change of the cell reactions. If the ΔS value of a cell reaction is negative, then the reversible voltages of fuel cells decrease with increasing temperature. Take the cell reaction of a hydrogen fuel cell (see Equation 1.3) as an example. According to the thermodynamic data,[46] the ΔS value of the reaction is −44.38 J/(mol K) for gas water product or −163.16 J/(mol K) for liquid water product. Integrating Equation 1.14 gives the variation of reversible voltage with temperature under constant pressure, written as:

$$E_T = E^0 + \Delta S\,(T - T_0)\,/\,(nF) \tag{1.15}$$

Thus it can be calculated that the reversible cell voltage of the hydrogen fuel cell will decrease 23 mV (for gas water product) as the temperature increases by 100 degrees. Moreover, as enzyme-based fuel cells usually work at relatively low temperature (20 – 40 °C), their reversible cell voltages will decrease 17 mV (for liquid water product) as the temperature increases by 20 degrees.

(2) Pressure factor: under a constant temperature, the relationship between the Gibbs free energy and temperature is given as:

$$(\partial \Delta G\,/\,\partial p)_T = \Delta V \tag{1.16}$$

Combining Equations 1.12 and 1.16 yields:

$$(\partial E\,/\,\partial p)_T = -\,\Delta V\,/\,(nF) \tag{1.17}$$

Equation 1.17 shows that the variation of reversible cell voltage with pressure correlates with the volume change of the cell reaction: if the volume change of the reaction is negative (*i.e.* the moles of product gases are fewer than the moles of reactant gases), such as Equation 1.3, the reversible voltage will increase with pressure.

(3) Concentration factor: the Nernst equation describes the relationship between the reversible voltages of fuel cell reactions and the activities (concentrations or gas pressures) of reactants and products.[46] In the hydrogen fuel cell, the Nernst equation for the reaction (see Equation 1.3) can be written as:

$$E = E^0 - \frac{RT}{2F}\ln\frac{\mathrm{a}_{\mathrm{H_2O}}}{\mathrm{a}_{\mathrm{H_2}}\mathrm{a}_{\mathrm{O_2}}^{1/2}} \tag{1.18}$$

where a is the activity of species. Assuming H_2 and O_2 are ideal gases, their activities can be replaced by their dimensionless partial pressures.[46] As enzyme-based fuel cells always operate below 100 °C, the liquid water is produced rather than the gas water. The activity of liquid water is usually taken as 1.[46] Thus Equation 1.18 can be re-written as:

$$E = E^0 - \frac{RT}{2F}\ln\frac{1}{p_{H_2}p_{O_2}^{1/2}} \tag{1.19}$$

It can be found that increasing the partial pressures of the reactant gases will increase the reversible voltage. For example, if a hydrogen fuel cell is pressurized to 4 atm H_2 and 6 atm air (the partial pressure of O_2 in air is 0.21) at 298 K, the reversible voltage will increase by only 19 mV; if air is replaced by pure O_2 with other conditions unchanged, then the reversible voltage will increase by 29 mV. The partial pressure of reactant gases has a small effect on the reversible voltage (mathematically originating from the logarithmic form of the pressure term), but low partial pressures (including using air instead of O_2) would lower the reaction kinetics.[48,49]

1.3 Kinetics of fuel cell reactions

The kinetics of electrochemical reactions is concerned with electron transfer processes.[50] Electrochemical reactions are heterogeneous processes because they involve the electron transfer between electrodes and reactants adjacent to the electrodes.[51] For example, both the HOR and ORR in the hydrogen fuel cell (see Equations 1.1 and 1.2) only occur at the interface between the electrode and the electrolyte. The current (number of electrons per time) produced by an electrochemical reaction is a measure of the rate of the electrochemical reaction (number of reactions per time).[50] Therefore, raising the rates of electrochemical reactions can increase the currents produced by fuel cells.

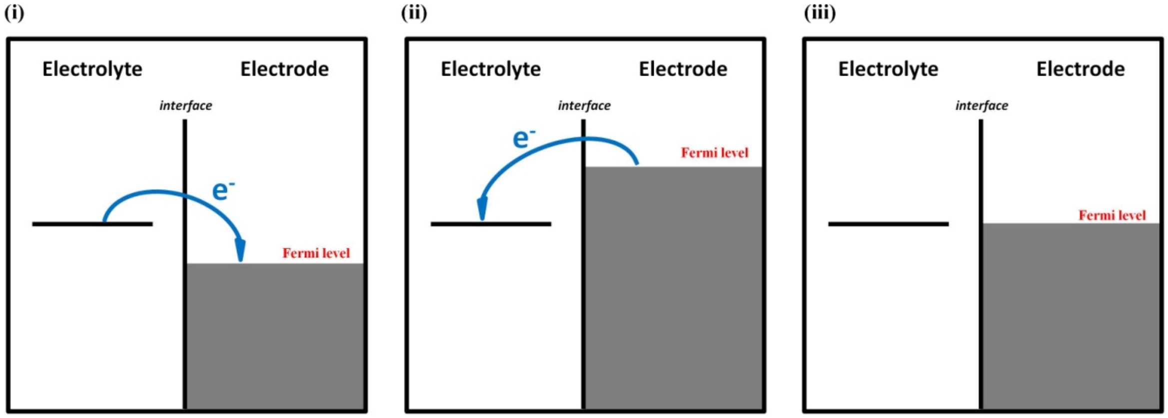

Figure 1.2. Schematic of the relationship between the directions of electron transfer and applied electrode potentials. Adapted from Reference 50.

Energy difference between electrons in an electrode and electroactive species in an electrolyte is the driving force of the electron transfer.[50] The electrode potential determines the electron energy in an electrode characterized by the Fermi level, thus controlling the direction of electron transfer and the electrochemical reaction.[51] Take the HOR (see Equation 1.1) as an example: when the electrode potential is applied more positive than the equilibrium potential of the HOR, the electrode will ‘pull’ electrons from H_2 and the forward direction of the HOR (*i.e.* the formation of protons) will be favoured, as shown in Figure 1.2(i); when the electrode potential is applied more negative than the equilibrium potential of the HOR, the electrode will 'push' electrons towards protons and the HOR will be biased towards the formation of H_2 (*i.e.* the reverse direction of the HOR), as shown in Figure 1.2(ii); when the applied electrode potential is equal to the equilibrium potential, the forward and reverse processes of the HOR will be balanced and no net electron transfer will occur, as shown in Figure 1.2(iii). Such electron transfer processes also point out that the net rate of an electrochemical reaction is given by the difference between the forward and reverse reaction rates. At thermodynamic equilibrium, there is no net current, but both the forward and reverse reactions are occurring at a rate measured by the exchange current density (j_0).[51]

One of the most important relations between current density and potential in electrochemical kinetics is the Butler-Volmer equation.[50-55] One form of the Butler-Volmer equation can be written as:[55]

$$j = j_0[\exp\left(\frac{\alpha nF\eta_{act}}{RT}\right) - \exp\left(-\frac{(1-\alpha)nF\eta_{act}}{RT}\right)] \tag{1.20}$$

where α, ranging from zero to one, is the transfer coefficient related to the symmetry of the activation barrier (for a symmetric reaction, $\alpha = 0.5$); η_{act} is the activation overpotential, representing a potential loss due to activation; j is the current density; j_0 is the exchange current density; n is the number of electrons involved in the reaction; F is the Faraday constant; R is the universal gas constant; and T is the thermodynamic temperature. Equation 1.20 also shows that the net current density is given by the difference in current density between the forward (the first term) and reverse (the second term) reactions. The Butler-Volmer equation outlines the variation of the current density produced by a fuel cell with the potential loss. For example, assuming the transfer coefficient α of a hydrogen fuel cell reaction is 0.4 at 298 K, the activation loss required to increase the forward current density to one order of magnitude as large as the exchange current density can be calculated as:

$$\frac{j_0 \exp\left(\frac{\alpha n F \eta_{act}}{RT}\right)}{j_0} = \exp\left(\frac{\alpha n F \eta_{act}}{RT}\right) = 10 \tag{1.21}$$

$$\eta_{act} = \frac{RT}{\alpha n F}\, ln 10 = \frac{8.314\times 298}{0.4\times 2\times 96500} ln 10 = 0.074\, V \tag{1.22}$$

This activation loss can also decrease the reverse current density (j_{rev}) to:

$$j_{rev} = j_0 \exp\left[-\frac{(1-\alpha) n F \eta_{act}}{RT}\right] = 0.031\, j_0 \tag{1.23}$$

The net current density gives:

$$j = 10\, j_0 - 0.031\, j_0 = 9.969\, j_0 \tag{1.24}$$

Thus an activation loss of 74 mV can increase the net current density approximately 10-fold. Likewise, an activation loss required to cause two orders-of-magnitude increase in the net current density is calculated to be 2 × 74 mV = 148 mV, showing that the lost potential is the price to increase the current density produced by the fuel cell. Moreover, the magnitude of the activation loss depends on the size of exchange current density. For example, if j_0 of the hydrogen fuel cell reaction is 10^{-6} A·cm^{-2}, increasing the net current density to 10^{-2} A·cm^{-2} requires an activation loss of 4 × 74 mV = 296 mV; if j_0 of the hydrogen fuel cell reaction is 10^{-4} A·cm^{-2}, then increasing the net current density to the same level of 10^{-2} A·cm^{-2} only requires an activation loss of 2 × 74 mV = 148 mV; that is, a higher exchange current density would cause less activation loss. Therefore, increasing j_0 is important to improve the fuel cell performance.

According to the Butler-Volmer equation (see Equation 1.20), the second exponential term (*i.e.* reverse reaction) could be neglected when the activation loss is large, shown as:

$$j = j_0 \exp\left(\frac{\alpha nF\eta_{act}}{RT}\right) \tag{1.25}$$

This simplified equation reflects the irreversible reaction process in which the forward direction of an electrochemical reaction dominates. From Equation 1.25, the activation loss gives:

$$\eta_{act} = -\frac{RT}{\alpha nF}\ln j_0 + \frac{RT}{\alpha nF}\ln j \tag{1.26}$$

Thus the transfer coefficient (α) and exchange current density (j_0) values can be obtained from the slope and intercept of a linear fit to a plot of η_{act} as a function of $\ln j$. This plot is known as the Tafel plot and Equation 1.26 is more commonly shown as:

$$\eta_{act} = a + bj \tag{1.27}$$

or

$$\eta_{act} = a + b\log j \tag{1.28}$$

which is known as the Tafel equation.[50-55] As fuel cells usually work at relatively high current densities (high activation overvoltages), the kinetics of fuel cell reactions can be approximated by the Tafel equation.

The reaction rate and experimental variables have the following relationship which can be expressed as:[56]

$$r \propto C^* \cdot \exp(-\frac{E_a}{RT}) \tag{1.29}$$

where C^* is the reactant concentration and E_a is the activation energy for the forward reaction. Therefore, to increase the forward-reaction rate and thus the net current density of a fuel cell, we need *(1) increase the reactant concentration*: owing to the linear relationship between the forward-reaction rate and the reactant concentration, increasing the reactant concentration has a large impact on the fuel cell kinetics compared with its minimal effect on the reversible voltage due to the logarithmic form of the Nernst equation (see Section 1.2); *(2) decrease the activation energy*: as the activation energy appears within an exponent, decreasing the activation energy for the forward reaction has a exponential impact on the increase in the reaction rate; a suitable catalyst can substantially decrease the activation barrier and thus massively increase the reaction rate measured by current density; and *(3) increase the temperature*: temperature also has an exponential effect on the reaction rate. Moreover, as the exchange current density (j_0) is the forward (or reverse) current density at equilibrium, j_0 has the same relationship to these variables. Therefore, such three ways to increase the net current density of a fuel cell also applies in the increase in the exchange current density. As mentioned above, increasing the exchange current density is meaningful because it can reduce the activation loss and improve the kinetic performance of fuel cells.

1.4 Fuel cell mass transport

Fuel cell mass transport, the process of supplying reactants (including fuels and oxidants) and removing products, can be divided into the two transport modes: diffusion and convection.[55,57,58] The diffusive transport dominated by the concentration gradients of reactants and products takes place in porous electrodes (known as diffusion layer), while the convective transport due to the bulk motion of fluids occurs in flow domain (outside the diffusion layer).[59,60] Figure 1.3 shows a schematic diagram of the two mass-transport modes at the porous anode and flow domain of a hydrogen fuel cell. At the flow domain, gas flow at a given rate results in the convective mixing and good distribution of H_2, so no concentration gradients form. C_{H2}^* represents the bulk H_2 concentration. Within the porous anode, the HOR results in the depletion of H_2 and thus form the concentration gradient across the diffusion layer. Such concentration gradient triggers the diffusive transport of H_2 from the boundary between the porous anode and the flow domain to the catalytic reaction sites in the internal porous anode. The H_2 concentration profile in the diffusion layer (C_{H2}) drops with the anode depth until it drops to zero. The current density corresponding to this limiting case is termed 'limiting current density' (j_L), which is the highest current density the HOR can provide.[55] The diffusion layer thickness (δ_0) is established between C_{H2} = 0 and C_{H2}= C_{H2}^*.

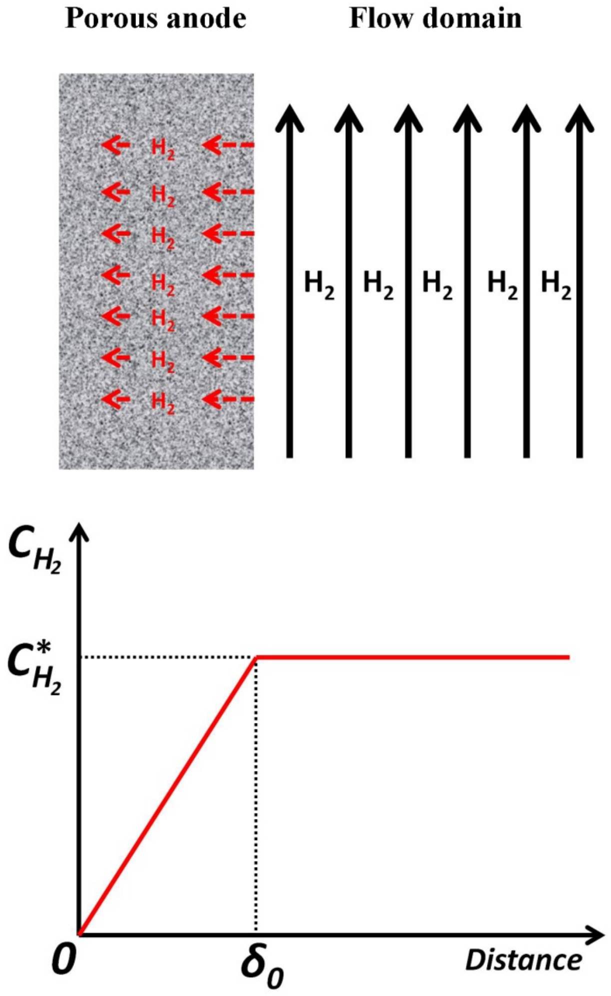

Figure 1.3. (*Upper panel*) Schematic diagram of the two mass-transport modes occurring at the porous anode and flow domain in a hydrogen fuel cell. The black arrows represent the convective flow and the red arrows represent the diffusive transport. (*Lower panel*) H_2 concentration profile (red line). Adapted from Reference 51.

The concentration gradient due to the reactant depletion in the diffusion layer can result in the voltage loss in a fuel cell.[47-49] Assuming a simplified electrochemical reaction with a single reactant and the activity of a product taken as 1, the potential loss due to concentration difference in the diffusion layer (η_{conc}) based on the Nernst equation can be written as:

$$\eta_{conc} = \left(E^0 - \frac{RT}{nF} ln \frac{1}{C_R^*}\right) - \left(E^0 - \frac{RT}{nF} ln \frac{1}{C_R}\right) = \frac{RT}{nF} \; ln \frac{C_R^*}{C_R} \tag{1.30}$$

where $C_R{}^*$ is the bulk reactant concentration and C_R is the reactant concentration in the diffusion layer. Moreover, the $C_R{}^*$ and C_R has the quantitative relationship to the limiting current density (j_L) and current density (*j*),[51] expressed as:

$$\frac{C_R}{C_R^*} = 1 - \frac{j}{j_L} \tag{1.31}$$

Substituting Equation 1.31 into Equation 1.30 yields:

$$\eta_{conc} = \frac{RT}{nF} \; ln \frac{j_L}{j_L - j} \tag{1.32}$$

This equation indicates the concentration loss (η_{conc}) will dramatically increase at high current density (*i.e.* $j \rightarrow j_L$) so that the potential can abruptly drop to zero. Raising j_L can expand the window of the increase in j.[61-67] As the limiting current density is directly proportional to the bulk reactant concentration,[51] maintaining a high value of $C_R{}^*$ is important for the improvement of fuel cell performance.

Up to this point, the reversible voltage and various voltage losses in a fuel cell have been analyzed. Thus the operating voltage of the fuel cell can be expressed as:

$$V = E - \eta_{ohm} - \eta_{act} - \eta_{conc} \tag{1.33}$$

where η_{ohm} is the ohmic loss due to electronic and ionic conductions, η_{act} is the activation loss from reaction kinetics, and η_{conc} is the concentration loss due to mass transport.

1.5 Fuel cell types

Fuel cells can be classified according to their electrolytes: alkaline fuel cell (AFC), molten carbonate fuel cell (MCFC), phosphoric acid fuel cell (PAFC), proton exchange membrane or polymer electrolyte membrane fuel cell (PEMFC), and solid oxide fuel cell (SOFC).[68] Moreover, fuel cells can be also classified according to their catalysts: conventional fuel cell (using non-biological, synthetic catalysts), microbial fuel cell (MFC), and enzyme-based fuel cell.[48] Although all fuel cell types have difference performance characteristics with their respective advantages and disadvantages, they share the same electrochemical principles, thus the designing or improvement of one type of fuel cells can be inspired by other types. In the following paragraphs, the technology-specific aspects of major fuel cell types are briefly introduced. (Note that conventional fuel cells are almost all covered by those fuel cells classified according to the electrolytes, thus conventional fuel cells will not be discussed separately, while enzyme-based fuel cell will be described in details in Section 2.3.)

The alkaline fuel cell (AFC) is the first practical fuel cell technology developed by Francis T. Bacon, and the AFCs were employed as an electricity generator and water producer in the Apollo-series spacecrafts.[69] The AFCs use aqueous alkaline solution (*e.g.* potassium hydroxide) as an electrolyte, in which hydroxide ions (OH^-) is transmitted from the cathode to the anode.[70] At the anode, OH^- reacts with H_2 to produce water and electrons, and at the cathode, O_2 combines with water and electrons to produce hydroxide ions. The OH^- ions act as the charge carriers in the AFCs. The anode and cathode reactions of the AFCs using pure H_2 and pure O_2 are:

$$\text{Anode:} \qquad H_2 + 2OH^- \longrightarrow 2H_2O + 2e^- \qquad (1.34)$$

$$\text{Cathode:} \qquad \frac{1}{2}O_2 + H_2O + 2e^- \longrightarrow 2OH^- \qquad (1.35)$$

It can be found that the water production at the anode is twice as much as the water consumption at the cathode, thus excess water must be removed from the anode; otherwise, the aqueous alkaline solution would become diluted and thus the fuel cell performance would be adversely affected.[71] The advantages of the AFCs include: *(1)* the current densities produced from the HOR and ORR reactions in the alkaline electrolyte are much higher than in the acidic electrolyte, thus non-platinum metals such as nickel can be employed as catalysts in the AFCs so that the fuel cell cost could be lowered; in addition, the aqueous alkaline electrolytes used in the AFCs are also inexpensive;[72-75] *(2)* the operating voltages of the AFCs is relatively high: 0.8 – 0.95 V, resulting in high fuel cell efficiency.[76] On the other hand, the disadvantages of the AFCs are also obvious. Except that water must be removed from the anode as mentioned above, the fuel and oxidant used in the AFCs (*i.e.* H_2 and O_2) must be purified to get rid of CO_2.[77] The AFCs cannot tolerate even a small amount of CO_2 present in air because the alkaline electrolyte can react with CO_2 to form carbonate ions, leading to both the decreased concentration of hydroxide ions in the electrolyte and the precipitation of carbonate ions due to their low solubility.[78] The carbonate crystals can block the electrode pores, thus adversely influencing the performance and lifetime of fuel cells.[79] Therefore, the AFCs cannot directly use air as their oxidants but only pure H_2 and O_2, thus limiting their terrestrial applications.

The molten carbonate fuel cell (MCFC) is a kind of medium/high-temperature fuel cells which have been developed since the 1950s.[80] The typical operating temperature of the MCFC is 650 °C.[81-83] Compared to low-temperature fuel cells, the advantages of the MCFCs are: *(1)* owing to relatively high operating temperature, not only hydrogen but also reformed or impure carbon fuels can be directly used as fuels; moreover, carbon monoxide becomes a fuel instead of a poison at such a high temperature;[84-86] *(2)* because the HOR and ORR reactions proceed very rapidly at the relatively high temperature, non-precious metal catalyst can be used in the MCFCs;[87] *(3)* the heat released from the fuel cell system can be used for cogeneration applications (*i.e.* combined heat and power), thus largely increasing the efficiency.[88] In the MCFCs, the electrolyte is a molten mixture of alkali carbonates (*e.g.* Li_2CO_3-K_2CO_3 or Li_2CO_3-Na_2CO_3) immobilized in a $LiAlO_2$ porous matrix.[89,90] At the anode, carbonate ions react with H_2 to produce CO_2 and water and liberate electrons; at the cathode, O_2 combines with electrons and CO_2 to form carbonate ion, which acts as a charge carrier in the MCFC. The anode catalysts are usually the Ni/Cr or Ni/Al alloys and the cathode catalysts usually consist of Ni-based nickel oxide.[91] The anode and cathode reactions of the MCFCs using H_2 as fuels are:

$$\text{Anode:} \qquad H_2 + {CO_3}^{2-} \longrightarrow H_2O + CO_2 + 2e^- \qquad (1.36)$$

Cathode: $$\frac{1}{2}O_2 + CO_2 + 2e^- \longrightarrow {CO_3}^{2-} \tag{1.37}$$

It can be found that CO_2 is consumed at the cathode and is produced in the anode. To maintain the recycling of CO_2 in the system, the waste stream containing CO_2 and H_2O is extracted from the anode and is then mixed with fresh reactants to the cathode.[92] Moreover, the above-mentioned electrode reactions do not involve carbon monoxide. In fact, CO makes its contribution to the electrode reactions by H_2 which is produced by the oxidation of CO in the water-gas shift (WGS) reaction at the high temperature.[93] To commercialize the MCFCs, lifetime/stability issues due to corrosive, molten electrolytes need solving.[94-96]

The phosphoric acid fuel cell (PAFC) is a mature fuel cell technology and has been already employed in commercialized fuel cell power plants.[97,98] The anode and cathode reactions of the PAFCs using H_2 as fuels are shown in Equations 1.1-1.2. Liquid-state pure or highly concentrated phosphoric acid (H_3PO_4) is used as an electrolyte.[99,100] Because the H_3PO_4 is in a solid state at room temperature (below 42 °C), the operating temperature of the PAFCs is usually elevated to 180 – 200 °C.[101,102] At the relatively low temperature (compared with the MCFCs), platinum is needed as an electrode catalyst which is usually immobilized onto high-surface-area activated carbon supports.[103-106] The PAFCs can use air as their cathode reactants because the Pt catalysts would not be poisoned by atmospheric CO_2, but Pt would become susceptible to CO and sulphides poisoning from reformed or impure fuels and reactants (as the susceptibility depends on temperature, the Pt catalysts in the PAFCs show a less degree of CO and sulphide poisoning than the Pt catalysts in fuel cells with operating temperature below 100 °C).[107-109] Moreover, the evaporation of H_3PO_4 tends to be fast at the operating temperature of the PAFCs, thus the electrolyte needs replenishing during operation.[110]

The proton exchange membrane or polymer electrolyte membrane fuel cell (PEMFC) employs solid-state polymer as an electrolyte. The most widely-used and commercially-available PEMs are perfluorinated membranes, including the DuPont's Nafion membranes, the Dow Chemical's Dow membranes, and the Asashi Chemical's Aciplex-S membranes.[111-113] Compared to liquid-state electrolytes, the solid-state PEMs do not require complex fuel cell operations but can make the electrolyte thickness as thin as possible and thus largely increase the power density of fuel cells, which are suitable for portable applications.[114,115] In the PEMFCs using H_2 as fuels and air as oxidants, H_2 and air reach the catalyst layers through the gas flow channels of bipolar plates and then the diffusion layers of membrane electrode assemblies (MEAs).[116] The anode and cathode reactions are shown in Equations 1.1-1.2. As the proton conduction in the electrolyte demands water, the humidification of the PEMs has an important effect on the ionic conductivity, thus the reactant gases need pre-humidifying and the operating temperature of the PEMFCs using classical membranes are kept below 100 °C.[117-119] The low-temperature operation has brought about at least three disadvantages: *(1)* the PEMFCs become very sensitive to even trace CO and sulphides;[120-123] *(2)* liquid water as a product can 'flood' the cathode and thus prevent fresh air from being able to react; *(3)* expensive platinum catalysts have to be used. To minimize these problems, *(1)* Pt/Ru-based alloys or composites have been developed to enhance the degree of CO and sulphide tolerance of the catalysts;[124-128] *(2)* active water management need applying to effectively remove liquid water;[129,130] or more fundamentally, develop novel PEMs which can withstand high temperature above 100 °C, thus leading to the improved CO and sulphide tolerance, simplified water management, and enhanced reaction kinetics;[131-135] *(3)* develop efficient non-precious metal catalysts.[136-141] The core part of the PEMFCs is the MEA, comprising of PEM, catalyst layer, sub-layer, and gas diffusion layer.[142] The gas diffusion layer is usually made of carbon paper treated by hydrophobic polytetrafluoroethylene (PTFE).[143-146] The sub-layer refers to a thin layer of activated carbon to level the gas diffusion layer.[147,148] The platinum-based catalyst on the porous activated carbon support is coated on the sub-layer, forming the catalyst layer.[149-152] The PEM-catalyst layer-sub-layer-gas diffusion layer combination undergoes the hot pressing to form the sandwich structure – the MEA.[153-155] Multiple MEAs with sealing rings and bipolar plates constitute a fuel cell stack.[156,157] Though the PEMFCs use expensive polymer membranes and platinum catalysts (though novel inexpensive and efficient catalysts and membranes are being explored), which are sensitive to CO and sulphide and need water management, they have exhibited very high power densities and fuel cell efficiencies at relatively low temperature, and also showed excellent on-off cycling characteristics, all of which make the PEMFC a promising technology as the vehicle power source.[158-160] Moreover, as the PEMFCs are low-temperature fuel cells, those using bacteria or enzymes as catalysts (*i.e.* microbial and enzyme-based fuel cells) often draw on the PEMFC principles and technologies.[161,162]

The solid oxide fuel cell (SOFC) is a type of all solid-state fuel cells and its most common electrolyte is yttria-stabilized zirconia (YSZ).[163] Zirconia (ZrO_2) itself has no ionic conductivity, but Zr^{4+} would be replaced by Y^{3+} in the ZrO_2 lattice after doping yttria

(Y_2O_3), forming oxygen vacancies and thus being able to conduct O^{2-} ions.[164] Every two doped Y^{3+} could constitute one oxygen vacancy and the maximum ionic conductivity of the YSZ can be achieved when the doped Y_2O_3 is about 8% (mol) at 1000 °C.[165] Therefore, the O^{2-} ion acts as the charge carrier in the SOFC and the anode and cathode reactions are:

Anode: $$H_2 + O^{2-} \longrightarrow H_2O + 2e^- \quad (1.38)$$

Cathode: $$\frac{1}{2}O_2 + 2e^- \longrightarrow O^{2-} \quad (1.39)$$

At the typical operating temperature of the SOFCs (800 – 1000 °C), O_2 is reduced to O^{2-}, which is then transported from the cathode to the anode via the oxygen vacancies of the YSZ; at the anode, H_2 is oxidized and combines with O^{2-} to produce water and release electrons. In the SOFCs, the anode materials usually employ porous Ni-YSZ, in which Ni acts as a catalyst, and the cathode materials typically use porous $La_{1-x}Sr_xMnO_3$ (LSM), providing catalytic activity and mechanical stability; the cathode-electrolyte-anode combination undergoes co-pressing and co-sintering to constitute an entire electrode-electrolyte assembly.[166-168] As mentioned above, the high operating temperature can result in obvious advantages, such as cogeneration applications, viability to use non-precious metal catalyst, and relatively high reaction kinetics, but the high temperature could also lead to the material, sealing and fabrication issues.[169] Therefore, it is important to develop novel materials which can decrease the operating temperature to 400 – 600 °C for the SOFCs.[170-172]

The microbial fuel cell (MFC) uses bacteria as catalysts to convert the chemical energy stored in organic compounds such as different kinds of carbohydrates and complex substrates from wastewater into electrical energy.[173-175] The working principles of the MFCs are: at the anode, bacteria decompose organic compounds under anaerobic conditions to release electrons and protons; electron transfer from the microorganisms to the anode is either direct (in mediator-less MFC) or facilitated by mediators (in mediator MFC); protons are transmitted from the anode to the cathode through the PEMs, while electrons flow from the anode to the cathode via an external circuit; at the cathode, electrons combine with protons and O_2 (usually using air) to produce water by Pt-based catalysts.[176-178] It can be found that the MFCs and PEMFCs share the similar processes of electricity generation except the anode reactions. The operating temperature of the MFCs is generally much lower than that of the PEMFCs, ranging from 20 °C to 40 °C.[179-181] In the mediator MFCs, electron transfer from microorganisms to anodes depends on redox mediators, such as thionine, methylene blue, and neutral red, in which act as electron relays in the electron transfer chain.[182-184] The disadvantages of the mediated electron transfer are cost and toxicity of mediators as well as voltage loss of the MFCs.[185] Owing to the characterization of some electrochemically active bacteria, the mediator-less MFCs in which electrons can be directly shuttled from bacteria to anodes are now feasible.[186-189] Moreover, applying the MFC technology to the treatment of wastewater has drawn more attention recently.[190,191]

In summary, all types of fuel cells have their respective advantages and disadvantages in terms of cost, power density, and durability. The AFCs and PAFCs are the mature fuel cell technologies, but they have currently met key technological bottlenecks (*e.g.* electrolytes) which prevent them from becoming competitive, alternative power sources. The most rapid progress that has been made in recent years is the PEMFC technology, which is suitable for portable and transport applications. The high-operating-temperature fuel cell technologies – the MCFC and SOFC are suited for fuel cell power plants due to their fuel flexibility, non-precious metal catalysts and high-quality waste heat for cogeneration applications. The MFC technology is suitable for wastewater treatment works and those practical applications of low-power requirement, such as wireless sensor networks for ecological monitoring. Up to now, the basic principles and technologies of fuel cells have been discussed. On the basis of such fuel cell fundamentals, fuel cells using enzymes which can efficiently catalyze the HOR and ORR reactions will be described next chapter.

Chapter 2

Enzymes as Fuel Cell Catalysts

Abstract

Enzymes can be employed as electrocatalysts for fuel cell reactions. In this chapter, the structures and functions of hydrogenases (for the HOR) and multi-copper oxidases exemplified by laccase and bilirubin oxidase (for the ORR) are introduced. Furthermore, the advantages and disadvantages as well as the major types of enzyme-based fuel cells are mentioned. Last, the outline of this thesis is presented.

2.1 Enzymes for the HOR – hydrogenases

As mentioned in Section 1.5, fuel cells with the operating temperature below 300 °C need Pt-based catalysts. It is well known that the disadvantages of using Pt as fuel cell catalysts include cost, rare reserves, and susceptibility to CO and sulphide poisoning at relatively low temperature. Therefore, it is highly desirable to discover and develop alternative, renewable, and efficient catalysts. People always draw inspiration from Nature. As we know, H_2 acts as an energy source for many bacteria, and enzymes known as hydrogenases expressed by these bacteria take part in the hydrogen cycling – including both oxidation and evolution of H_2.[192] The active sites of these enzymes contain the abundant first-row transition elements – Ni and Fe; this characteristic combined with their efficient electrocatalytic activities of H_2 oxidation and production has been attracting scientists to synthesizing complex molecules that can mimic the enzymatic H_2 cycling.[193-195] Moreover, hydrogenases absorbed at pyrolytic graphite edge (PGE) electrodes show active catalytic oxidation of H_2 at rates comparable to the electrodeposited Pt and exhibit much less susceptibility to CO poisoning than Pt at room temperature.[196,197] Therefore, it is very interesting to apply hydrogenases to the HOR in a fuel cell. To acquire a fundamental overview of hydrogenases, the following sub-sections will introduce hydrogen cycling in microbial organisms – concerning with the origins of hydrogenases (Section 2.1.1), types/structures/states of hydrogenases (Section 2.1.2), and inhibition of hydrogenase by small molecules such as O_2, CO and sulphides, which are commonly found in soil and reforming gases (Section 2.1.3).

2.1.1 H_2 cycling by bacteria

Bacteria in soil cannot directly use the atmospheric H_2 because the level of H_2 in the Earth's lower atmosphere is too low (~0.5 ppm).[198] H_2 that can be taken up by bacteria evolves from some biological processes in soil – for example, fermentative bacteria can produce H_2 by the fermentation of carbohydrates, N_2-fixing microorganisms in the root nodules of plants can generate H_2 in the process of ammonia formation, and photosynthetic bacteria such as cyanobacteria can produce H_2 through photosynthesis.[199-202]

Bacteria make use of H_2 by coupling H_2 oxidation to the reduction reactions of some molecules or ions, such as carbon dioxide, sulphate, and nitrate.[203] Figure 2.1 shows a schematic representation of the microbial H_2 uptake in wet soil. The level of H_2 decreases with decreasing soil depth whereas the O_2 level is the exact opposite, thus forming the H_2/O_2 concentration gradients in soil. This characteristic has made hydrogenases expressed by the bacteria living at different soil depths adapt to different levels of H_2 and O_2 and thus exhibit different affinity for H_2 and tolerance towards O_2 in order to survive.[203] As shown in Figure 2.1, methanogens, sulphate-reducing bacteria, iron (III)-reducing bacteria, denitrifying bacteria, and aerobes such as Knallgas bacteria are distributed in order from the depths to the surface of soil. The bacteria nearer to the soil surface exhibit the lower H_2 threshold concentration (below which H_2 cannot be taken up by bacteria) and the higher affinity for H_2 due to the decreasing level of H_2 – for example, the H_2 threshold concentration for methanogens is 70 ppm, the threshold for sulphate-reducing bacteria is 10 ppm, and the threshold for Knallgas bacteria at the top decreases to 1 ppm.[204-206] Membrane-bound hydrogenases (MBHs) produced by *Ralstonia eutropha H16* (a kind of Knallgas bacteria) show a good catalytic activity of H_2 oxidation in the O_2-rich/H_2-poor mixture, which arouses interest in terms of fuel cell applications.[207] In addition to O_2, the bacteria also need to adapt to the presence of CO, NO, and H_2S produced by microbial metabolism.[203,208] In short, the H_2 cycling by bacteria has outlined the variable hydrogenases which exhibit different catalytic bias and activities for H_2 production and oxidation in different conditions.

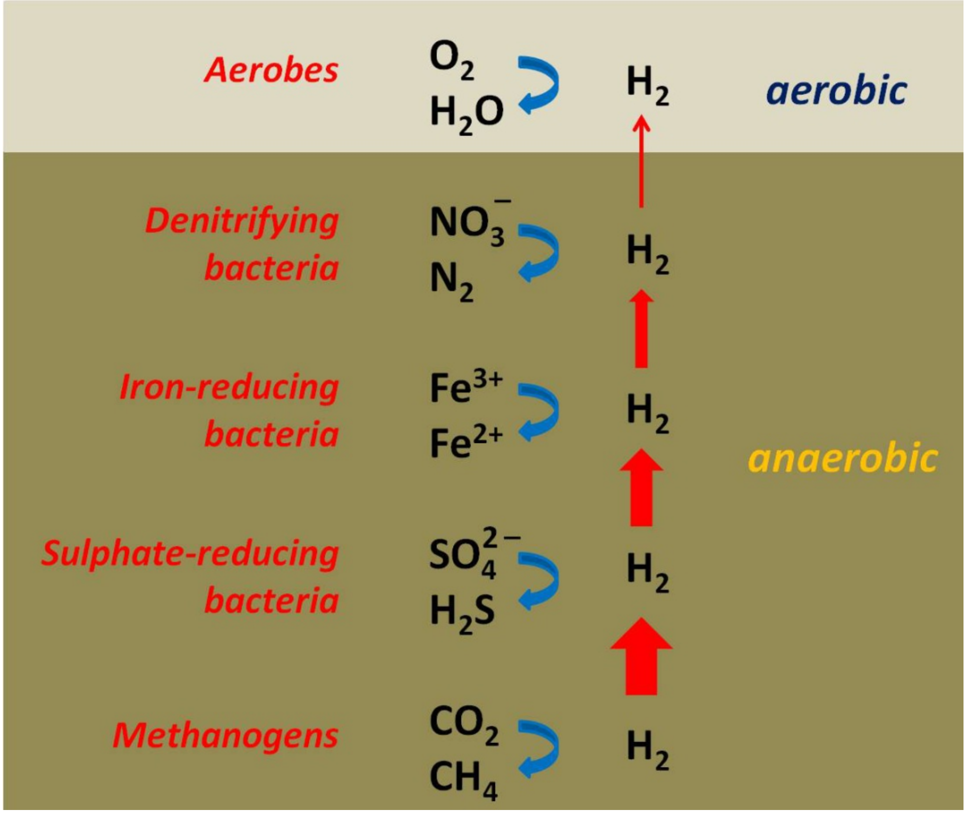

Figure 2.1. Schematic representation of the H_2 uptake in a wetland soil. The levels of H_2 in soil are indicated by the thickness of the red vertical arrows. The reduction processes coupled to H_2 oxidation for the bacteria distributed at different depth of soil are also provided. Adapted from Reference 203.

2.1.2 Types, structures and redox states of hydrogenases

Convergent evolution has created various hydrogenases which share no similarity of their genetic sequence in the microbial world.[209] The minimum common unit in hydrogenases is [Fe(CO)(CN)(RS)].[210] Hydrogenases can be classified into the three types according to the metal composition of their active sites, that is, [NiFe]-, [FeFe]-, and [Fe]-hydrogenases.[211-213] [NiFe]- and [FeFe]-hydrogenases show the opposite catalytic bias towards the inter-conversion of H_2 and protons: [NiFe]-hydrogenases are more frequently involved in the oxidation of H_2 whereas [FeFe]-hydrogenases are usually associated with the production of H_2.[214,215] When external environments to which hydrogenases are exposed are taken to unusual extremes, such typical catalytic bias of hydrogenases may change. For example, an O_2-tolerant [NiFe]-hydrogenase from *E. coli* turns out to be an efficient H_2 producer below pH 4.[216] One subspecies of [NiFe]-hydrogenases is known as [NiFeSe]-hydrogenases in which a selenocysteine coordinated to the Ni replaces one of the terminal cysteine residues of the typical [NiFe]-hydrogenases.[212,213] The [NiFeSe]-hydrogenase from *Desulfomicrobium baculatim* shows high catalytic activities for both the production and oxidation of H_2 in the presence of 100% H_2 and also exhibit an O_2-tolerant H_2-production activity in the presence of 1% O_2.[217] The third type of hydrogenases – [Fe]-hydrogenases which are the most recently discovered and are only found in methanogens catalyze the reversible reduction of N^5,N^{10}-methenyltetrahydromethanopterin with H_2 to N^5,N^{10}-methylenetetrahydromethanopterin and a proton as an important step towards the conversion from carbon dioxide to methane rather than catalyze the direct inter-conversion of H_2 and protons like [NiFe]- and [FeFe]-hydrogenases.[218] This chapter focuses on [NiFe]-hydrogenases that are more closely linked with the HOR, and their structures and various redox states are briefly introduced as below.

The active site of a typical [NiFe]-hydrogenase contains one Ni, one Fe, four cysteines, two CN^-, and one CO.[219-221] As shown in Figure 2.2, two cysteine ligands coordinate the Ni atom, and the other two cysteine ligands act as sulphur bridges between the Fe atom and the Ni atom; in addition to the two bridging cysteines, the Fe atom is also coordinated by one CO and two CN^- ligands. In organometallic chemistry, the 18-electron rule is often used to predict the stability of d-block organometallic compounds; that is, transition metal complexes are expected to be stable if the total number of metal valence electrons including those from ligands is 18.[222] The 18-electron rule should be applicable to the active site of [NiFe]-hydrogenases, which belongs to a d-block organometallic compound.[212] If the oxidation state of the Fe atom is +2 and the Ni atom is assigned as either Ni^{I} or Ni^{II}, or Ni^{III}, none of these metals have 18 valence electrons, thus both the Fe and Ni atoms become susceptible to attack by an additional ligand (X), such as hydroxide, hydroperoxide, and sulphur.[223-225]

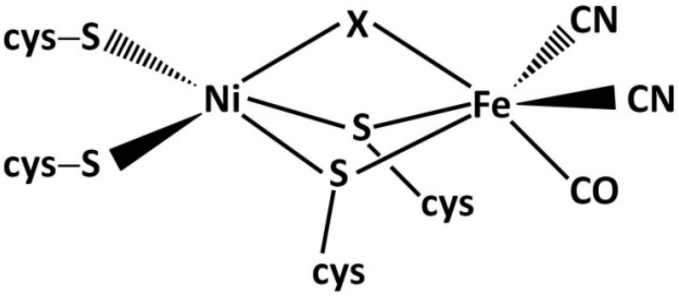

Figure 2.2. A representation of the active site of a [NiFe]-hydrogenase from *Desulfovibrio desulfuricans*. Adapted from Reference 219.

[NiFe]-hydrogenases contain three iron-sulphur (Fe-S) clusters known as electron relay centres to connect the active sites buried within the protein matrix to the surface.[212] The three Fe-S clusters can be classified according to their distances to the active site: the proximal cluster (closest to the active site), the medial cluster, and the distal cluster (farthest from the active site).[213] The distances between the active site and Fe-S clusters as well as between the Fe-S clusters themselves are typically within 14 Å: for example, the active site and the proximal, medial, and distal Fe-S clusters of the [NiFe]-hydrogenase from *Desulfovibrio fructosivorans* are positioned 10.7 Å, 9.6 Å, and 8.4 Å apart, respectively.[220] Such distances allow for efficient electron transfer from the active site to the protein surface by electron tunnelling and meanwhile do not limit the rate of catalysis.[226] The structures of Fe-S clusters have an important effect on the property of [NiFe]-hydrogenases. For example, both O_2-tolerant and O_2-sensitive [NiFe]-hydrogenases share the same structures of the medial [3Fe-4S] and the distal [4Fe-4S] clusters, but the structural difference of their proximal clusters, [4Fe-3S] for the O_2-tolerant hydrogenases and [4Fe-4S] for the O_2-sensitive hydrogenases, has decided whether or not they are able to catalyze the H_2 oxidation in the presence of O_2.[227-229] This will be further discussed in Section 2.1.3.

H_2 and proton are the substrate and product for H_2 oxidation, respectively, thus it is very important to understand how H_2 and protons diffuse towards and from the deeply buried active sites of [NiFe]-hydrogenases. The hydrophobic gas channel between the protein surface and the active site has been revealed by the crystal structure of the xenon-bound [NiFe]-hydrogenase from *Desulfovibrio fructosovorans*: that is, several small channels at the protein surface combine to form one channel capable of reaching the active site.[230] The molecular dynamics simulation has shown the gas channel ends near the Ni atom of the active site and that H_2 can reach the distance of <4 Å from the active site.[231] In addition to H_2, other gas molecules such as O_2 and CO can also access to the active site via such gas channels.[232] The size and chemical environment of gas channels have a significant influence over the diffusion rates of gases and the enzymes' susceptibility to O_2 and CO inhibition. For example, narrowing the gas channel of the mutants of a [NiFe]-

hydrogenase led to the decrease in the diffusion rates of CO and H_2 towards and from the active site by up to two orders of magnitude;[233] increasing the size of the gas channel made the mutants become O_2 sensitive;[234] and replacing small hydrophobic residues in the gas channel with methionines resulted in the improvement of O_2 tolerance of the mutated [NiFe]-hydrogenases.[235] For the proton transport between the protein surface and the active site, the crystallographic data have yet to be available, but several possible proton pathways involving histidine and glutamate residues have been proposed by theoretical studies.[236,237] In one proposition, the proton pathway is suggested to be a hydrogen bonding network between the active site and the Mg^{II} cation coordinated by histidine and glutamate residues as well as water molecules in the C-terminus region of the large subunit of a [NiFe]-hydrogenase.[232]

In the active site of a [NiFe]-hydrogenase, the iron atom usually stays in the Fe^{II} state, while the oxidation state of the Ni atom is variable, ranging from Ni^{I} to Ni^{II} and Ni^{III}, thus leading to the different redox states of the [NiFe]-hydrogenase.[238-240] The paramagnetic Ni^{I} and Ni^{III} can be characterized by electron paramagnetic resonance (EPR), while the diamagnetic, EPR-silent Ni^{II} state can be characterized by Fourier-transform infrared (FTIR) based on the shifts of CO and CN vibrations.[241-244] Figure 2.3 summarizes the inter-conversions of the typical redox states of the [NiFe]-hydrogenases. The enzymes have three active states: Ni-SI, Ni-C, and Ni-R. The Ni-SI state corresponds to the EPR-silent Ni^{II} species which can be oxidized to the Ni^{III}-hydride species known as the Ni-C state.[245] The Ni-C state is sensitive to light and could lose the hydride by illumination, forming the Ni-L state (Ni^{I} species) which is stable only at low temperature (200 K).[246]

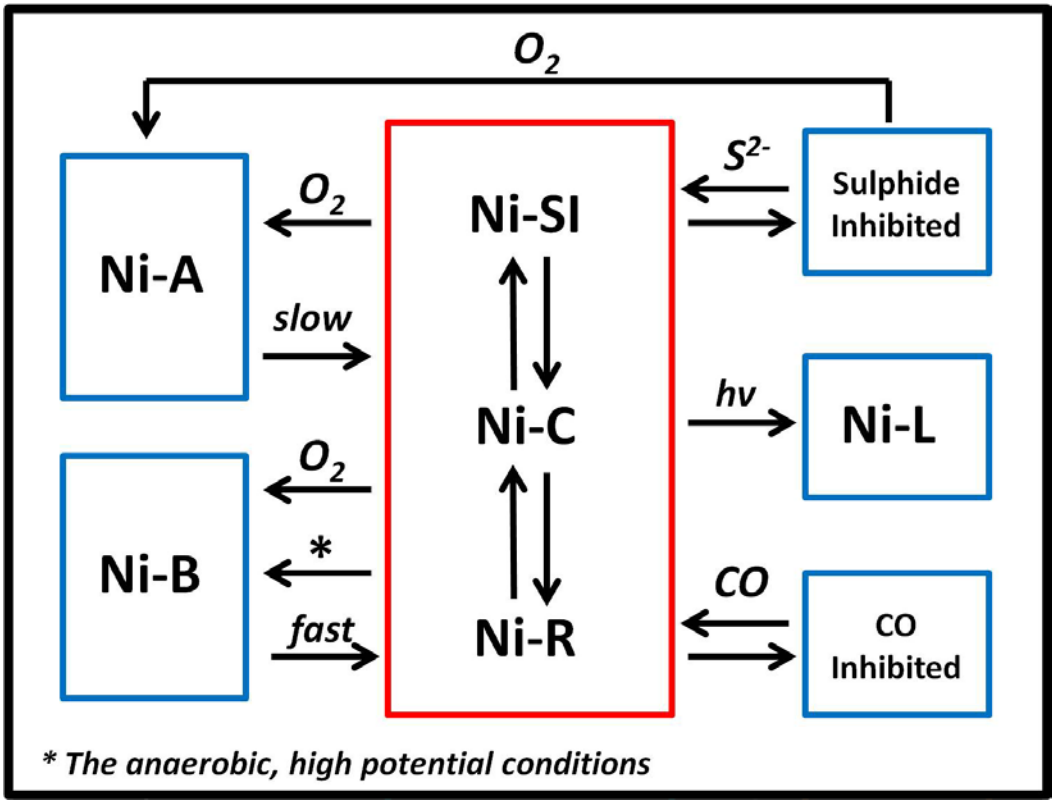

Figure 2.3. A schematic representation of the different redox states of a [NiFe]-hydrogenase and its reactions with common inhibitors. Adapted from References 212 and 246.

Reduction of the Ni-C state gives the Ni-R state corresponding to the Ni^{II}-hydride species.[241] The reaction of [NiFe]-hydrogenases with O_2 leads to two inactive states: Ni-A (Unready) and Ni-B (Ready).[247] The Ni-B state can be also formed at high-potential, anaerobic conditions.[248] It has been suggested that the Ni-A state contains a bridging peroxide ligand while the Ni-B state contains a bridging hydroxyl ligand in the active site.[249] The oxidation states of the Ni atoms in both the Ni-A and Ni-B states are +3, while the obvious difference between the Ni-A and Ni-B states lies in their recovery rate to the active state: the reactivation rate of the Ni-A state is orders of magnitude slower than the reactivation of the Ni-B state.[247] The reaction of the [NiFe]-hydrogenases with O_2 will be further discussed in Section 2.1.3. Moreover, the electrochemical experiments have proved that the reaction of [NiFe]-hydrogenases with CO is completely reversible.[250] The reaction of [NiFe]-hydrogenases with sulphide is also reversible, but the Ni-A state containing oxygenated sulphur species would be generated if the sulphide-bound enzymes are exposed to O_2.[221,251]

2.1.3 Inhibition of hydrogenases by small molecules

The common inhibitors of hydrogenases are small molecules, such as CO, sulphide, and O_2, which exist as microbial metabolites in soil. In different living environments, bacteria have evolved different degrees of tolerance towards to the inhibitors. Therefore, hydrogenases produced by different bacteria exhibit various degrees of inhibition by these small molecules (*e.g.* reversible or irreversible), which can be studied by electrochemical methods and other characterization techniques. Understanding how hydrogenases undergo the inhibition by such molecules is important in terms of an effort to use hydrogenases as electrocatalysts of the HOR because these molecules can be also found in reforming gases and other impure fuels supplied to fuel cells.

As mentioned in Section 2.1.2, CO is a reversible inhibitor of hydrogenases for H_2 oxidation by binding the Ni atom of the enzymes to form a CO-inhibited state (see Figure 2.3). O_2-tolerant [NiFe]-hydrogenases exhibit only weak CO inhibition.[252-254] A cyanide anion is isoelectronic with CO and also acts as a reversible inhibitor of hydrogenases. The electrochemical, EPR, and FTIR measurements have recently revealed that the Ni-B state will be generated when [NiFe]-hydrogenases are reacted with CN^- so that the enzymes can be easily reactivated.[255] Moreover, sulphide such as H_2S acts as a reversible inhibitor of O_2-sensitive [NiFe]-hydrogenases.[251] The crystallographic data have proved the presence of an exogenous sulphide bridging the Ni and Fe atoms in the active site of the [NiFe]-hydrogenase from *Desulfovibrio vulgaris*.[256] Liberation of H_2S has been observed during the reactivation of hydrogenases from *Desulfovibrio vulgaris* under the atmosphere of pure H_2, thereby suggesting the reversible inhibition by H_2S for the O_2-sensitive [NiFe]-hydrogenases.[257] It is suggested that the sulphide-inhibited state of the [NiFe]-hydrogenase contains an S^{2-} or HS^- bridging ligand.[251] As mentioned in Section 2.1.2, the sulphide-inhibited state will be converted into the Ni-A state when the sulphide-bound O_2-sensitive [NiFe]-hydrogenases are exposed to O_2. On the other hand, O_2-tolerant [NiFe]-hydrogenases do not react with sulphide.[210]

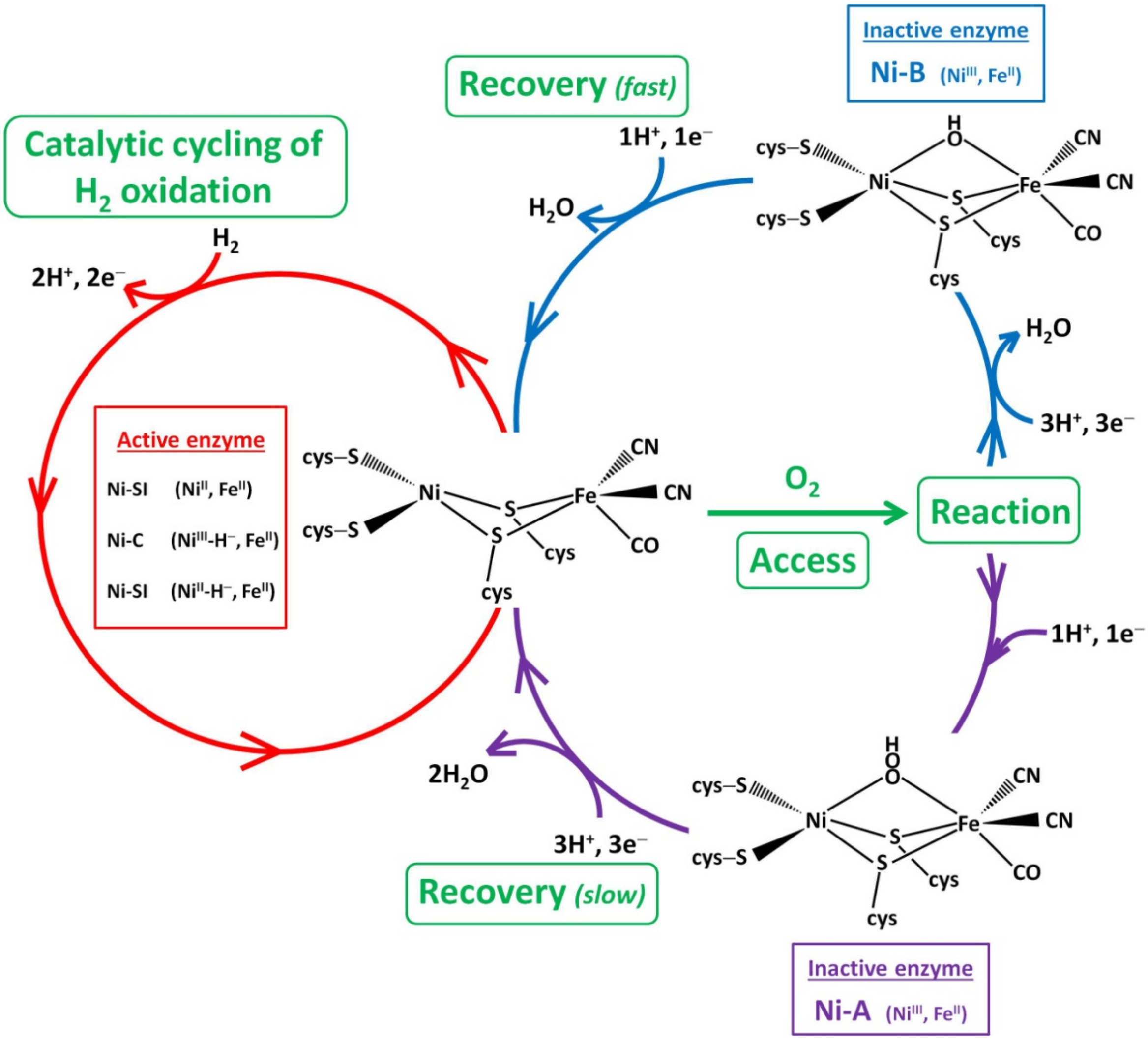

Figure 2.4. A schematic representation of the reactions of a [NiFe]-hydrogenase with O_2 and H_2. The catalytic cycling of H_2 oxidation for the active enzyme is indicated in a red circle. There are two pathways to the formation of aerobically inactive states: the Ni-A and Ni-B states. Which pathway is dominated is determined by the number of additional electrons immediately available from the Fe-S clusters to the active site when the enzyme is attacked by O_2. The cycling of the active state and the inactive Ni-A state is indicated in a purple circle and the cycling of the active state and the inactive Ni-B state is indicated in a blue circle. Adapted from Reference 259.

O_2 is a potent inhibitor of hydrogenases which are either inactivated or permanently damaged by O_2.[210] The active sites (known as H-clusters) of [FeFe]-hydrogenases undergo permanent damage in the presence of even trace O_2 because O_2 first binds the di-iron domain of the H-cluster and then the reactive products of O_2 reduction cause irreversible damage to the [4Fe-4S] cluster of the H-cluster.[258] On the other hand, [NiFe]-hydrogenases undergo largely reversible inhibition by O_2 and will form a combination of two inactive states – the Ni-A (Unready) and Ni-B (Ready) when they are attacked by O_2 (see Figure 2.3). The formation ratio of Ni-A to Ni-B during the reaction of [NiFe]-hydrogenases with O_2 has determined whether or not the hydrogenases can retain the catalytic H_2-oxidation activity in the presence of O_2, *i.e.* O_2-sensitive or O_2-tolerant hydrogenases.[259] The O_2-tolerant characteristic of a [NiFe]-hydrogenase is an indispensible condition for applying this alternative electrocatalyst to the HOR in a fuel cell.[213] Some O_2-tolerant [NiFe]-hydrogenases have been characterized so far, including MBHs from *Aquifex aerolicus*,[240] *Escherichia coli*,[254] *Ralstonia metallidurans*,[260] and *Ralstonia eutropha*.[261]

To understand how the O_2 tolerance of a [NiFe]-hydrogenase is formed, the process of catalytic cycle → inactivation cycle → catalytic cycle can be considered in the three distinct stages: access, reaction, and recovery.[210, 259, 262] Figure 2.4 shows a schematic representation of catalytic cycling of H_2 oxidation and aerobic inactivation cycles. *(1)* ‘Access’ refers to how quickly O_2 can reach the active site; as mentioned in Section 2.1.2, the size of gas channels has a big effect on the access of H_2 to the active site. *(2)* ‘Reaction’ involves the binding of O_2 at the active site, which leads to the formation of either the Ni-

A state containing a peroxide bridging ligand or the Ni-B state containing a hydroxide bridging ligand. If a [NiFe]-hydrogenase exhibits the O_2-tolerance, its Ni-B state must vastly outnumber the Ni-A state. As shown in Figure 2.4, the fast delivery of sufficient electrons to the active site can ensure the formation of the Ni-B state. In other words, if O_2 attacks the active Ni-SI state, three additional electrons are required to reduce O_2 to hydroxide as the Ni-SI state (Ni^{II}) is one electron more reduced than the Ni-B state (Ni^{III}), as depicted in the blue cycle (see Figure 2.4); if O_2 attacks the active Ni-C state, two additional electrons are required as the Ni-C state (Ni^{III}-hydride) is two electrons more reduced than Ni-B; if O_2 attacks the active Ni-R state, one additional electron is required as the Ni-R state (Ni^{II}-hydride) is three electrons more reduced than Ni-B. All these additional electrons must be supplied by electron sources close to the active site. Crystal structures of the O_2-tolerant [NiFe]-hydrogenases from *Ralstonia eutropha*, *Hydrogenovibrio marinus* and *Escherichia coli* have revealed that the unusual proximal [4Fe-3S] cluster has an important influence over the O_2 tolerance.[228,229,263] This proximal [4Fe-3S] cluster in the O_2-tolerant hydrogenases is coordinated by six cysteine residues rather than the proximal [4Fe-4S] cluster coordinated by four cysteine residues in O_2-sensitive hydrogenases. The EPR data have shown that the proximal [4Fe-3S] cluster can undergo two sequential redox transitions: $[4Fe\text{-}3S]^{3+} \leftrightarrow [4Fe\text{-}3S]^{4+} \leftrightarrow [4Fe\text{-}3S]^{5+}$, thus indicating that such proximal cluster can deliver up to two electrons to the active site when O_2 attacks the enzymes.[264] Moreover, the medial [3Fe-4S] cluster can provide the third electron for the active site.[265] *(3)* 'Recovery' is concerned with both kinetics the and thermodynamics of the reductive activation of the inactive states back to the active state.

As shown in Figure 2.4, the Ni-B state recovers rapidly while the Ni-A state recovers very slowly. Furthermore, a more reducing potential has a stronger external driving force to provide sufficient electrons rapidly for the inactive states. In short, the *intrinsic* O_2 tolerance of [NiFe]-hydrogenases depends on the 'limited' access of O_2 and the predominance of the formation of the Ni-B state upon the reaction with O_2 (Ni-B can allow for the fast recovery). In Chapter 5, a non-biological method is presented to be able to substantially increase the degree of the *apparent* O_2 tolerance of [NiFe]-hydrogenases.

2.2 Enzymes for the ORR – multi-copper oxidases

Compared to the HOR, the ORR is sluggish and causes the large activation overpotential loss at the cathode because the four-electron reduction of O_2 to H_2O is complex and involves many individual steps.[266,267] Moreover, most fuel cells use air rather than pure O_2 as their oxidant.[14] As discussed in Section 1.3, the kinetics operating on air that comprises of 21% O_2 is approximately only one fifth of the kinetics running on pure O_2. Therefore, it is very important to develop efficient catalysts that are able to decrease the activation barrier as well as the overpotential of the ORR. To date, many catalysts with high electrocatalytic activity for the ORR have been made, including those Pt-based and metal-free nanostructures.[268,269]

Learning from Nature, the 'blue' copper oxidases known as multi-copper oxidases that can be found in many plants and fungi have been proved to be able to efficiently catalyze the four-electron reduction of O_2 at relatively small overpotentials.[270-272] Among the multi-copper oxidases, laccase and bilirubin oxidase (BOD) are more frequently used as the ORR catalysts in enzyme-based fuel cells.[273-277] The crystal structures of laccase and BOD are similar.[278,279] Figure 2.5 shows the crystal structure of BOD from *Myrothecium verrucaria* as well as the schematic representation of the electron transfer from the electrode to the active site and the ORR occurring at the active site provided the BOD is attached to an electrode. The Type 1 Cu atom is located close to the protein surface and is suggested to act as an immediate electron acceptor from the extrinsic environment.[280] The crystallographic data have revealed the Type 1 Cu atom of the BOD is surrounded by a hydrophilic environment including two non-coordinating amino acids: asparagine and threonine, serving as 'anchors' in terms of the attachment of the enzyme to the electrode.[279] Such anchoring allows for the fast, direct electron transfer from the electrode to the BOD because the distance between the Type 1 Cu atom and the electrode is minimized. For laccases, the residues around the Type 1 Cu atom are hydrophobic, thus electrodes are often modified with aromatic functionalities to improve the binding of enzymes and the electron tunneling.[281] The active site of the BOD is the trinuclear Cu cluster known as the Type 2/Type 3 Cu site composed of an apical Type 2 Cu atom and a Type 3 Cu pair. The distance between the active site and the Type 1 Cu atom is within 14 Å, allowing for fast, intramolecular electron tunneling.[226,279] Through the Type 1 Cu site as an electron relay, four electrons tunnel from the electrode to the Type 2/Type 3 Cu site, where the ORR occurs. The reactants (*i.e.* O_2 and protons) and the product (*i.e.* H_2O) enter and leave the active site of the BOD via two channels: one channel terminates close to the Type 2 Cu atom and the other terminates at the Type 3 Cu pair.[279] In laccases, there are also two channels for the mass transport of reactants and products.[282]

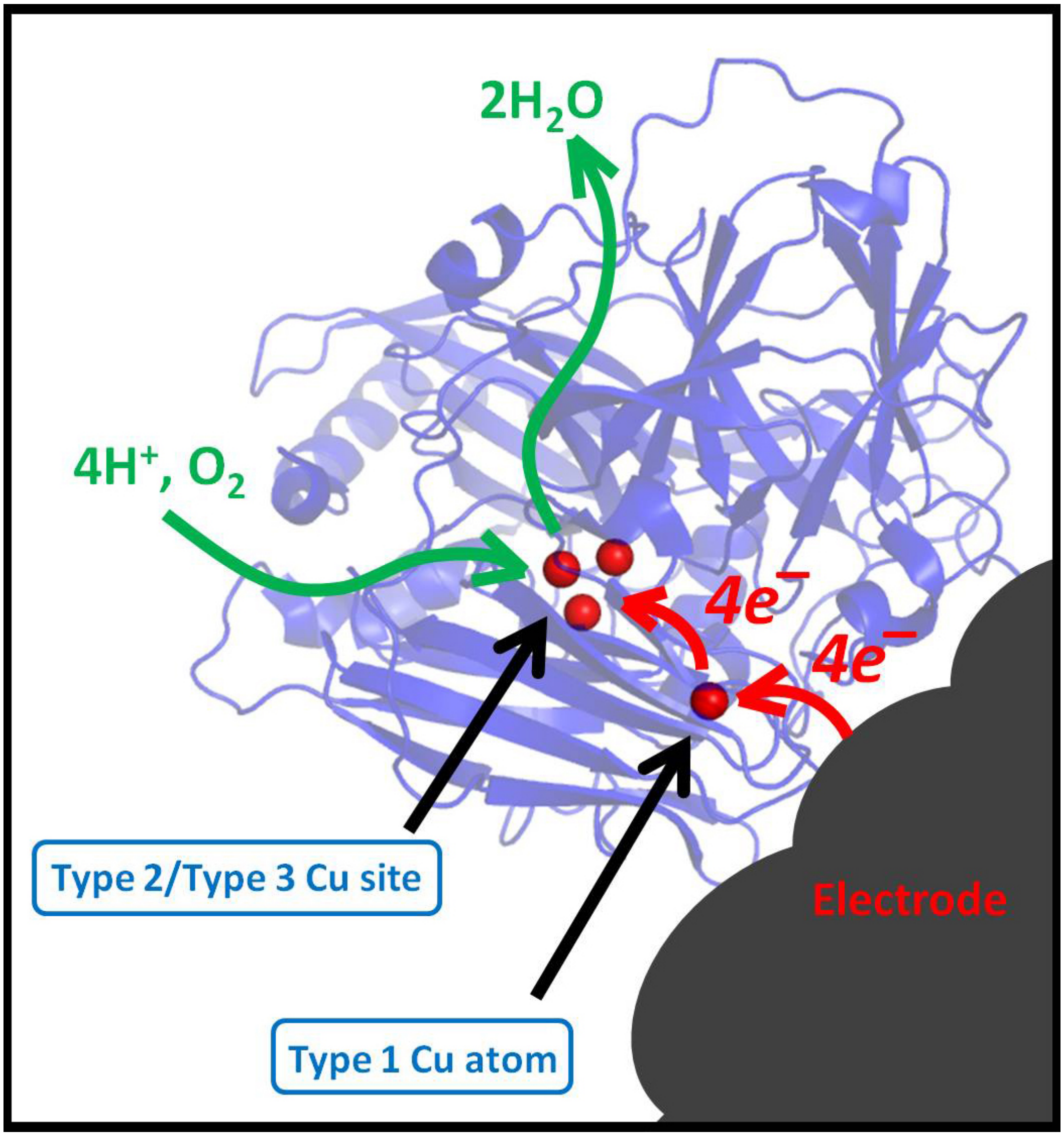

Figure 2.5. A schematic representation of the attachment of BOD to an electrode. The crystal structure of BOD from *Myrothecium verrucaria* (Protein data bank code: 2XLL) is created using PyMOL: the protein superstructure is indicated in blue and the copper atoms are indicated as red spheres. Electron tunnelling from the electrode to the trinuclear Type 2/Type 3 Cu cluster (active site) through the Type 1 Cu atom is depicted

in red arrows. The reduction of O_2 to H_2O occurs at the active site, and the reactant and product pathways are indicated in green arrows.

As the ORR electrocatalysts in enzyme-based fuel cells, BODs have the distinct advantages over laccases because the pH window of laccases is narrow (pH 3-5) and laccases are inhibited by halide ions, such as F^- and Cl^- ions.[283-286] Iketa and co-workers first proposed using BOD as an electrocatalyst for the ORR in a biofuel cell, but they used a mediator – 2,2-azinobis(3-ethylbenzothiazoline-6-sulfonate) (ABTS) in the electrocatalytic reduction of O_2.[287] Heller and Mano have developed a method of wiring BOD to the electrode surface by electron-conducting redox hydrogels exemplified by the Os redox polymer.[288-290] The redox hydrogels allow for the good electronic contact between the enzyme and the electrode.[291] However, as mentioned in Section 1.5, such a mediated electron transfer based on redox mediators including the ABTS and Os polymer has the obvious disadvantages: cost, toxicity, operational complexity, and voltage loss. In this thesis, the mediator-free HOR and ORR are realized by embedding hydrogenase and BOD into 3D porous carbon electrodes (Chapters 3-4). The rough internal surface of the 3D electrodes results in good electronic contact between the electrode and electron entry/exit sites (relay centres) of the enzymes, that is, [Fe-S] clusters for hydrogenase and Type 1 Cu atom for BOD.

2.3 Enzyme-based fuel cells

Enzyme-based fuel cells are operated based on the same underlying electrochemical principles as other types of fuel cells, while the intrinsic characters of enzyme-based fuel cells distinct from other types due to enzymes as electrocatalysts must be considered in the design of enzyme-based fuel cells.[292-296] Using enzymes as fuel cell catalysts has the advantages and disadvantages.[297] *Advantages: (1)* Owing to high selectivity of enzymes for their substrates, fuels and oxidants do not need separating by expensive, ionic-conductivity membranes and they can be supplied to fuel cells as mixtures, thereby decreasing the cost of construction and simplifying and miniaturizing fuel cell setups.[298] *(2)* Many redox enzymes attached to electrodes catalyze electrochemical reactions in the vicinity of the equilibrium potentials for substrate redox couples, resulting in the minimal overpotential requirement that is needed to drive the reactions at useful rates.[299] For example, hydrogenase-2 (Hyd-2), a [NiFe]-hydrogenase from *Escherichia coli*, catalyzes the reversible inter-conversion of H_2 and protons at the equilibrium potential for the $2H^+/H_2$ redox couple, while another [NiFe]-hydrogenase from the same bacterium (hydrogenase-1, Hyd-1) requires an overpotential of about 0.05 V to drive the H_2 oxidation;[254] for the catalysis of the ORR, the BOD requires an overpotential which is about 0.3 V smaller than the overpotential requirement of Pt(111) electrocatalysts.[272] *(3)* Enzymes are renewable, environmentally-friendly catalysts and can be used in a disposable and biodegradable devices.[300] *(4)* Enzyme-based fuel cells enjoy a high level of fuel flexibility: because they are not ‘poisoned’ by the formation of undesirable intermediates such as CO during the multiple-step oxidation of complex fuels, enzyme-based fuel cells can use some organic compounds such as sugars as their fuels.[292] *Disadvantages: (1)* The current/power density produced by an enzyme-based fuel cell is low.[293] The turnover frequency of an enzyme is high – for example, some hydrogenases oxidize H_2 at exceeding 10^4 s^{-1}, comparable to Pt on a per active-site basis.[212] However, enzymes are so large (*e.g.* the maximum molecular diameters of Hyd-1 and BOD are 110 and 70 Å, respectively[263,279]) that the current density (current per unit area) becomes low. *(2)* Enzymes are fragile and very sensitive to the outside ambient conditions such as pH and temperature, thus limiting the stability of enzyme-based fuel cells.[301] *(3)* Though many enzymes have their intrinsic electron relay chains that connect the deeply-buried active sites with the protein surface, such as [NiFe]-hydrogenases and BOD, there still exist some enzymes that lack such efficient electron transfer, thereby resulting in poor electronic contact between enzymes and electrodes.[302] *(4)* The isolation and purification of enzymes are usually time-consuming. For example, it takes over one week to obtain hydrogenase-1 by the processes of bacteria growth and the isolation and purification of the membrane-bound hydrogenases. For those commercially-available enzymes such as BOD, the contained contaminants may impair activity, thus the enzyme needs further purification before use.

To minimize the above-mentioned disadvantages, some effective methods have been presented: *(1)* high-specific-surface-area porous electrodes are used to substantially increase the loading density of enzymes, thus capable of raising catalytic current densities;[303,304] *(2)* immobilization of enzymes on electrodes can improve both the stability of enzyme-based fuel cells and the electron contact between the enzymes and the electrodes.[305-308] The methods of enzyme immobilization include physical adsorption to electrodes, covalent attachment to electrodes, and entrapment in a polymer gel by encapsulation methods exemplified by the sol-gel technique.[309]

In the following paragraphs, the major types of enzyme-based fuel cells classified according to the fuel difference are briefly reviewed. It can be found that the majority of researches into enzyme-based fuel cells focus on the improvement of fuel cell performance, particularly power density and stability, based upon various electrodes and methods for the enzyme immobilization.

Sugar fuel cells – Monosaccharides exemplified by glucose and fructose are frequently used as fuels in enzyme-based sugar fuel cells. Almost all glucose fuel cells use glucose dehydrogenases as anode catalysts and laccase or BOD as cathode catalysts, and dispense with membranes. To achieve good electronic coupling of enzymes to electrodes, many enzyme-based glucose fuel cells employ mediators, such as the redox Os polymers,[310-316] vitamin K_3,[317,318] and ABTS.[319] In these works, control experiments have been conducted to prove that the power densities of enzymatic glucose fuel cells based on mediated electron transfer were higher than the power densities of their counterparts without mediators. However, the fuel cell performance depends on the stability of mediators, the leakage of which would lead to the sharp decrease in the lifetime of fuel cells.[319] Moreover, some enzymatic glucose fuel cells employ high-electrical-conductivity carbonaceous nanostructures such as carbon nanotubes and graphene, on which enzymes are immobilized, to be able to improve the electron contact between enzymes and electrodes, thereby dispensing with mediators.[320-322] The enzyme-based mediator-free fructose fuel cells are achieved by immobilizing fructose dehydrogenases in the matrices of high-sorption carbon nanoparticles KetjenBlack (KB) – single-walled carbon nanotubes – chitosan composite[323] or multi-walled carbon nanotubes – cellulose composite.[324] In an enzymatic mediator-free disaccharide fuel cells, the cellobiose dehydrogenase-gold nanoparticle anode and the BOD-gold nanoparticle cathode are placed into human physiological fluids such as blood and plasma, and the fuel cell can generate the maximum power density of 3 $\mu W \cdot cm^{-2}$ with the half life of up to 2 hours.[325]

One glucose dehydrogenase can only extract 2 electrons from a single molecule of glucose by oxidizing glucose to hydrogen peroxide and glucono delta-lactone, thus the chemical energy stored in the fuel is not fully exploited and the accumulation of hydrogen peroxide may also have a deleterious effect on the glucose dehydrogenase.[326] Therefore, multi-enzyme cascades are used for deep or complete oxidation of biofuels.[327] Zhu and co-workers used a three-enzyme cascade to extract 4 electrons from a single glucose and demonstrated that the glucose fuel cell based on the deep oxidation of glucose produced the power that was 32% higher than the power generated by the one-dehydrongease-based glucose fuel cell.[328] They have recently published a result that nearly 24 electrons per glucose unit of a polysaccharide – maltodextrin are extracted by a synthetic catabolic pathways comprising 13 enzymes.[329] Minteer and co-workers achieved the complete oxidation of glucose to CO_2 by a six-enzyme cascade in a glucose fuel cell.[330] They also extracted 4 electrons from a single molecule of sucrose by a three-enzyme cascade.[331]

One of the potential applications for enzyme-based sugar fuel cells is serving as an implantable power source in living organisms.[332] Implantable enzymatic glucose fuel cells should be able to generate electrical power for implant devices such as *in vivo* biosensors and pacemakers using physiologically-produced glucose as the fuel and O_2 dissolved in physiological fluids as the oxidant. [333,334] Katz and co-workers have implanted enzymatic glucose fuel cells into several living animals, such as snails,[335] clams,[336] lobsters,[337] and rat muscle tissues.[338] The multiple implanted biofuel cells connected in series can power an electrical watch or a micro-pacemaker.[337]

Alcohol fuel cell – Enzyme-based methanol fuel cells usually employed a three-NAD^+-dependent-enzyme cascade to completely oxidize methanol to carbon dioxide occurring either in solution or within a modified Nafion matrix electropolymerized on the surface of carbon electrode; the latter, *i.e.* the methanol fuel cell based on the polymer encapsulation, showed an improved stability.[339,340] Enzymatic ethanol fuel cells typically used a single enzyme system to oxidize ethanol to acetaldehyde or a two-enzyme system to oxidize ethanol to acetate within a polymer matrix for enzyme immobilization.[341-344] Glycerol can be also used as the fuel by enzyme-based fuel cells in which a two-enzyme system is employed to partially oxidize glycerol or a three-enzyme cascade to completely oxidize the fuel.[345,346]

Hydrogen fuel cell – Armstrong and co-workers demonstrated the first enzyme-based H_2 fuel cell.[347] Operated on 3% H_2 in air, this membrane-less fuel cell generated the maximum power density of 5 $\mu W \cdot cm^{-2}$ employing an O_2-tolerant [NiFe]-hydrogenase as an anodic catalyst and laccase as a cathodic catalyst. Further characterization found that such H_2-weak/air-rich mixture could completely inactivate the hydrogenase that was unable to recover spontaneously under low-load conditions.[348] Another enzymatic membrane-less H_2 fuel cell running on a H_2-rich/air-weak mixture (*i.e.* 80% H_2-20% air) produced a maximum power density of 100 μW·cm^{-2} with a half-life of 8 hours, based on the covalent attachment of [NiFe]-hydrogenase and BOD to multi-walled carbon nanotubes on anode and cathode, respectively.[349]

2.4 Outline of this thesis

As mentioned in the last paragraph, the power densities of enzyme-based membrane-less H_2 fuel cells designed to date are still low, at the μW·cm^{-2} level, limited by the low current densities at the electrodes, especially the cathodes; moreover, the lifetime of enzyme-based membrane-less H_2 fuel cells is also comparatively low, with the hour-level half-life. Therefore, in terms of niche, practical applications, it is necessary to substantially increase the power density to the mW·cm^{-2} or even mW·cm^{-3} level and extend the half-time to the level of days for enzyme-based membrane-less H_2 fuel cells.

This thesis contains my independent works during my doctoral study at the Inorganic Chemistry Laboratory under the supervision of Professor Fraser A. Armstrong, on the improvement in the performance of enzyme-based membrane-less H_2 fuel cells, specifically, enhancing the current/voltage/power/stability capabilities of the fuel cells. First, I present a facile, effective method for the construction of three-dimensional (3D) porous carbon electrodes; based upon such 3D electrodes with the re-proportioned cathode/ anode geometric area ratios, the enzyme-based membrane-less H_2 fuel cell has achieved the maximum power density exceeding 1.5 mW·cm^{-2} and its half-time has been extended to over one week under a non-explosive H_2-air condition (Chapter 3). Next, I construct a fuel cell test bed, in which parallel and series connections of sandwich-like electrode stacks can be varied; the effects of electrode microstructures, enzyme concentrations, parallel and series stacking on the current/voltage/power capabilities of the fuel cells have been investigated; such fuel cell test bed running on a non-explosive H_2-air mixture achieves the maximum volumetric power density of over 2 $mW \cdot cm^{-3}$ with the open circuit voltage (OCV) of over 2V, capable of powering some electronic gadgets such as clock and light-emitting device (LED); the test bed has also exhibited a good working stability (Chapter 4). Last, in addition to the substantial increase in the current/power/stability of the for enzyme-based membrane-less H_2 fuel cell, I find out that the 3D porous carbon electrodes can also largely increase the degree of apparent O_2-tolerance of hydrogenases, which has a major impact on the fuel cell performance, and also analyze the mechanism for such increase; as a proof-of-concept experiment, an O_2-sensitive hydrogenase is able to work as an anodic catalyst in an enzyme-based membrane-less H_2 fuel cell based on the 3D porous carbon electrodes (Chapter 5). The work described in Chapter 3 has been published (L. Xu and F. A. Armstrong, *Energy & Environmental Science*, 2013, **6**, 2166-2171), while the works in Chapters 4-5 are in manuscript preparation.

Chapter 3

Improving the performance of enzyme-based membrane-less H_2 fuel cell based on 3D compacted mesoporous carbon electrodes

Abstract

The performance of an enzymatic fuel cell is usually characterized by power density and stability.[297] For enzyme-based membrane-less H_2 fuel cells that have been established so far, the power densities are limited by comparatively low current density at the electrodes as well as unbalanced anodic/cathodic currents due to the explosive limits of H_2 in air.[347,349] In addition, the lifetime of these fuel cells is also relatively short.[349] In this chapter, an enzyme-based membrane-less H_2 fuel cell exhibits the significantly improved performance based on the 3D compacted mesoporous carbon (CMC) electrodes with re-proportioned cathode/anode areas. The CMC electrodes can allow for the large increase in the loading of enzymes, thereby substantially raising the electrocatalytic current densities at both anode and cathode. The current densities at the anode and cathode of the same geometric area can achieve 4.60 ± 0.32 $mA \cdot cm^{-2}$ and 1.23 ± 0.12 $mA \cdot cm^{-2}$, respectively, and the open circuit voltage (OCV) of the fuel cell is 1.07 V under the quiescent condition in the 78% H_2/22% air mixture at 25°C. Moreover, the cathode/anode geometric area ratio is re-proportioned to balance the cathodic and anodic currents, partly making up for the O_2 starvation at the cathode in the H_2-rich/air-weak atmosphere and thus further increasing the power density. The maximum power density of the fuel cell with the geometric area ratio of cathode to anode of 3:1 is 1.67 ± 0.24 $mW \cdot cm^{-2}$, one or two orders of magnitude higher

than other enzyme-based membrane-less H_2 fuel cells. Furthermore, 90% of the power is retained after continuously working for 24 hours and more than half of the power can be retained after the one-week continuous work, showing a good stability of the fuel cell.

3.1 Introduction

Regarding the increase in current density on electrodes, let us recall the methods given in Section 1.3: *(1)* increasing the reactant concentration, *(2)* decreasing the activation energy, and *(3)* increasing the temperature. Compared to conventional fuel cells, these methods do not have desired effects on enzymatic fuel cells. First, each enzyme has a characteristic Michaelis-Menten constant (K_m) for a given substrate and saturation will occur as the substrate concentration increases.[350] Therefore, increasing the reactant (substrate) concentration has a limited effect on the increase in current density for enzymatic fuel cells. However, for enzyme-based H_2 fuel cells, the problem is not concerned with too much substrates and thus ‘saturation’ but is with regard to ‘starvation’. Specifically, *(i)* enzyme electrodes are not ‘dry’ but immersed in aqueous solutions, but the solubility of either H_2 or O_2 in water is very low at ambient conditions; *(ii)* the electrodes of enzymatic H_2 fuel cells should not be rotated or stirred because the power requirement for rotation or stirring far exceeds the power produced by the fuel cell, thus the rates of electrochemical reactions are further limited by the poor mass transport; *(iii)* the mixture of H_2 and O_2 or air has very wide explosive limits – H_2 in O_2 is 4.8 – 95.2% v/v and H_2 in air is 4.9 – 76.5% v/v.[351] Lojou and co-workers used the PEM to separate anode and cathode so that this enzymatic membrane H_2 fuel cell can be supplied with 100% H_2 and 100% O_2 to the corresponding compartments and achieved the maximum power density of 0.3 $mW\cdot cm^{-2}$.[352] However, for the membrane-less H_2 fuel cell, because H_2 and O_2 or air are mixed together in the membrane-less condition, their concentrations must be controlled outside the explosive limits, resulting in the need to use mixtures that are either H_2-weak/O_2 (air)-rich or H_2-rich/O_2 (air)-weak. Both of the extreme conditions result in unbalanced anode/cathode currents and even ‘strangle’ the fuel cell. As mentioned in Section 2.3, the H_2-weak H_2-air mixture could completely inactivate hydrogenases under low-load conditions. At the H_2-rich extreme, such as 80% H_2-20% air, the cathodic kinetics is sharply decreased to merely 4% of the kinetics in 100% O_2 because 20% air only contains about 4% O_2. This severe O_2 starvation has an adverse effect on the further increase in the cathodic current density. In short, the kinetics-related problems of enzyme-based membrane-less H_2 fuel cells lie in meagre, unbalanced substrates and poor mass transport of substrates. Secondly, enzymes are inherently efficient catalysts, but the ‘footprints’ of enzymes are so large that the electrode surface is not effectively exploited, thus the current/power densities of enzymatic fuel cells are not comparable to those produced by their conventional counterparts. Thirdly, enzymes are fragile proteins which are very sensitive to temperature, thus increasing temperature provides a very limited increase potential for the current/power density.

On the basis of the above-mentioned analyses, one effective way of increasing the current density (generally normalized by geometric electrode area) is to increase reaction sites per unit geometric electrode area, partly making up for the large footprints of enzyme molecules on electrode surface and the low reaction kinetics due to meagre, unbalanced substrates, poor mass transport, and low temperature. For an electrode with a highly rough surface, the real electrode surface area could be orders of magnitude larger than its geometric electrode area.[353] Therefore, increasing the roughness of an electrode can increase the real electrode surface area and thus accommodate more enzymes (*i.e.* more reaction sites) per unit geometric electrode area. The ratio of real electrode surface area to geometric electrode area, termed *roughness factor*[51] or *electrode area ratio*,[353] reflects the roughness of an electrode and the order of the increase in real electrode surface area. Electrodes with a high specific surface area usually have a large roughness.[354,355] Electrode materials with a high specific surface area such as carbon[356-360] and gold[361-363] micro/nano-structures and carbon matrices[364-366] have been used in enzymatic sugar fuel cells to increase catalytic current densities and improve stability and electronic contact. The extreme case is a '3D' electrode able to accommodate a high density of immobilized macromolecules while providing free access for the small fuel and oxidant molecules. A rough internal surface also leads to a high probability of there being good electronic contact between the electrode material and electron entry/exit points in the enzymes. Here, a facile, effective method for the construction of 3D porous carbon electrodes is presented. This kind of 3D electrodes is constructed easily by compacting powder forms of certain carbon micro/nano-materials (mesoporous carbon for this chapter) into discs using reasonable pressures in a hydraulic press (see Figure 3.1).

Based on the 3D compacted mesoporous carbon (CMC) electrodes, the performance of enzyme-based membrane-less H_2 fuel cell has been improved by physically incorporating O_2-tolerant [NiFe]-hydrogenase-1 from *Escherichia coli* (Hyd-1) and bilirubin oxidase (BOD) from *Myrothecium verrucaria* into the CMC electrodes (anode and cathode, respectively) and scaling the relative sizes of anode and cathode to compensate for low O_2 levels and balance electrocatalytic activities. The fuel cell achieves the maximum power density of 1.67 ± 0.24 $mW \cdot cm^{-2}$ with a half-time of one week, using H_2 mixed with a small proportion of air (containing only 4.6% O_2).

Figure 3.1. The photograph of a hydraulic press and a pellet die for the construction of 3D porous carbon electrodes.

3.2 Surface area and pore size distribution of the 3D CMC electrodes

Surface area and pore size distribution are important properties of fuel cell electrodes. Electrodes with a higher specific surface area (*i.e.* larger roughness) allow for more reaction sites per unit geometric electrode area. As far as mass transport is concerned, the pore size distribution of the fuel cell electrodes is a more critical parameter for mass transport within the electrode than the porosity itself.[367] Furthermore, for enzyme-based fuel cells, the pore sizes of electrodes must be large enough to accommodate macromolecule enzymes. Figure 3.2 shows the nitrogen adsorption-desorption isotherm of

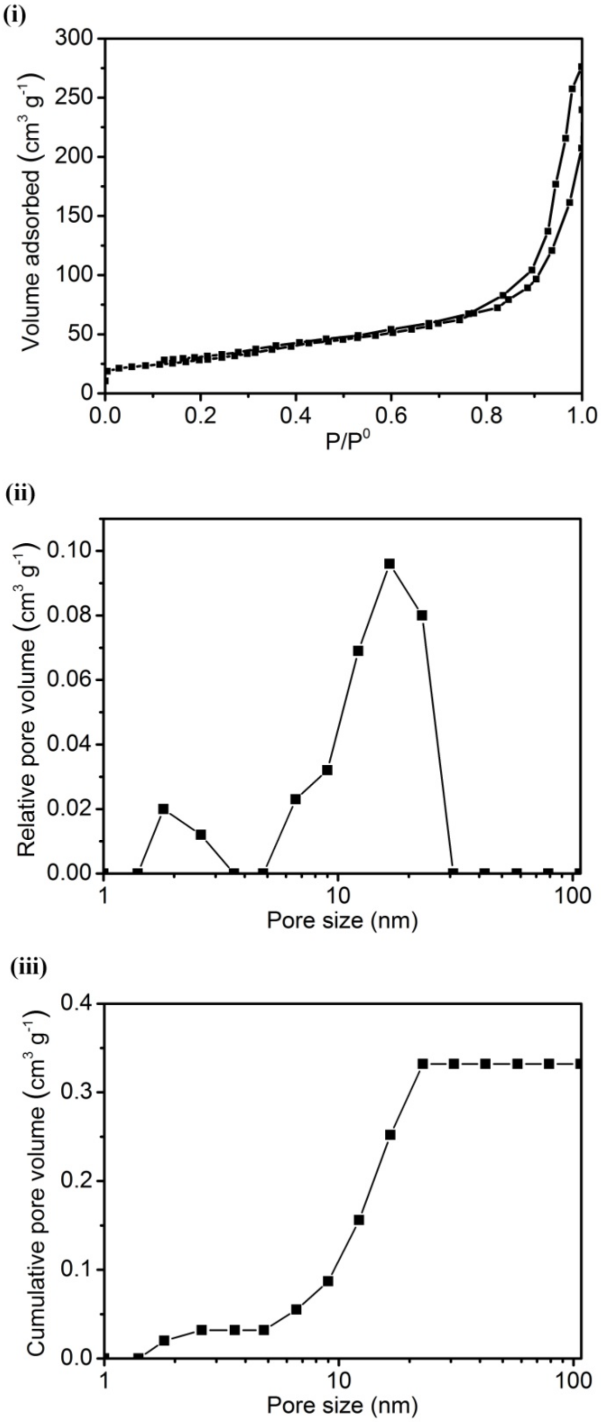

Figure 3.2. (i) Nitrogen adsorption and desorption isotherms for the 3D CMC electrode. (ii and iii) BJH pore size distribution for the 3D CMC electrode.

the 3D CMC electrode. This N_2 adsorption-desorption isotherm exhibits the hysteresis loop associated with capillary condensation occurring in mesopores, which is the characteristic feature of the Type IV curve.[368] Based on the Brunauer-Emmett-Teller (BET) method, the specific surface area of the 3D CMC electrode is calculated to be 105 $m^2 \cdot g^{-1}$. Such value can be considered as a high specific surface area for electrodes of fuel cells and other electrochemical energy conversion devices.[369,370] Figures 3.2(ii)-(iii) show the relative and cumulative pore size distributions of the 3D CMC electrode based on the Barrett-Joyner-Halenda (BJH) model. The pore volume of the 3D CMC electrode is 0.33 $cm^3 \cdot g^{-1}$ and the porosity is 15%. The volume of those pores having diameters larger than 10 nm is 0.25 $cm^3 \cdot g^{-1}$, constituting 76% of the total pore volume of the 3D CMC electrode. As mentioned in Section 2.3, the maximum molecular diameters of Hyd-1 and BOD are 11 nm and 7 nm, respectively. Therefore, about three quarters of the pores of the 3D CMC electrode are large enough to be permeable to and accommodate Hyd-1 and BOD.

3.3 Anodes and cathodes having the same geometric areas

In the membrane-less fuel cell setup, the Hyd-1-modified CMC anode and the BOD-modified CMC cathode are positioned in a face-to-face, coaxial manner at a distance of 5 mm, as shown in Figure 3.3. Both the anode and the cathode have the same geometric area (0.2 cm^2) and the thickness of 0.90 mm. Figure 3.4 shows cyclic voltammograms (CVs) of the Hyd-1-modified CMC anode and the BOD-modified CMC cathode having the same geometric area (0.2 cm^2) under various, quiescent conditions at 25°C and pH 6.0. The

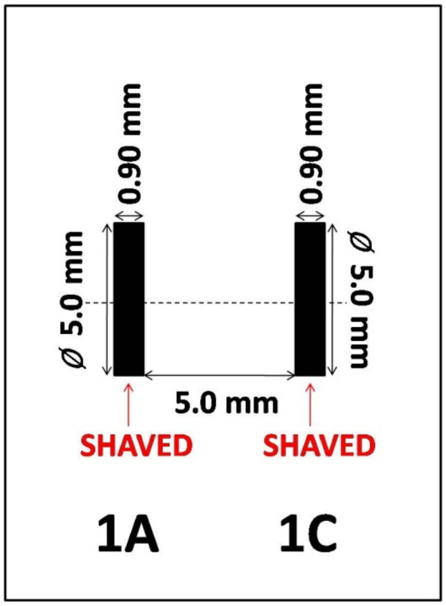

Figure 3.3. A schematic representation of how the Hyd-1-modified anode and the BOD-modified CMC cathode are positioned in the fuel cell. 1A and 1C mean that the anodic and cathodic geometric areas are the same. The depths to which the electrodes were shaved to expose the internal population of enzyme molecules are indicated in red colour.

black CVs are obtained with the Hyd-1-modified CMC anode and the BOD-modified CMC cathode having the same thickness (0.90 mm) under membrane-less, quiescent conditions in a 78% H_2/22% air mixture. Under the large excess of H_2 over O_2, the current density at the anode is much higher than that measured at the cathode. Hyd-1 undergoes O_2-inhibition at high potential, but the enzyme can reactivate rapidly from the Ni-B state. The maximum current densities of the Hyd-1-modified CMC anode and the BOD-modified CMC cathode attain average values of 4.60 ± 0.32 $mA{\cdot}cm^{-2}$ and 1.23 ± 0.12 $mA{\cdot}cm^{-2}$, respectively (standard deviations for five separate experiments, the same below).

In the absence of the modified enzymes (red solid) or without the gas substrates (red dash), there are no catalytic currents, as shown in Figure 3.4.

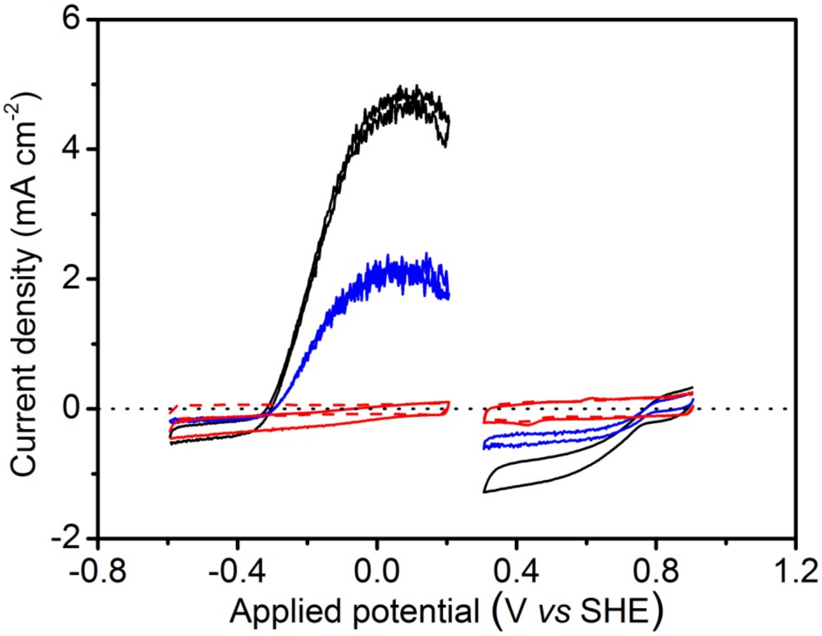

Figure 3.4. CVs of a Hyd-1-modified CMC anode and a BOD-modified CMC cathode having a thickness of 0.90 mm (black), whereas those obtained after shaving off the upper half of the already-modified electrodes with a scalpel, resulting in electrodes with a thickness of 0.45 mm, are shown in blue. These voltammograms were recorded under a 78% H_2/22% air atmosphere. For the blank voltammograms, those under a 78% H_2/22% air atmosphere without the modified enzymes are shown in red solid while those under 100% N_2 atmosphere with the modified enzymes shown in red dash. All the voltammograms were recorded under membrane-less, quiescent conditions at 25°C (scan rate: 1 mV·s^{-1}) in 0.1 M sodium phosphate buffer (pH 6.0).

The integrated (average) rates are estimated for each enzyme based on the total amounts applied to each electrode (0.8 nmole Hyd-1 based on RMM = 100 kDa and 1.6

nmole BOD based on RMM = 50 kDa) as given in Section 3.6. For Hyd-1, a calculation based on a current density of 4.60 $mA \cdot cm^{-2}$, an electrode area of 0.2 cm^2 and 0.8 nmole Hyd-1 applied to the electrode gave an average rate of 6 molecules $H_2 \cdot s^{-1}$. For BOD, a calculation based on a current density of 1.23 $mA \cdot cm^{-2}$, an electrode area of 0.2 cm^2 and 1.6 nmole BOD applied to the electrode gave an average rate of 0.4 molecule $O_2 \cdot s^{-1}$. These values are well below the expected turnover frequencies, because *(i)* they are an average for *all* enzyme molecules, including those deeply buried below the electrode surface, *(ii)* the quiescent condition without rotating or stirring results in poor mass transport, *(iii)* the value for BOD (measured at only 4.6% O_2) will be in any case be only a small fraction of the maximum rate, and moreover, O_2 diffuses much more slowly than H_2, which will be discussed in detail in Chapter 5.

To establish that the enzymes permeated well into the internal CMC electrodes, the enzyme-modified CMC electrodes were shaved to 50% thickness (0.45 mm) thus exposing the catalyst that had permeated to this depth (see Figure 3.3). The resulting CVs (blue in Figure 3.4) retained 40-50% of the original electrocatalytic current densities, thus confirming that the enzymes permeate deeply into interior CMC electrodes. The penetration is important, not only for the practical purposes of greatly enhancing catalyst loading, but also for providing the internal porous channels of the electrodes for the mass transport of reactants and products because enzyme penetration indicates that the porous channels in the CMC electrodes are interconnected and open to surface.

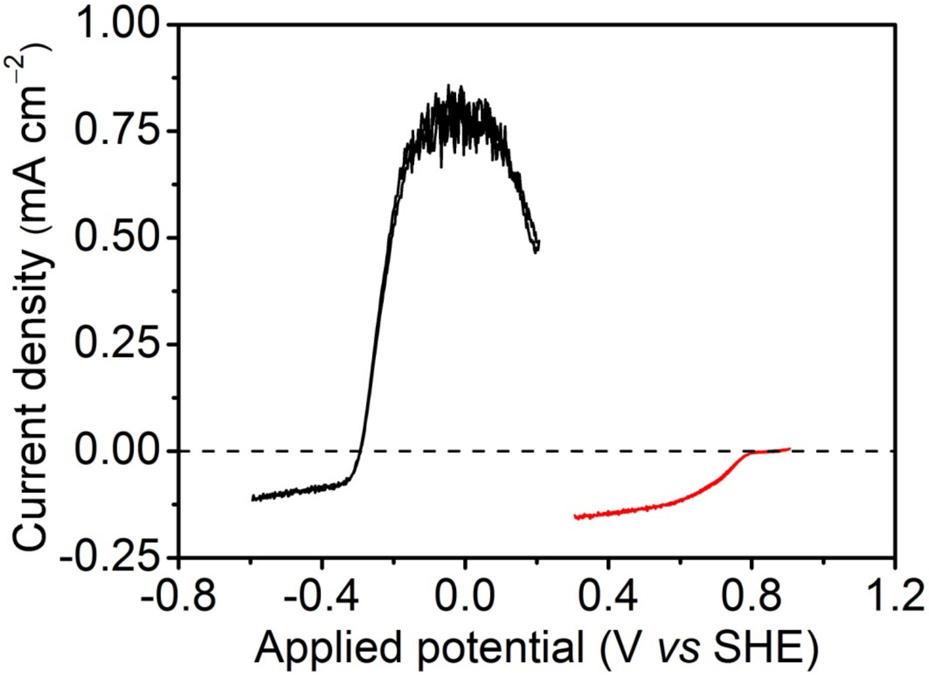

Figure 3.5. CVs of the Hyd-1-modified mesoporous carbon-deposited anode (black) and the BOD-modified mesoporous carbon-deposited cathode (red) under a 78% H_2/22% air mixture. Other conditions: temperature 25°C, scan rate: 1 mV·s^{-1}, 0.1 M sodium phosphate buffer (pH 6.0).

A non-CMC electrode is constructed by grinding a pyrolytic graphite 'edge' (PGE) electrode into graphitized mesoporous carbon nanopowder. The mass of mesoporous carbon deposited on the PGE electrode is approximately one tenth of the mass of mesoporous carbon for the typical CMC electrode (*i.e.* geometric area: 0.2 cm^2, thickness: 0.90 mm), thus the real electrode surface area and pore volume of the mesoporous carbon-deposited electrode are 10% of the real electrode surface area and pore volume of the CMC electrode. Figure 3.5 shows the CVs of the Hyd-1-modified mesoporous carbon-deposited anode and the BOD-modified mesoporous carbon-deposited cathode under a 78% H_2/22%

air mixture. Compared to the CMC electrode, the anodic and cathodic current densities for the mesoporous carbon-deposited electrodes were decreased to 0.75±0.09 mA·cm^{-2} and 0.15±0.02 mA·cm^{-2}, respectively. In other words, the anodic current density decreases by 84% and the cathodic current density decreases by 88% when the CMC electrodes are replaced by the mesoporous carbon-deposited electrodes, further indicating that the large loading density of enzymes due to large surface area and pore volume of electrodes leads to the increase in current density at the electrodes.

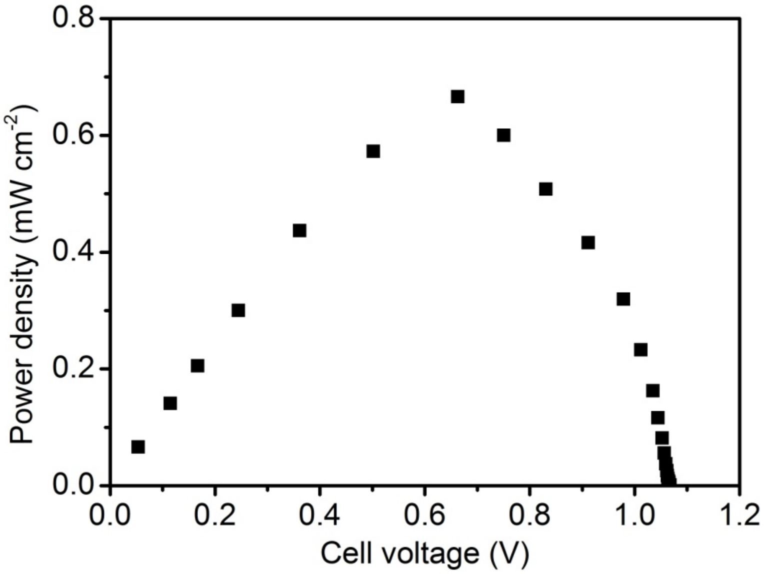

Figure 3.6. Dependence of power density on the cell voltage of the enzymatic membrane-less H_2 fuel cell composed of Hyd-1-modified CMC anode and BOD-modified CMC cathode, each having the same geometric area (0.2 cm^2) and the same thickness (0.90 mm). Experimental conditions: 78% H_2/22% air, temperature: 25°C, 0.1 M sodium phosphate buffer (pH 6.0).

Figure 3.6 shows the dependence of power density on the cell voltage of the enzymatic membrane-less H_2 fuel cell composed of the Hyd-1-modified CMC anode and the BOD-modified CMC cathode of the same geometric area (0.2 cm^2) and the same thickness (0.90 mm) under the quiescent condition in a 78% H_2-22% air mixture at 25°C and pH 6.0. The open circuit voltage (OCV) of the fuel cell is 1.068±0.002 V and the maximum power density is 0.664 ± 0.076 $mW{\cdot}cm^{-2}$, which is at least six times as high as the maximum power density produced by other enzyme-based membrane-less H_2 fuel cells.

3.4 Anodes and cathodes having re-proportioned geometric area

Owing to meagre O_2 in the non-explosive H_2-rich H_2-air mixture, the power density of enzymatic membrane-less H_2 fuel cells is severely limited by the cathodic current. One effective way of minimizing this problem is to re-proportion the cathode/anode geometric area ratio to balance the cathodic and anodic currents under the H_2-rich/air-weak condition. This prediction was evaluated using the CMC cathodes having two (2C) and three times (3C) the geometric area of the original (1C) (the resulting fuel cells are denoted 1A/1C, 1A/2C, 1A/3C in increasing order of cathode size), as shown in Figure 3.7.

Figure 3.8(i) shows the CVs of the BOD-modified 1C, 2C, and 3C electrodes under a quiescent 78% H_2/22% air mixture at 25°C. The current at the cathode increases with the increase in the cathode area, although the current does not double in magnitude for the 2C, nor does it triple for the 3C: the non-linear scaling most likely reflects the increased contribution of edge effects with the smaller electrode and the spherical rather than linear mass transport of reactants to microelectrodes. Power density curves for the 1A/2C and 1A/3C fuel cells are shown in Figure 3.8(ii). Operated under a 78% H_2/22% air mixture at 25°C, the power densities of the 1A/2C and 1A/3C fuel cells attain maxima of 1.17 ± 0.15 $mW \cdot cm^{-2}$ and 1.67 ± 0.24 $mW \cdot cm^{-2}$, respectively. These values, achieving the $mW \cdot cm^{-2}$ level, are much higher than the 1A/1C fuel cell (see Figure 3.6) and at least an order of magnitude higher than previous membrane-less enzymatic H_2 fuel cells.

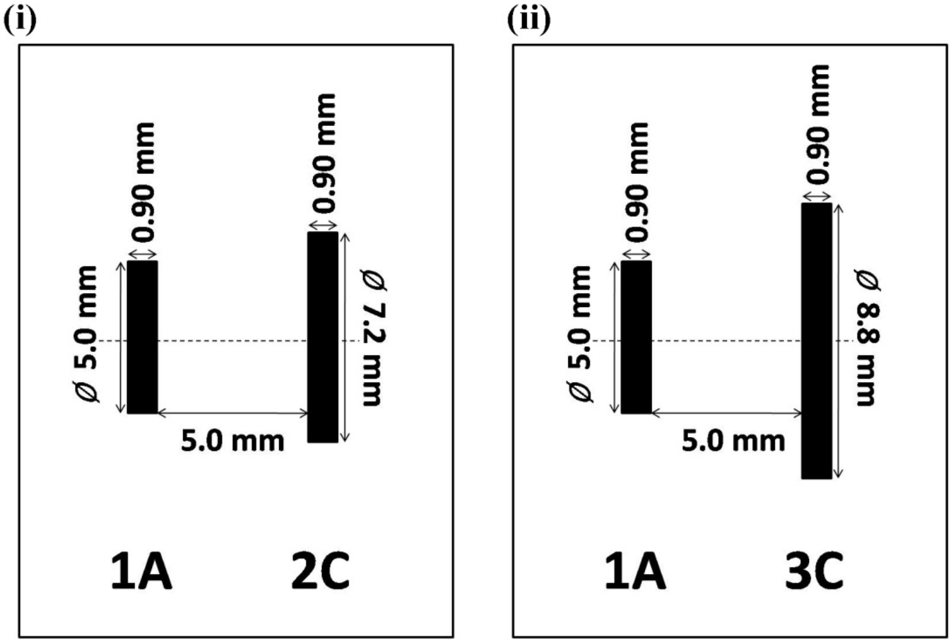

Figure 3.7. Schematic representations of the Hyd-1-modified CMC anodes and the BOD-modified CMC cathodes having the re-proportioned geometric areas in the 1A/2C and 1A/3C fuel cells.

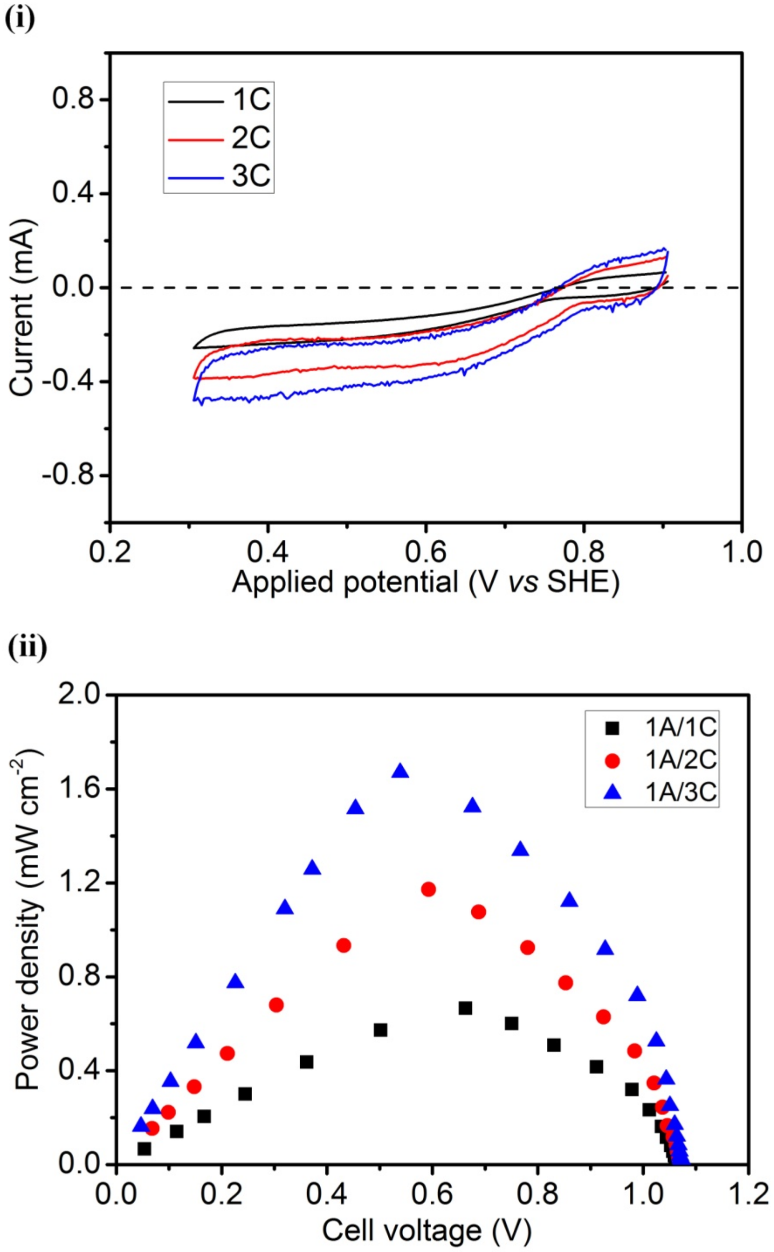

Figure 3.8. (i) CVs of the BOD-modified 1C (black), 2C (red), and 3C (blue) cathodes under quiescent conditions of a 78% H_2/22% air mixture at 25°C (scan rate: 1 mV·s^{-1}). Electrode dimensions are as shown in Figure 3.7. The electrolyte is 0.1 M sodium phosphate buffer at pH 6.0. (ii) Dependence of power density on the cell voltage of the 1A/1C (black), 1A/2C (red) and 1A/3C (blue) fuel cells. Experimental conditions: 78% H_2/22% air, temperature: 25°C, 0.1 M sodium phosphate buffer (pH 6.0).

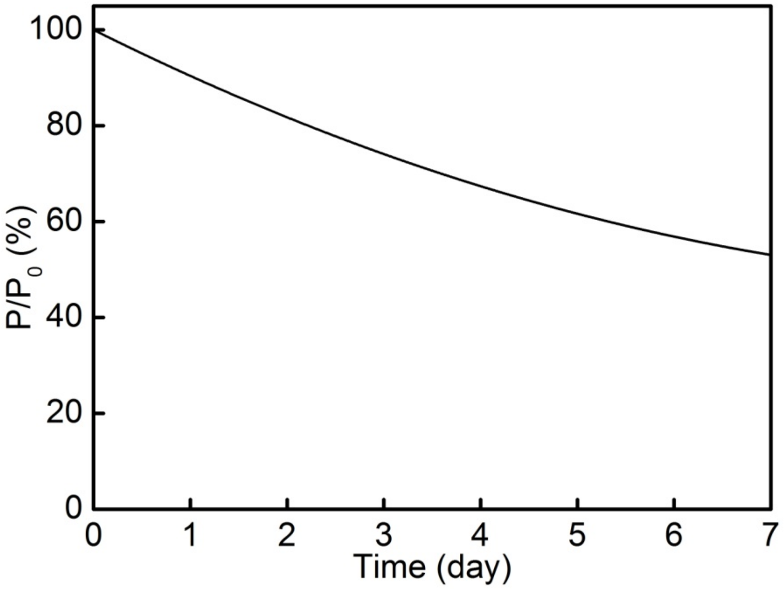

Figure 3.9. Dependence of relative stability of power (%) on time for the 1A/3C fuel cell at an applied constant potential of 0.8 V under a quiescent, 78% H_2/22% air mixture at 25°C in 0.1 M sodium phosphate buffer, pH 6.0.

The power output of the 1A/3C fuel cell was monitored at a constant potential of 0.8 V over a continuous period of one week, as shown in Figure 3.9. Good prospects for stability are demonstrated by the fact that 90% of the power was retained after continuously working for 24 h and 54% of the power was retained after 7 days of non-stop operation. The half-time of the enzymatic membrane-less fuel cell is thus extended to one week. It is worth mentioning that this stability is achieved without the assistance of covalent coupling or polymer encapsulation, just by the physical adsorption of enzymes to the 3D CMC electrodes. This improved stability of the fuel cell is due to the 3D structure of the CMC electrodes and large loading density of enzymes: *(i)* enzyme molecules that are located at deeper levels are less likely to desorb, and *(ii)* the current becomes limited by the mass transport of dissolved gases instead of the loading of enzymes so that either inactivation or desorption of enzymes would not have the major effect on the current output. This phenomenon can be also observed in conventional fuel cells using Pt-based catalysts: catalyst desorption also occurs in conventional fuel cells, but the loading of Pt is so large that instability is not a problem during normal operation.[55]

3.5 Conclusions

This chapter exhibits that the power density and lifetime of enzyme-based membrane-less H_2 fuel cells have been substantially increased based on a type of 3D porous carbon electrodes, which can be constructed by compacting graphitized mesoporous carbon nanopowder in a hydraulic press. Owing to the large roughness and the 3D structure (depths) of the electrodes, the CMC electrodes can largely increase the loading density of enzymes (*i.e.* reaction sites per unit geometric electrode area). Such large enzyme loading brings about at least two advantages: *(1)* both the anodic and cathodic current densities are substantially increased, and *(2)* the apparent stability of the fuel cell is remarkably improved. Moreover, because of the unusual H_2-rich H_2-air mixture due to the wide explosive limits for aerobic H_2 mixtures, the power densities of the enzyme-based membrane-less H_2 fuel cells are severely limited by the cathodic electrocatalytic activity. The power density of the fuel cell can be further increased by re-proportioning the cathode/anode geometric area ratio to balance the cathodic and anodic currents under the non-explosive H_2-rich/air-weak mixture. Based on the 3D CMC anodes and cathodes having re-proportioned geometric areas, the maximum power density of the enzyme-based membrane-less H_2 fuel cell achieves the mW·cm^{-2} level and the half-time is extended to one week in the H_2-rich H_2-air mixture containing merely 4.6% O_2, which have demonstrated the best performance to date in enzyme-based membrane-less H_2 fuel cells. The methods presented in this chapter should be also meaningful to other types of enzymatic fuel cells which meet the same or similar challenges in an effort to improve the fuel cell performance.

3.6 Methods

Materials: Graphitized mesoporous carbon nanopowder was purchased from Sigma-Aldrich and used without further purification. Hyd-1 from *Escherichia coli* was isolated and purified as described previously.[254] Bilirubin oxidase from *Myrothecium verrucaria* was purchased from Amano Enzyme Inc and further purified by hydrophobic interaction chromatography with a HiTrap Phenyl HP hydrophobic column (GE Healthcare). Sodium dihydrogen orthophosphate and di-sodium hydrogen orthophosphate were purchased from Fisher Scientific and used to prepare the sodium phosphate buffer solution. The pyrolytic graphite ‘edge’ (PGE) electrode bases were made of pyrolytic graphite blocks (Momentive Performance Materials Ltd) and used as the mechanical support and electrical conduction for the CMC electrodes. Conductive silver paint (Agar Scientific) was used to glue the CMC pellet to the PGE electrode base. All aqueous solutions were prepared using deionized water from a Milli-Q water system (18 MΩ·cm).

Instrumentation: Electrochemical measurements were performed on an Ivium potentiostat (CompactStat, Ivium technologies) in a membrane-less fuel cell setup as described previously[349]. All potentials were adjusted to the standard hydrogen electrode (SHE) using the relationship $E_{SHE} = E_{Ag/AgCl} + 0.206$ V at 25°C. Power measurements were obtained by varying the applied load and recording the potential in each case (Keithley 195A digital voltmeter). The distance between the anode and the cathode was fixed at 5 mm. The ratios of H_2 to air were controlled by two mass flow controllers (Sierra instruments). A Sorptomatic 1990 instrument (CE Instruments) was used to acquire N_2 adsorption-desorption isotherms at 77K. The BET surface area was calculated from the linear portion of the BET plot. The pore size distribution plots were obtained using the BJH model.

Fabrication of the CMC electrodes and other electrodes: A quantity (50 mg) of graphitized mesoporous carbon nanopowder was placed in a pellet die (Specac) and subjected to a pressure of 0.2 tonnes using a hydraulic press (Specac). The CMC electrode disc was then cut to size for the required geometric area and attached to the PGE electrode base using conductive silver paint. After the paint was dry, 20 µL of Hyd-1 ($4\ mg \cdot mL^{-1}$) and 20 µL of BOD ($4\ mg \cdot mL^{-1}$) for 1C or 40 µL of BOD for 2C or 60 µL of BOD for 3C were applied to the CMC electrodes to form the Hyd-1-modified CMC anode and the BOD-modified CMC cathode respectively. The enzyme-modified CMC electrode was subsequently placed in a cold room (4°C) for 2 h to allow sufficient permeation of enzymes into the electrodes before starting the electrochemical characterization and fuel cell tests. To prepare carbon-deposited electrodes, a PGE electrode base was ground into graphitized mesoporous carbon nanopowder contained in a weighing boat (the nanopowder adheres so strongly to the PGE electrode by physical adsorption that it is not removed even by a high-pressure torrent of water). After the electrode was rinsed with deionized water, 20 µL of Hyd-1 (4 mg·mL^{-1}) or 20 µL of BOD (4 mg·mL^{-1}) were dropped onto the carbon-deposited electrode, which was subsequently placed in a cold room (4°C) for 2 h before the electrochemical experiments. The ‘shaved’ electrodes were prepared by cutting across the modified CMC electrodes cleanly with a scalpel, using a vernier calliper to control the thickness.

Chapter 4

A test bed for enzyme-based membrane-less H_2 fuel cells

Abstract

In this chapter, a test bed in which series and parallel connections of sandwich-like electrode stacks can be varied is constructed for investigating the current/voltage/power/ stability/parallel-series-connection capabilities of enzyme-based membrane-less H_2 fuel cells running on a non-explosive H_2-air mixture. Based on the method for the construction of 3D porous carbon electrodes introduced in Chapter 3, three 3D compacted porous carbon (CPC) electrodes with varied specific surface areas and pore size distributions are constructed by compacting powder forms of graphite (GT), multi-walled carbon nanotube (CNT), or the mixture of the two carbon allotropes in this chapter. The characterizations of the 3D CPC electrodes exhibit how the electrode microstructures influence catalytic current outputs. Moreover, the effects of parallel and series connections on the current/voltage/power output characteristics are studied in the fuel cell test bed. Operating under a 78% H_2-22% air mixture at 20°C, the maximum volume power density of the fuel cell test bed exceeds 2 $\mathrm{mW \cdot cm^{-3}}$ at the cell voltage of 1.22 V, capable of powering some electronic gadgets with a good working stability.

4.1 Introduction

As discussed in Chapter 1, the open circuit voltage (OCV) of a single fuel cell is 1 V or lower and the cell voltage is typically 50-70% of the OCV when the power output of the fuel cell reaches its maximum. Generally, the output voltage of a single fuel cell is 0.6-0.8 V under external loads, while the majority of the applications require more than 1 V. Moreover, though the current density has been largely increased due to the 3D porous carbon electrodes (Chapter 3), the current output of a single fuel cell is still limited in terms of practical applications. To elevate the currents and voltages of enzyme-based membrane-less H_2 fuel cells, multiple single cells need connecting in parallel and series into a fuel cell stack to achieve a required voltage and current output. In a parallel connection, the total current is the summation of the currents flowing through each component, while the voltage across each component is the same; in a series connection, the total voltage is the summation of the voltages across each component, while the current through each component is the same.[371]

There are very few publications on the parallel and series connections of enzymatic fuel cells, while many microbial fuel cells (MFCs) involve the study of parallel and series connections. Therefore, the MFCs are referred in terms of the designs of the effective fuel cell stacking. The main stacking configurations of scaled-up microbial fuel cells are shown in Figure 4.1. The major four types are: *(1)* Simply connecting individual cells by external wires (see Figure 4.1(i)).[372-375] This stacking arrangement is relatively straightforward to construct and operate, but the setup volumes of fuel cell stacks and the ohmic resistances of electrical interconnects between the component cells are relatively large (the resistance should be reduced by using as short, high-conductivity external wires as possible). *(2)* Planar-bipolar Stacking.[376-379] There are two ways of planar-bipolar arrangements – anodes and cathodes are supported on either side of bipolar plates (see Figure 4.1(ii)) and ionic-conductivity membranes (see Figure 4.1(iii)). The functions of bipolar stacking include separating the fuel and oxidant and conducting electrons between adjacent cells (for plates) or ions between anode/cathode compartments (for membranes). Bipolar plates are generally made of graphite or non-toxic metal. Graphite is chemically stable and highly electrical conductive, but the processing cost of graphite is expensive and the brittle characteristic of graphite also adds to the difficulties of construction, whereas non-toxic and inexpensive metal materials, such as aluminium, stainless steel, and nickel, have higher electrical conductivity and are easier to process than graphite. The advantage of using metal as bipolar pate materials is the minimized ohmic loss, while the disadvantage lies in the relatively poor corrosion resistance, which influences the long-term working stability of fuel cells (but for enzymatic fuel cells, the stability-limiting factor is the relatively short active 'lifetime' of enzymes, thus making the disadvantage less severe). *(3)* Tubular cell stacks (see Figure 4.1(iv)).[380-384] In tubular stacking, fuels flow through the inside of the tube and oxidants through the outside of the tube, and vice versa. The advantage of tubular cells is the good sealing and structural integrity of the cells (for enzymatic fuel cells, because of high specificity of enzymes, fuels and oxidants need not be separated, thus making the sealing between fuels and oxidants unnecessary), while its disadvantages are notable, that is, complicated construction processing and relatively large ohmic resistance. According to the advantages and disadvantages of the above-mentioned stacking arrangements of MFCs combined with the characteristics of enzymatic fuel cells, a ‘monopolar’ stacking is presented in this chapter, in which double-coated anode/cathode stacks are alternatively arranged in a single compartment. This stacking-arrangement test bed for membrane-less enzyme hydrogen fuel cells can miniaturize the volume of cell setup, minimize ohmic fuel cell losses, and make enzyme-modified enzymes work under the optimized conditions.

In Chapter 3, it has been demonstrated that the 3D CMC electrodes can substantially increase the power densities of enzyme-based membrane-less H_2 fuel cells by raising the loading density of enzymes on the electrodes. The large enzyme loading at the 3D CMC electrode can also improve the apparent stability of the fuel cell because the electrode act as a buffer against inactivation or desorption when the current is largely determined by mass transport of dissolved gases. In this chapter, the ‘compacting’ method is applied to construct new 3D compacted porous carbon (CPC) electrodes, in which the pore sizes are not limited to the mesoporous dimension. The effect of porous structures of the 3D CPC electrodes on the catalytic currents is studied in the fuel cell test bed. Moreover, the current/voltage/power capabilities of parallel and series connections are investigated in the test bed. Based on the compacted 60% GT-40% CNT electrodes, the fuel cell test bed running in a 78% H_2-22% air (~4.6% O_2) atmosphere has achieved the maximum volume power density of 2.09 ± 0.03 mW·cm^{-3} at the cell voltage of 1.22 V, capable of powering some electronic gadgets such as clock and light-emitting devices (LEDs) with the good working stability.

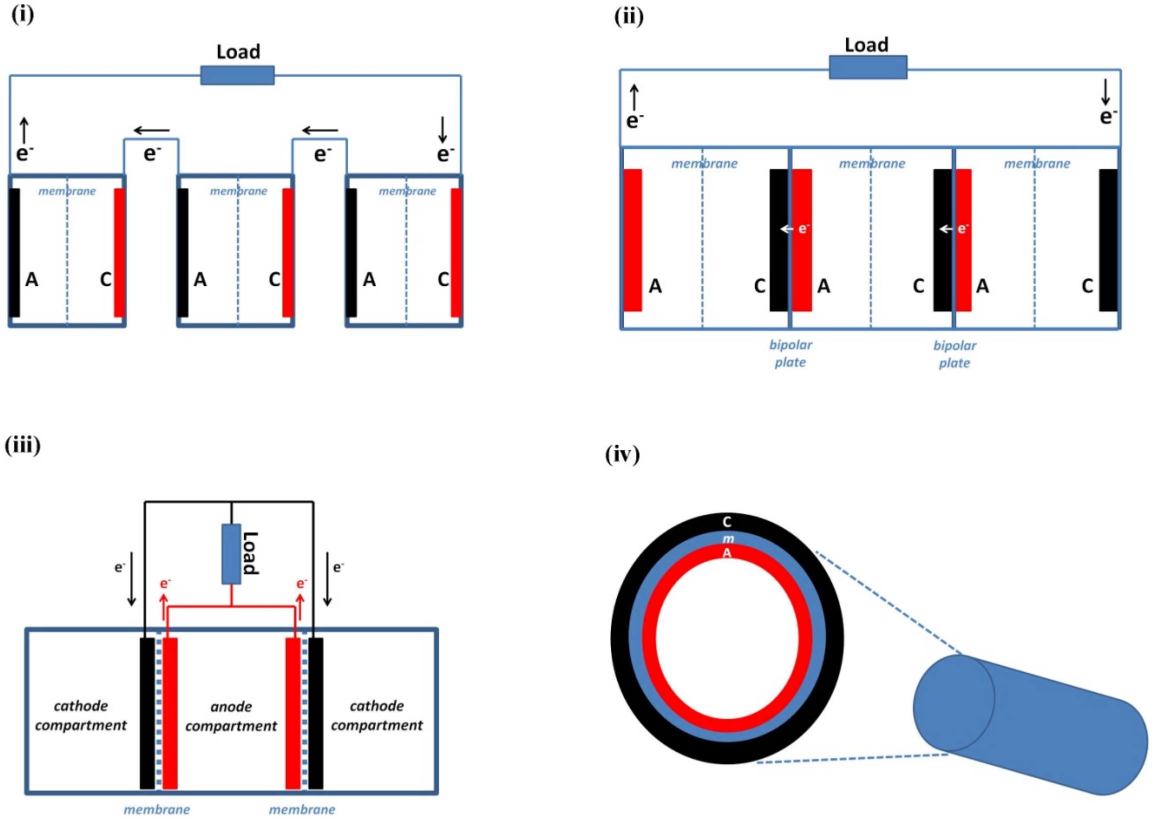

Figure 4.1. Schematic diagrams of (i) connecting individual cells by external wires, (ii) planar-bipolar plate stacking, (iii) bipolar stacking by ionically-conductivity membranes, and (iv) tubular cell stacking. (A = anode, C = cathode, m = membrane, e^{-} = electron)

4.2 Structure of the test bed

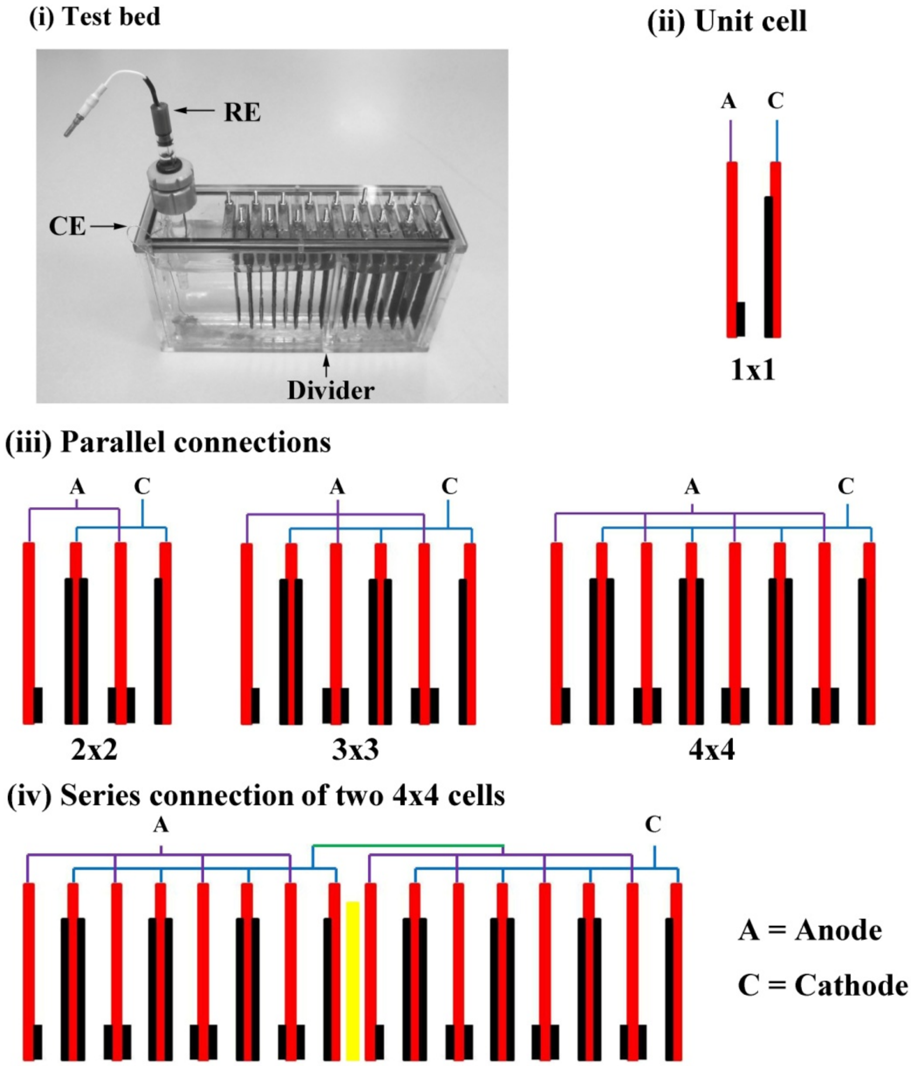

Figure 4.2. (i) Photograph of the test-bed electrode stacks (CE = counter electrode, RE = reference electrode). The schemes for the unit cell (1x1) (ii), the parallel stacks (2x2, 3x3, 4x4) (iii), and the series stack (iv). The colour representations: *red* – metal plates, *black* – 3D CPC electrodes, *yellow* – divider.

As shown in Figure 4.2(i), the test bed consists of 16 rectangular metal plates (1.5 cm × 5 cm) with a narrow gap of 0.5 cm. The 3D CPC electrodes can be attached to either side of the plate by conductive glue. So the plate serves as both electrode supporter and current collector and connector. To describe the structure and functions of the test bed, it is divided into three parts: unit cell, parallel connections, and series connection. The unit cell (denoted as 1x1), with the volume of 3.75 cm^3, contains one anodic plate and one cathodic plate (see Figure 4.2(ii)). As discussed in the last chapter, because the power density of an enzyme-based membrane-less hydrogen fuel cell is limited by the low cathodic current density due to meagre O_2 and slow O_2 diffusion in a non-explosive H_2-rich H_2-air mixture, the cathode/anode geometric area ratio needs re-proportioning to balance the cathodic and anodic currents. The geometric area ratio of cathode to anode can reach up to 5:1 in each unit cell of this test bed. In parallel connections, 2, 3, 4 anodic plates and 2, 3, 4 cathodic plates can form fuel cells (denoted as 2x2, 3x3, 4x4) containing the 3, 5, 7 unit cells, respectively (see Figure 4.2(iii)). *N* anodic plates and *n* cathodic plates generally make up *n* fuel cells, while the same number of plates in this test bed can form 2*n*-1 cells, showing that the alternatively-arranged, double-sided electrode stacks can constitute more fuel cells per unit volume (when *n*>1) and thus utilize space more effectively. To achieve series connection in the test bed, a divider needs applying to separate the electrolyte solution (see Figure 4.2(iv)). Note that it is the solution rather than the whole test bed that is separated; in other words, the upper part of the inner test bed still communicates. The reasons for this design are – separating the electrolyte solution allows both sides of the divider to become ionic insulation and thereby makes the series connection feasible, while leaving space in the upper part is for the need of Hyd-1 activation. The reductively activation of Hyd-1 is controlled by a three-electrode system in which the reference and counter electrodes are set up at one side of the divider in the test bed (see Figure 4.2(i)). Before the activation of Hyd-1, the solution level must be raised to overflow the divider and thus the electrolyte solution at each side of the divider become interconnected so that the three-electrode system can cover both sides of the divider. After the Hyd-1 activation, the solution level is lowered to form two individual cell stacks without sharing the electrolyte, ready for the series connection. To some extent, this kind of divider functions like a ‘weir’ in hydraulic engineering. In this chapter, volume power density is used to gauge the power output of the test bed. Compared to the power density that is usually normalized to geometric electrode area, the volumetric terms are more important for miniaturized fuel cells because we can learn how big a device is required for a certain amount of power. The volume power density is normalized with respect to the volume of the unit cell.

4.3 Characterizations of the 3D CPC electrodes

The 3D CPC electrodes are made by compacting powder forms of GT, CNT, or the mixture of the two carbon allotropes with various ratios. Thickness is an important characteristic of 3D electrodes. For the 3D CPC electrodes, thickness is dependent on mass under a fixed pressure. As shown in Figure 4.3, there is a good linear relationship between the thickness and the mass of the 3D CPC electrodes under the pressure of 0.5 tonnes. These plots can be used to control the thickness of a 3D CPC electrode and get the electrode with a required thickness. In this chapter, the thickness of the 3D CPC electrodes is selected as 0.3 mm. The reasons are given in Section 5.7.

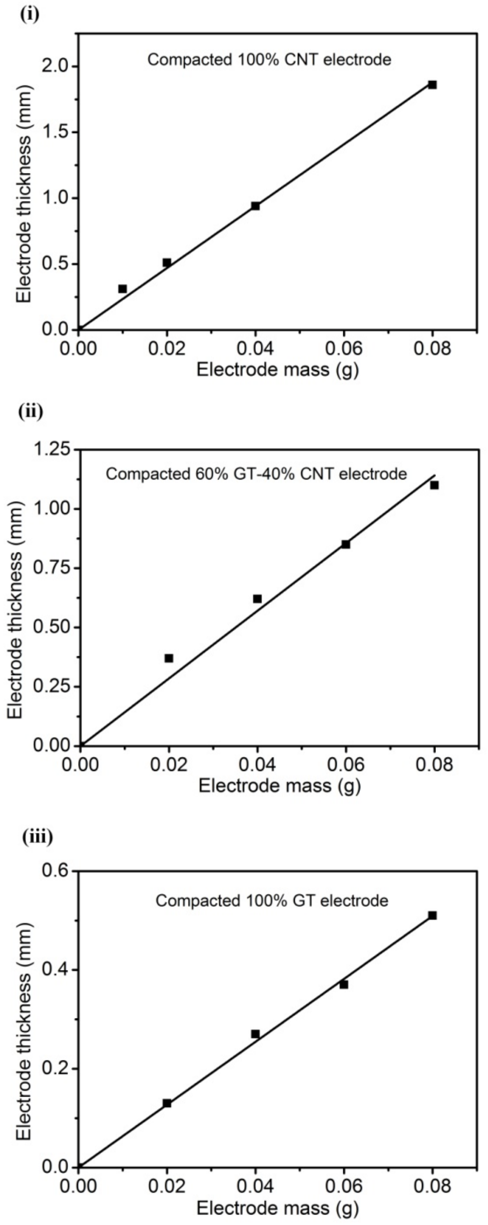

Figure 4.3. Dependence of electrode thickness on electrode mass of (i) the compacted 100% CNT electrode, (ii) the compacted 60% GT-40% CNT electrode, and (iii) compacted 100% GT electrode, under the pressure of 0.5 tonnes.

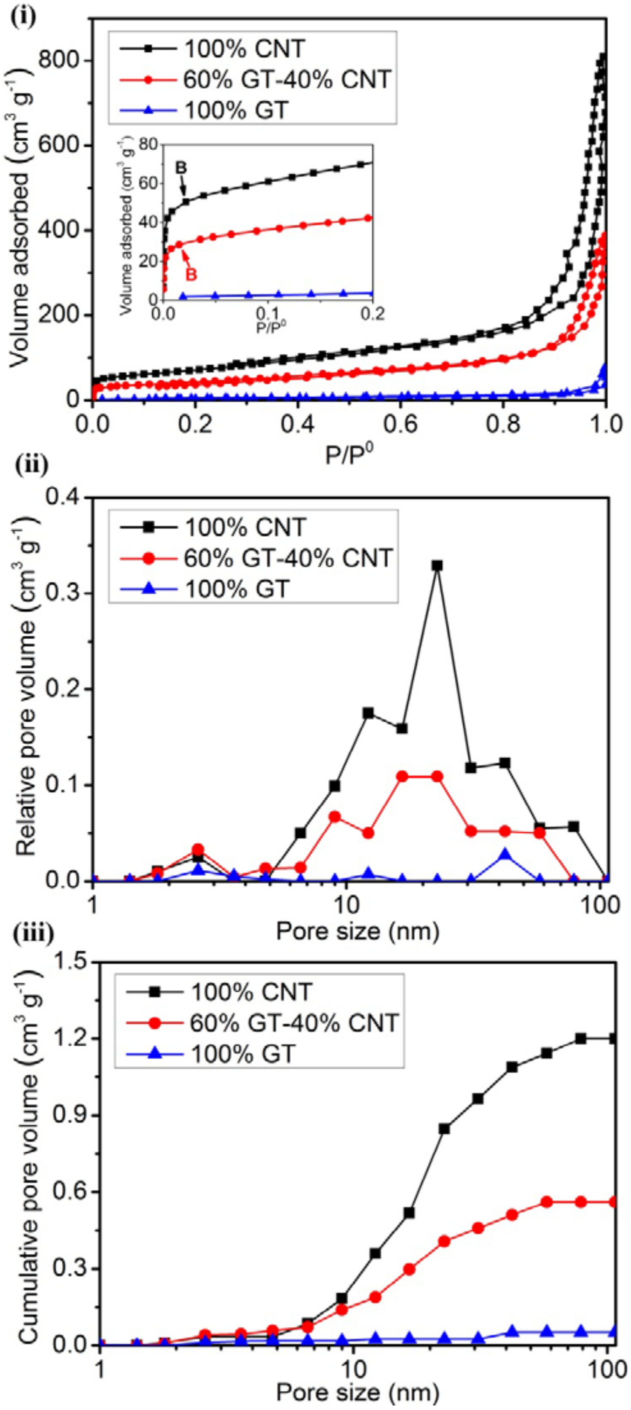

Figure 4.4. N_2 adsorption-desorption isotherms (i) and the corresponding pore size distribution curves (ii & iii) of the compacted 100% GT, 60% GT-40% CNT, 100% CNT electrodes. The inset in (i) shows the zoomed-in isotherms (P/P^0: 0-0.2), giving a clear Point B.

Figure 4.4(i) shows the typical N_2 adsorption-desorption isotherms of the compacted 100% GT, 60% GT-40% CNT and 100% CNT electrodes. The three physisorption isotherms exhibit the characteristic feature of the Type IV curve, that is, the hysteresis loop related to capillary condensation occurring in mesopores (pore diameter: 2-50 nm).[368] Both of the isotherms of the compacted 100% CNT and 60% GT-40% CNT electrodes have Point B (see the inset of Figure 4.4(i)), at which the almost linear middle section of the isotherm starts.[368] The Point B is indicative of a transition from monolayer coverage to multilayer adsorption.[385] The absence of this point on the adsorption-desorption isotherm of the compacted 100% GT electrode shows the weak absorbate-absorbent interaction compared with the absorbate-absorbate interactions and a considerable overlap between monolayer and multilayer adsorption.[368,385] Using the BET method, the specific surface areas of the compacted 100% GT, 60% GT-40% CNT and 100% CNT electrodes are calculated to be 15.6 $m^2 \cdot g^{-1}$, 154 $m^2 \cdot g^{-1}$ and 256 $m^2 \cdot g^{-1}$, respectively. Electrodes with larger specific surface area are possible to immobilize more catalysts and thus provide more reaction sites per unit geometric electrode area.

Furthermore, an effective fuel cell electrode also requires a relatively high porosity, necessary for the good mass transport of substrates and products, and moreover, in terms of enzymatic fuel cells, pore sizes should be large enough to be permeable to and accommodate macromolecular enzymes. Figures 4.4(ii)-(iii) show the relative and cumulative pore size distributions of three 3D CPC electrodes based on the BJH model. The pore volumes/porosity of the compacted 100% GT, 60% GT-40% CNT and 100% CNT electrodes are 0.052 $cm^3 \cdot g^{-1}$/6.2%, 0.56 $cm^3 \cdot g^{-1}$/29% and 1.2 $cm^3 \cdot g^{-1}$/39%, respectively. The volumes of those pores having sizes larger than 10 nm are 0.034 $cm^3 \cdot g^{-1}$, 0.42 $cm^3 \cdot g^{-1}$ and 1.0 $cm^3 \cdot g^{-1}$, making up 65%, 75% and 85% of the total pore volumes of the compacted 100% GT, 60% GT-40% CNT and 100% CNT electrodes, respectively. As mentioned in Sections 2.3 and 3.2, the pore size of 10 nm is the minimum requirement for the permeation and immobilization of enzymes in the internal porous channels of the electrodes. Therefore, most of the pores of the CPC electrodes have met this requirement. As both the specific surface area and the pore volumes of the compacted 60% GT-40% CNT and 100% CNT electrodes are one order of magnitude larger than that of the compacted 100% GT electrode, the enzyme loadings of the compacted 60% GT-40% CNT and 100% CNT electrodes are much larger than the enzyme loading of the compacted 100% GT electrode, and meanwhile, the mass transports of dissolved gases and products in the compacted 60% GT-40% CNT and 100% CNT electrodes are also much more efficient than in the compacted 100% GT electrode, which should result in significantly higher current densities in the compacted 60% GT-40% CNT and 100% CNT electrodes (as confirmed in Section 4.4). Mesopore volumes of the compacted 100% GT, 60% GT-40% CNT and 100% CNT electrodes constitute 100%, 90% and 90% of the total pore volume, consistent with the Type IV isotherms (given by mesoporous absorbents); for the remaining 10% of pore volume in both the compacted 60% GT-40% CNT and 100% CNT electrodes, 9% has diameters greater than 50 nm (*i.e.* macropores) and 1% less than 2 nm (*i.e.* micropores).

4.4 Effect of porous structures on catalytic activity

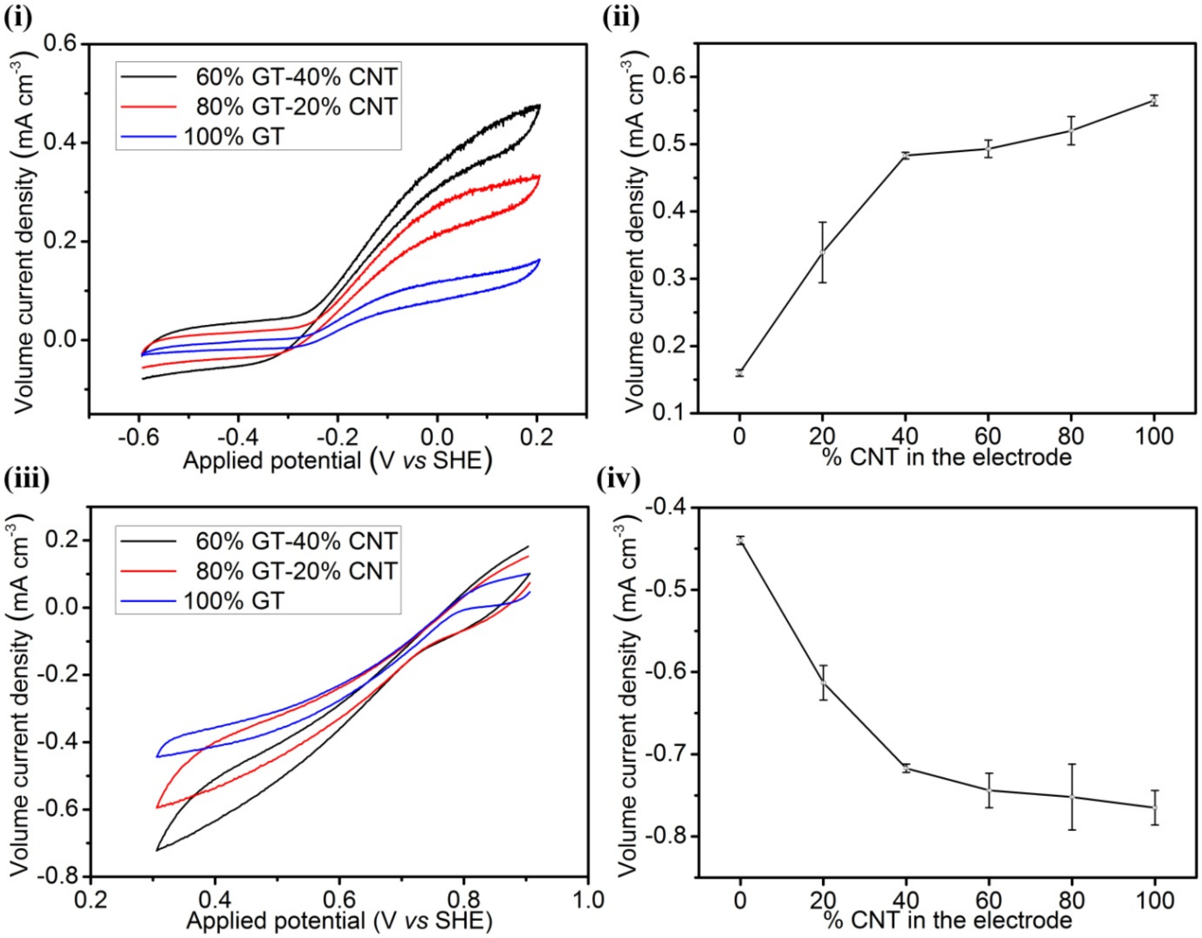

Figure 4.5. CVs of the Hyd-1-modified 3D CPC anodes (i) in 100% H_2 and the BOD-modified 3D CPC cathodes (iii) in 100% air with the three ratios between GT and CNT (*i.e.* 60% GT-40% CNT, 80% GT-20% CNT, and 100% GT). The average volume current densities measured at +0.206 V *vs.* SHE for the anodes (ii) and at +0.306 V *vs.* SHE for the cathodes (iv) as a function of the mass ratios of CNT to GT (*i.e.* 100% CNT, 80% CNT-20% GT, 60% CNT-40% GT, 40% CNT-60% GT, 20% CNT-80% GT, and 100% GT). Other conditions: operated in the membrane-less, quiescent unit cell of the test bed, 0.1 M sodium phosphate buffer, pH 6.0, 20°C, scan rate: 1 mV s^{-1}.

Since adjusting the ratios between GT and CNT can vary the specific surface area, pore volume, and pore size distribution of the 3D CPC electrodes, how do the varied surface structures of the electrodes affect the current density? Figure 4.5(i) shows CVs of the Hyd-1-modified 3D CPC anodes with the three ratios between GT and CNT (*i.e.* 100% GT, 80% GT-20% CNT, 60% GT-40% CNT) under membrane-less, quiescent conditions and Figure 4.5(ii) shows the average anodic current densities as a function of the mass ratios of CNT to GT. Measured at +0.206 V *vs.* SHE, the volume current densities at the compacted 100% GT, 80% GT-20% CNT, 60% GT-40% CNT, 40% GT-60% CNT, 20% GT-80% CNT, and 100% CNT anodes are 0.160 ± 0.005 mA·cm^{-3}, 0.339 ± 0.045 mA·cm^{-3}, 0.483 ± 0.005 mA·cm^{-3}, 0.493 ± 0.013 mA·cm^{-3}, 0.520 ± 0.021 mA·cm^{-3}, and 0.565 ± 0.008 mA·cm^{-3}, respectively. The catalytic activity at the anodes increases with the mass ratio of CNT to GT while such increase becomes small over 60% GT-40% CNT.

Moreover, Figure 4.5(iii) shows CVs of the BOD-modified 3D CPC cathodes comprised of 100% GT, 80% GT-20% CNT, 60% GT-40% CNT and Figure 4.5(iv) shows the average cathodic current densities *vs.* the CNT/GT ratio. The volume current densities (at +0.206 V *vs.* SHE) at the compacted 100% GT, 80% GT-20% CNT, 60% GT-40% CNT, 40% GT-60% CNT, 20% GT-80% CNT, and 100% CNT cathodes are –0.440 ± 0.005 mA·cm^{-3}, –0.613 ± 0.021 mA·cm^{-3}, –0.717 ± 0.005 mA·cm^{-3}, –0.744± 0.021 mA·cm^{-3}, –0.752 ± 0.040 mA·cm^{-3}, and –0.765 ± 0.021 mA·cm^{-3}, respectively. As expected, the cathodic current densities increase as the increase in the ratios of CNT to GT, the same trend as the anodic currents. This is because the 3D CPC electrodes with larger specific surface areas and pore volumes can accommodate and immobilize more macromolecular enzymes (*i.e.* higher density of catalytic reaction sites) and allow for more efficient mass transport, thus leading to faster electrochemical reaction rates and higher current densities. Though the compacted 100% CNT electrode has the best performance, the compacted 60% GT-40% CNT electrode is selected as the working electrode for this test bed in view of the balance between effectiveness and efficiency (cost control). Specifically, the unit price of multi-walled carbon nanotube is at least two orders of magnitude higher than that of graphite according to Sigma-Aldrich, thus the cost of the compacted 100% CNT electrode is about 2.5 times as high as the cost of the compacted 60% GT-40% CNT electrode, while the catalytic activities increase by only 17% for the anodes and 7% for the cathodes from the compacted 60% GT-40% CNT electrode to the compacted 100% CNT electrode. The view of cost control is important for practical applications of fuel cells.

4.5 Optimizing enzyme quantities

As the catalysts in enzymatic fuel cells, the population density of enzymes immobilized at electrodes has considerable influence over the catalytic activity: the more enzymes, the more reaction sites, thus the higher current outputs. Owing to the limitations of mass transport and electrode carrying capacity, however, the current would not continue increasing but reach a saturation plateau when the enzyme quantities increase to a certain level. Further increasing the enzyme quantities beyond this level would bring about not only the enzyme waste but also ‘enzyme jams’ in the internal porous channels of electrodes, thereby possible to hinder the mass transport of substrates and products to/from enzymes. Therefore, optimizing enzyme quantities is important for the performance of catalytic reactions occurring at the enzyme-modified electrodes. As Hyd-1 and BOD are applied to the 3D CPC electrodes by letting the enzymes naturally permeate into the electrodes and immobilize at the rough surface of the electrodes by physical adsorption (see Section 4.10), the enzyme concentrations directly control the enzyme quantities accommodated and immobilized at the electrodes.

Figure 4.6(i) shows CVs of the compacted 60% GT-40% CNT anodes modified by Hyd-1 with various concentrations and Figure 4.6(ii) shows the average anodic current densities as a function of the Hyd-1 concentrations. The volume current densities (measured at +0.206 V *vs.* SHE) are 0.234 ± 0.015 $\text{mA}\cdot\text{cm}^{-3}$, 0.349 ± 0.024 $\text{mA}\cdot\text{cm}^{-3}$, 0.424 ± 0.027 $\text{mA}\cdot\text{cm}^{-3}$, 0.483 ± 0.005 $\text{mA}\cdot\text{cm}^{-3}$, and 0.480 ± 0.019 $\text{mA}\cdot\text{cm}^{-3}$ when the Hyd-1 concentrations are 0.5 $\text{mg}\cdot\text{ml}^{-1}$, 1 $\text{mg}\cdot\text{ml}^{-1}$, 2 $\text{mg}\cdot\text{ml}^{-1}$, 4 $\text{mg}\cdot\text{ml}^{-1}$, and 6 $\text{mg}\cdot\text{ml}^{-1}$, respectively. The anodic current density reaches a constant plateau at 4 $\text{mg}\cdot\text{ml}^{-1}$ of Hyd-1, showing that the enzymatic carrying capacity of the compacted 60% GT-40% CNT electrodes approaches the saturation at such concentration. Thus 4 $\text{mg}\cdot\text{ml}^{-1}$ is selected as the working concentrations of Hyd-1. Moreover, Figures 4.6(iii) shows CVs of the compacted 60% GT-40% CNT cathodes modified by the various concentrations of BOD and Figure 4.6(iv) shows the average cathodic current densities versus the BOD concentrations. The cathodic current densities (measured at +0.306 V *vs.* SHE) are –0.632 ± 0.005 $\text{mA}\cdot\text{cm}^{-3}$, –0.693 ± 0.011 $\text{mA}\cdot\text{cm}^{-3}$, –0.717 ± 0.005 $\text{mA}\cdot\text{cm}^{-3}$, and –0.731 ± 0.008 $\text{mA}\cdot\text{cm}^{-3}$ when the BOD concentrations are 1.5 $\text{mg}\cdot\text{ml}^{-1}$, 3 $\text{mg}\cdot\text{ml}^{-1}$, 6 $\text{mg}\cdot\text{ml}^{-1}$ and 12 mg·ml^{-1}, respectively. The cathodic current densities increase with the concentrations of BOD until the constant value beyond 6 mg·ml^{-1}, showing that the enzyme accommodation capacity approaches saturation at this concentration. Likewise, 6 mg·ml^{-1} is selected as the working concentration of BOD.

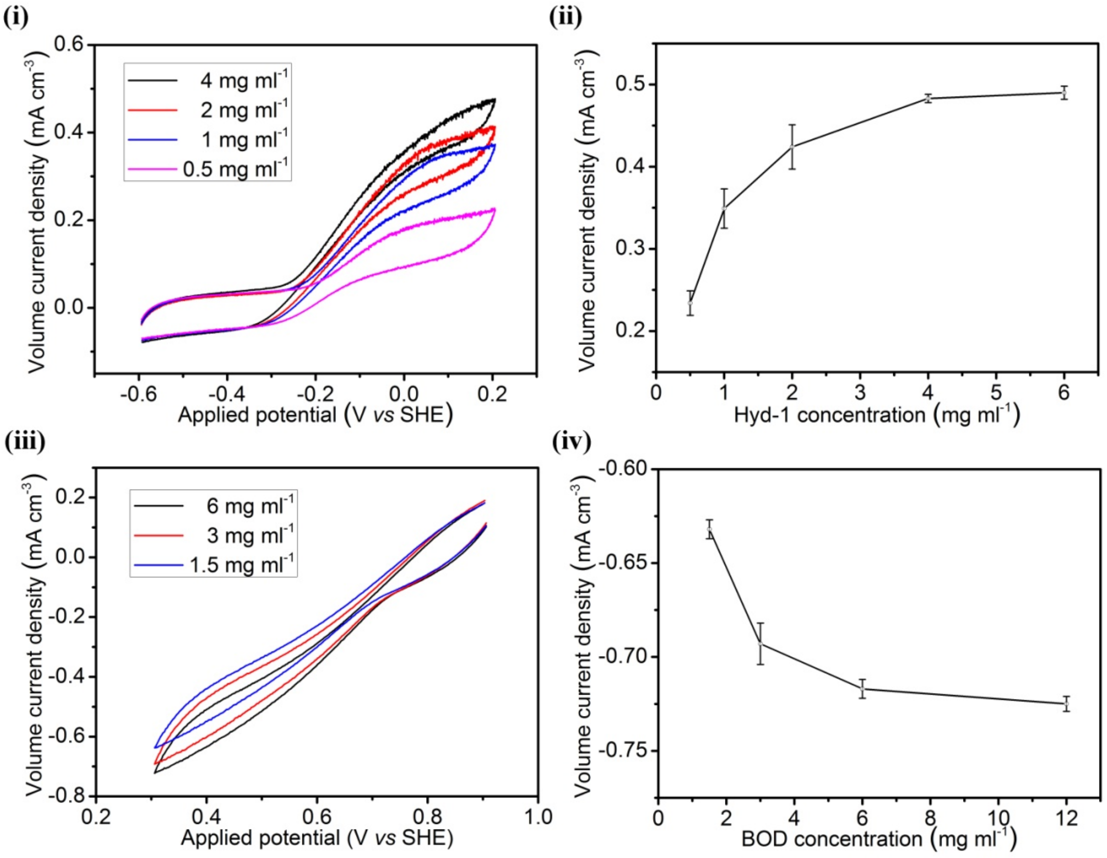

Figure 4.6. CVs of the compacted 60% GT-40% CNT electrodes modified by the various concentrations of Hyd-1 in 100% H$_2$ (i) and BOD in 100% air (iii). The average volume current densities measured at +0.206 V *vs.* SHE for the anodes (ii) and at +0.306 V *vs.* SHE for the cathodes (iv) as a function of the corresponding enzyme concentrations. Other conditions: operated in the membrane-less, quiescent unit cell of the test bed, 0.1 M sodium phosphate buffer, pH 6.0, 20°C, scan rate: 1 mV s^{-1}.

4.6 Parallel connections

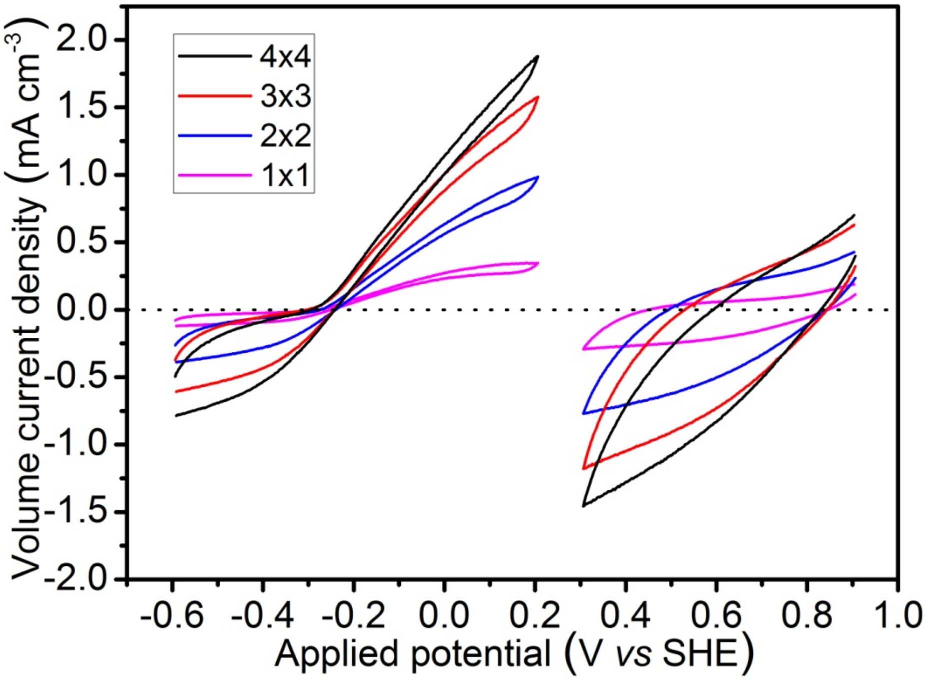

Figure 4.7. CVs of the Hyd-1-modified compacted 60% GT-40% CNT anodes and the BOD-modified 60% GT-40% CNT cathodes in the unit cell (1x1) and the parallel stacks (2x2, 3x3 and 4x4) under membrane-less, quiescent conditions in a 78% H_2-22% air mixture at 20°C. Other conditions: 0.1 M sodium phosphate buffer, pH 6.0, scan rate: 1 mV s^{-1}.

The unit cells in the test bed can be connected in parallel to increase the current outputs. Figure 4.7 shows CVs of the Hyd-1-modified compacted 60% GT-40% CNT anodes and the BOD-modified 60% GT-40% CNT cathodes in the unit cell (1x1) and the parallel stacks (2x2, 3x3 and 4x4) under membrane-less, quiescent conditions in a 78% H_2-22% air

(~4.6% O_2) mixture at 20 °C. The catalytic current densities at both the anodes and the cathodes increase as more cells are connected in parallel. Furthermore, the cathode/anode area ratio in each unit cell is re-proportioned to be 5:1 to offset the large excess of H_2 over O_2, thus the cathodic and anodic current densities in both the unit cell and the parallel stacks are balanced to be of the same order of magnitude under the H_2-rich atmosphere. This is highly beneficial to the substantial increase in the power density otherwise limited by the low O_2 level.

Based on the Hyd-1-modified compacted 60% GT-40% CNT anodes and the BOD-modified compacted 60% GT-40% CNT cathodes, the volume power density curves of the unit cell and the parallel stacks are shown in Figure 4.8. The OCVs of the 1x1, 2x2, 3x3 and 4x4 cells are 1.041 V, 1.041 V, 1.045 V and 1.048 V, respectively. The volume power densities of the 1x1, 2x2, 3x3 and 4x4 cells attain maxima of 0.16 ± 0.01 $mW \cdot cm^{-3}$, 0.48 ± 0.01 $mW \cdot cm^{-3}$, 0.79 ± 0.02 $mW \cdot cm^{-3}$, and 1.10 ± 0.02 $mW \cdot cm^{-3}$, respectively. The OCVs of the parallel stacks 2x2, 3x3 and 4x4 are almost the same as that of the unit cell 1x1, while the maximum power density of the 2x2 cell is 3 times as high as that of the 1x1 cell and the maximum power densities of the 3x3 and 4x4 cells are nearly 5 and 7 times as high as the maximum power density of the unit cell, respectively, showing that the maximum volume power densities of the parallel stacks are the summation of those of their constituent unit cells. The changes in the OCVs and volume power densities of the parallel stacks are consistent with the characteristics of parallel circuits.[371]

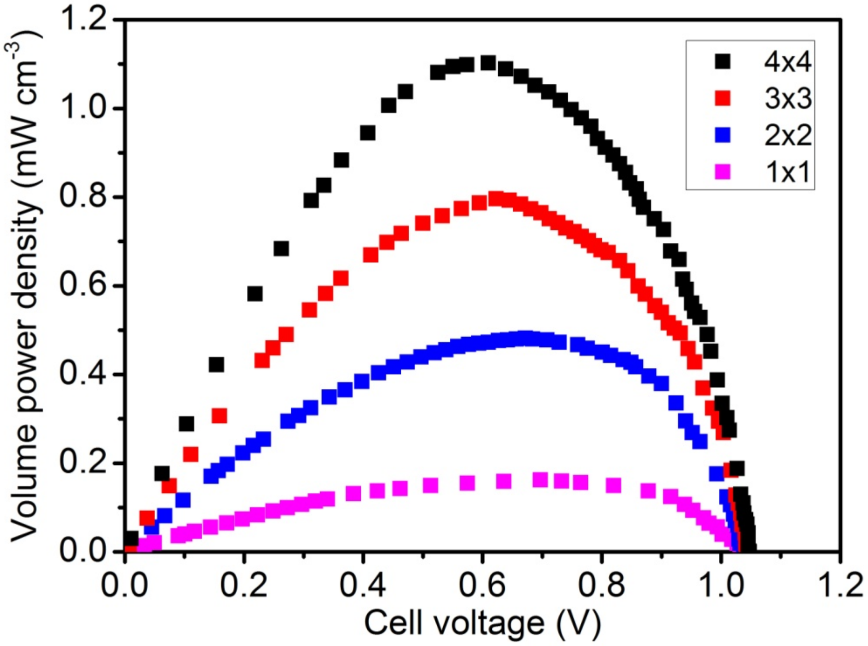

Figure 4.8. Volume power density curves of the unit cell (1x1) and the parallel stacks (2x2, 3x3, 4x4). All the curves were recorded in the test bed using the compacted 60% GT-40% CNT electrodes under a 78% H_2-22% air atmosphere at 20°C. Other conditions: 0.1 M sodium phosphate buffer, pH 6.0.

4.7 Series connection

In the test bed, the two parallel stacks 4x4 can be connected in series to double the cell voltage. Figure 4.9 shows the dependence of volume power density on the cell voltage of this series stack and its component in the 78% H_2-22% air mixture at 20 °C, using the compacted 60% GT-40% CNT electrodes. The OCV of the series stack are 2.090 V, twice as large as the OCV of a single 4x4 cell (*i.e.* 1.048 V). The maximum volume power density of the series stack is 2.09 ± 0.03 mW·cm^{-3} (at the cell voltage of 1.22 V), almost twice as high as the maximum volume power density of a 4x4 cell (*i.e.* 1.10 ± 0.02 mW·cm^{-3}), showing minimized ohmic fuel cell losses of the series stack.

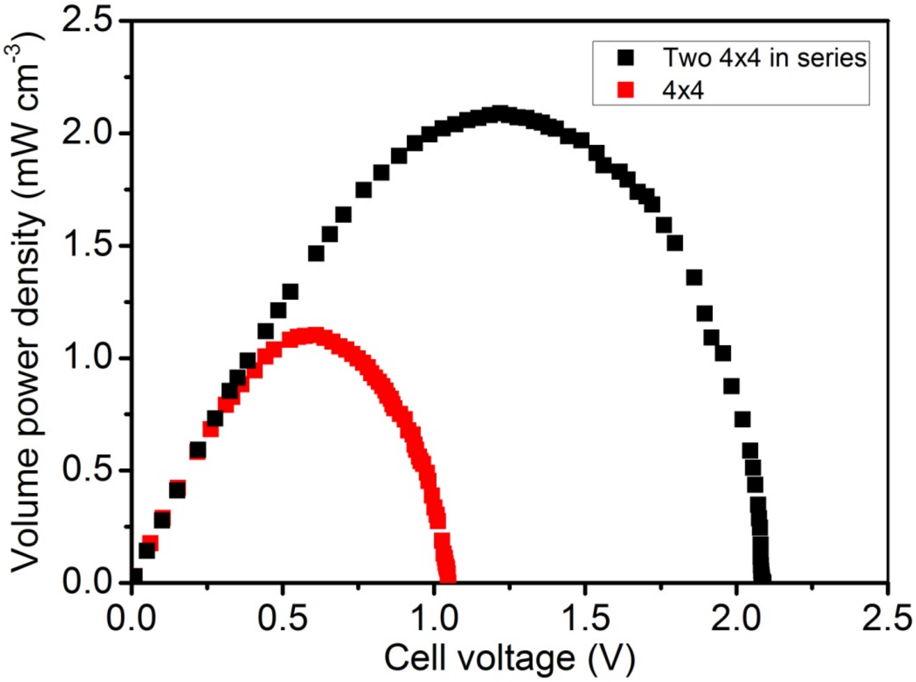

Figure 4.9. Volume power density curves of a single 4x4 cell and the series stack in which two 4x4 cells are connected in series. All the curves were recorded in the test bed using the compacted 60% GT-40% CNT electrodes under a 78% H_2-22% air atmosphere at 20°C. Other conditions: 0.1 M sodium phosphate buffer, pH 6.0.

4.8 Practical applications

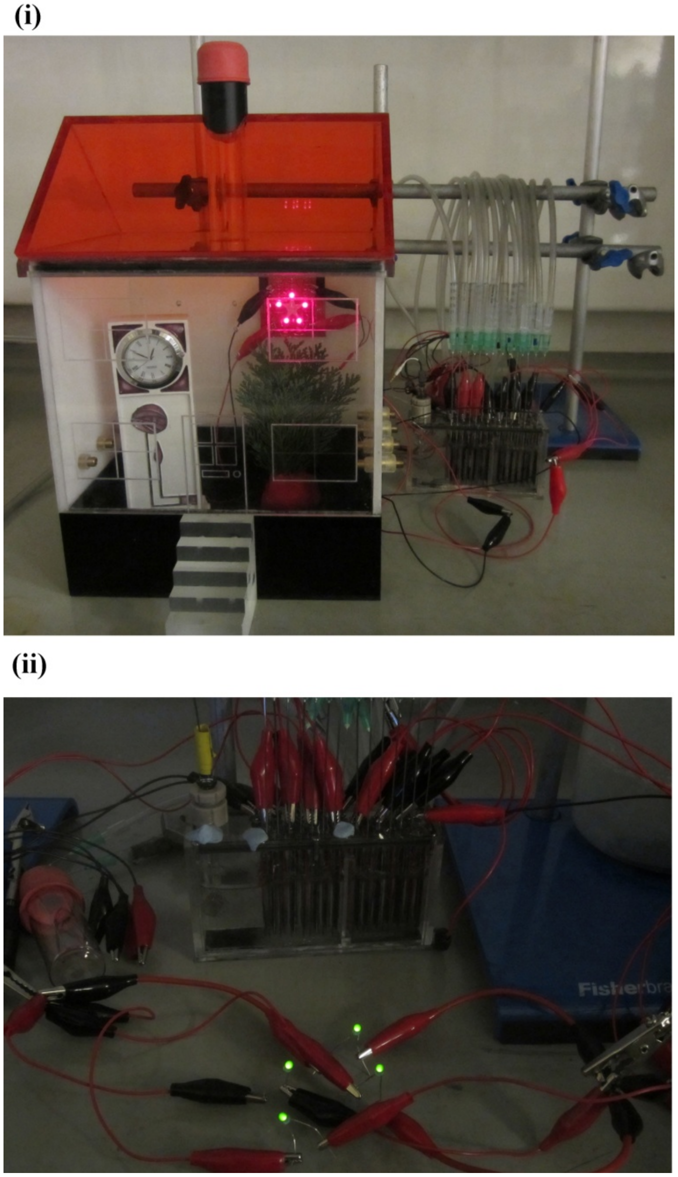

Figure 4.10. Photographs of the working test bed powering (i) five red LEDs and a clock (the LEDs and clock are connected in parallel to the test bed) and (ii) four green LEDs (which are also connected in parallel to the test bed). Working conditions: the test bed with the parallel and series connections, in which the two parallel stacks (4x4) cells are connected in series; the compacted 60% GT-40% CNT electrodes, a 78% H_2-22% air mixture at 20°C, 0.1 M sodium phosphate buffer at pH 6.0.

With the elevated voltage and current, the demonstration experiments have been conducted to show that the test bed, in which the two 4x4 cells are connected in series, are capable of powering electronics from a non-explosive 78% H_2-22% air mixture at 20 °C. Figure 4.10(i) shows that five red light-emitting diodes (LED) and a clock are powered by the fuel cell test bed, a demonstration of electricity that originates from the buried active sites of enzymes and is transmitted by long-range electron hopping. This test bed can even power four green LEDs, which require higher voltage, as shown in Figure 4.10(ii). To test the sustainability of the test bed, LEDs were switched on and off while the clock kept being connected to the test bed. The test bed could work normally without interruption, showing that it can withstand the sudden change of current and voltage.

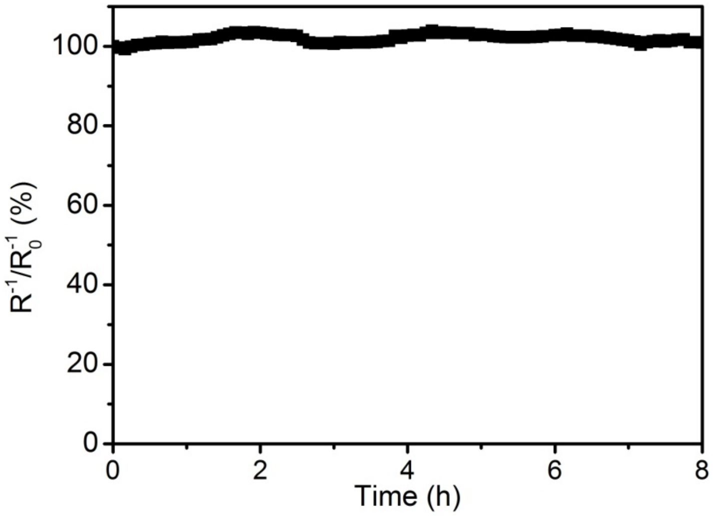

Figure 4.11. Dependence of stability of reciprocal of resistance of the LDR (%) with time (h = hours) for a red LED powered by the test bed (two 4x4 cells in series) using the compacted 60% GT-40% CNT electrodes under a 78% H_2-22% air atmosphere at 20°C. Other conditions: 0.1 M sodium phosphate buffer, pH 6.0.

Furthermore, a photoresistor or light dependent resistor (LDR) is used as a probe to monitor the change in light intensity of a red LED, reflecting the working stability of the fuel cell test bed. Because resistance in the LDR decreases with the increase in light intensity, the reciprocal of resistance can be used to reflect the light-emitting intensity.[386] Figure 4.11 shows the dependence of stability of the reciprocal of resistance (light intensity) on time. The light intensity of the LED powered by the test bed does not decay after continuously working for 8 hours, demonstrating the stably-working test bed.

4.9 Discussion

The fuel cell test bed has demonstrated low-loss interconnects between its components and efficient stack configuration. To achieve these, the test-bed design should meet the following requirements: *(1)* Minimize ohmic fuel cell losses. As mentioned in Section 1.1, the ohmic losses are caused by ionic and electronic resistance and can be minimized by making the travel distance of ions and electrons as short as possible (also meeting the miniaturization of fuel cell setup) and using high-conductivity, non-toxic, and inexpensive materials. One feasible way around this aim is to use stainless-steel plates, both sides of which can carry the 3D CPC electrodes (the anodic and cathodic plates are alternatively arranged), and to stack those plates in rows with a narrow gap, as presented in this chapter. *(2)* Make each unit cell identical. The large difference in fuel cell performance between the component unit cells can adversely influence the power output of a stack, especially important for the series stack, in which the stack current depends on the component with the lowest current. Although it is almost impossible to keep the performance of each unit cell exactly the same, making it close to each other is feasible. One method introduced here is integrating the electrode stacks into a single compartment, in which the electrolyte solution (for parallel connections) and the gas concentrations (for both parallel and series connections) are the same for those stacks. *(3)* Enhance mass transport under the quiescent condition. Here 'quiescent' means that neither rotating nor stirring is applied in the test bed because the power requirement for the rotating or stirring far exceeds the power produced by an enzymatic fuel cell. Without rotating or stirring, however, the current will be severely restricted by the poor mass transport of substrates and products to/from enzymes. One way of alleviating this problem without additional power consumption is to set gas inlets down at the bottom of the test bed. The effervescence can agitate the electrolyte solution and the solution containing bubbles of gaseous substrates (*i.e.* the H_2-air mixture) laps against the enzyme-modified electrodes, thereby enhancing the mass transport. Though the mass transport limitation still exists, the 'bubbling' is a contributing factor in the relatively high current/power densities in this test bed.

Adjusting the ratios between GT and CNT can vary the specific surface area, pore volume, and pore size distribution of the 3D CPC electrodes. The effect of varied surface structures of the electrodes on the current/power density originates from the difference in enzyme loading and mass transport of substrates and products in the internal porous channels of the electrodes. The 3D CPC electrodes, together with the 3D CMC electrodes described in Chapter 3, have demonstrated that electrodes with higher specific surface area, larger pore volume, and availability of >10 nm pore sizes allow for higher density of catalytic reaction sites and more efficient mass transport, thereby leading to higher current/power densities.

4.10 Methods

Materials: Graphite and multi-walled carbon nanotube were purchased from Sigma-Aldrich and used without further purification. Hyd-1 from *Escherichia coli* was isolated and purified as described previously.[254] Bilirubin oxidase from *Myrothecium verrucaria* was purchased from Amano Enzyme Inc and further purified by hydrophobic interaction chromatography with a HiTrap Phenyl HP hydrophobic column (GE Healthcare). Sodium dihydrogen orthophosphate and disodium hydrogen orthophosphate were purchased from Fisher Scientific and used to prepare the sodium phosphate buffer solution. The PGE electrode bases were made of pyrolytic graphite blocks (Momentive Performance Materials Ltd). Conductive silver paint (Agar Scientific) was used to glue the 3D CPC electrodes to the plates of the test bed. All aqueous solutions were prepared using deionized water from a Milli-Q water system (18 MΩ·cm).

Construction of the test bed: The fuel cell test bed consists of one compartment made of polycarbonate with a partial divider also made of polycarbonate. A reference electrode Ag/AgCl and a counter electrode Pt mesh are set at the left side. The main part of the test bed consists of 16 stainless-steel plates as the supporters for the 3D CPC electrodes and as current collectors (see Figure 4.2(i)). The 3D CPC electrodes are glued to both sides of the plates by conductive silver paint. The exposed metal area not covered by the 3D CPC electrodes on the plates is painted to insulate against the electrolyte solution. The top edges of the plates are bent and can be fixed to the ceiling of the test bed by screws and nuts, which also function as the current connectors. This also allows for the convenient dismantling of the plates. The anodic and cathodic plates are fixed in an alternative way. The gas inlet is positioned in the centre of each unit cell for the good gas distribution. There are 14 gas inlets corresponding to the 14 unit cells.

Fabrication of the 3D CPC electrodes: A certain quantity of GT, CNT, or the mixtures of the two carbon allotropes was placed in a pellet die (Specac) and subjected to a pressure of 0.5 tonnes using a hydraulic press (Specac). As shown in Figure 4.3, different quantities of GT, CNT, or the mixtures are required for a certain thickness of the 3D CPC electrodes. For the typical thickness of 0.3 mm, (1) the compacted 100% GT electrode needs 47 mg of GT; (2) the compacted 60% GT-40% CNT electrode needs 12 mg of GT and 8 mg of CNT; (3) the compacted 100% CNT electrode needs 11 mg of CNT. The CPC discs were then cut to size for the required geometric area and attached to the test-bed plates using conductive silver paint. After the paint was dry, 30 µL of Hyd-1 (or Hyd-2) (4 $mg \cdot mL^{-1}$) was applied to the 3D CPC anode and a multiple of 30 µL (in proportion to the area ratio of cathode to anode) of BOD (6 $mg \cdot mL^{-1}$) was applied to the 3D CPC cathode. The enzyme-modified CPC electrodes were subsequently placed in a cold room (4 °C) for 1 h to allow sufficient permeation of enzymes into the electrodes before starting the electrochemical characterization and fuel cell tests. For the 2D carbon electrode, 5 μL of the enzyme solution (Hyd-1/Hyd-2: 4 mg·mL^{-1}, BOD: 6 mg·mL^{-1}) was pipetted onto the surface of the PGE electrode, which was subsequently placed in a cold room (4 °C) for 1 h and rinsed with deionized water before the electrochemical experiments.

Instrumentation: Electrochemical measurements were performed on an Ivium potentiostat (CompactStat, Ivium Technologies) in the fuel cell test bed. All potentials were adjusted to the standard hydrogen electrode (SHE) using the relationship $E_{\text{SHE}} = E_{\text{Ag/AgCl}} + 0.206$ V at 25 °C. Power measurements were obtained by varying the applied load and recording the potential in each case (Keithley 195A digital voltmeter). The ratios of H_2 to air were controlled by two mass flow controllers (Sierra Instruments). A Sorptomatic 1990 instrucment (CE Instruments) was used to acquire N_2 adsorption-desorption isotherms at 77 K. The BET surface area was calculated from the linear part of the BET plot. The pore size distribution plots were obtained by using the BJH model. The light intensity of the red LED is monitored by a cadmium sulphide (CdS) light dependent resistor connected to a digital multimeter.

Chapter 5

3D electrodes increase the apparent O_2-tolerance degrees of both O_2-tolerant and O_2-sensitive [NiFe]-hydrogenases

Abstract

The degree of O_2 tolerance of [NiFe]-hydrogenases has a significant effect on the fuel cell performance.[210,212,348] This chapter shows that, in addition to the substantial increase in the power density and lifetime of an enzyme-based membrane-less H_2 fuel cell, the 3D CPC electrodes are also able to largely increase the degrees of apparent O_2 tolerance of [NiFe]-hydrogenases, including both O_2-tolerant and O_2-sensitive [NiFe]-hydrogenases exemplified by Hyd-1 and Hyd-2, respectively. The O_2-tolerance degrees of the O_2-tolerant Hyd-1 and O_2-sensitive Hyd-2, both of which are immobilized at the 2D and 3D electrodes with varied porous structures, are studied by the cyclic voltammetry and chronoamperometry techniques. The electrochemical characterizations exhibit that the 3D CPC electrodes can indeed substantially increase the apparent O_2-tolerance degrees for both Hyd-1 and Hyd-2, allowing the inherently O_2-tolerant enzyme (Hyd-1) to own a much higher O_2-tolerance degree and making the inherently O_2-sensitive enzyme (Hyd-2) be able to oxidize H_2 in the presence of O_2. Such interesting results originate from the porous structures of the 3D CPC electrodes. The effusion occurs inside the porous structures of the 3D electrodes. Because the rate of effusion of H_2 is four times as high as that of O_2, the H_2 and O_2 undergo a separation in the porous channel according to the Graham's law of effusion. In other words, the porous structure of 3D CPC electrode acts as a sieve to sift H_2 from O_2, so the enzymes permeated to the depths of the electrode would not be exposed to O_2 and thus retain their active states. Based on the compacted 100% CNT electrode, the O_2-sensitive Hyd-2 is able to work as the anodic catalyst in a membrane-less fuel cell in a non-explosive H_2-rich H_2-air mixture.

5.1 Introduction

In Chapters 3-4, one focus is on how to increase the low cathodic currents that severely limit the power density of an enzyme-based membrane-less H_2 fuel cell. On the other hand, the O_2-tolerance degree of the anodic catalyst – [NiFe]-hydrogenase also has considerable influence over the fuel cell performance. [210,212,348] All hydrogenases that have been characterized to date are inactivated or permanently damaged by O_2 or/and high potential.[210,213] Even for the inherently O_2-tolerant [NiFe]-hydrogenases, such as Hyd-1, the activity of H_2 oxidation would still suffer from almost complete inactivation when the enzymes immobilized at the PGE electrode were exposed to O_2 at high potentials.[348] The inactivation of hydrogenases by O_2, regardless of reversible or irreversible inhibition, can severely impair the anodic current magnitude and the stability of the fuel cell. Therefore, as far as the fuel cell performance is concerned, it is very important to improve the O_2 tolerance of the [NiFe]-hydrogenases.

Let us recall how an inherently O_2-tolerant [NiFe]-hydrogenase retains its H_2-oxidation activity in the presence of O_2. As described in Section 2.1.3, the O_2 tolerance of the [NiFe]-hydrogenase originates from *(i)* the 'restricted' access of O_2 to the active site via gas channels, *(ii)* the availability of additional electron sources close to the active site, and *(iii)* the fast recovery to the active states. The *(iii)* is usually the result of the *(ii)* because the fast delivery of sufficient electrons to the active site can ensure the formation of the Ni-B state which can recover rapidly. Therefore, the first two aspects play key roles in the inherent O_2-tolerance ability of [NiFe]-hydrogenases. Using the molecular biology techniques, the improved O_2-tolerance degrees of hydrogenase mutants with more electron sources closed to the active site or optimized sizes of gas channels could be obtained.

Are there any feasible non-biological methods for the improvement in the O_2-tolerance degrees of hydrogenases? Hydrogenases are immobilized onto the internal porous channels of the 3D electrodes, which can be considered as ‘big’ gas channels compared to ‘small’ gas channels within the protein matrix. So it is possible to use this ‘big’ gas channels to control the access of O_2 to the enzymes. This chapter demonstrates that the 3D CPC electrodes can do this job! The porous structures of the 3D CPC electrodes allow the effusion of H_2 and O_2 to occur in the ‘big’ gas channel. The O_2 is ‘screened’ out due to the much slower effusion rates than H_2 so that quite a few of hydrogenases permeated and immobilized deeply in the 3D electrode are not exposed to O_2 but H_2, thus the integrated or apparent O_2-tolerance degrees of the hydrogenases are increased. Based on the compacted 100% CNT electrode, a membrane-less fuel cell using the O_2-sensitive Hyd-2 as an anodic catalyst can produce power under the H_2-rich H_2-air mixture.

5.2 Increasing the apparent O_2-tolerance degree of Hyd-1

It can be observed that the CV shapes of Hyd-1 at the 3D CPC electrodes (in Chapters 3-4) are slightly different from the CV shapes of the same enzyme at the 2D PGE electrodes (in Refs. 254 and 265). The difference is obvious when Hyd-1 undergoes O_2 inhibition at high

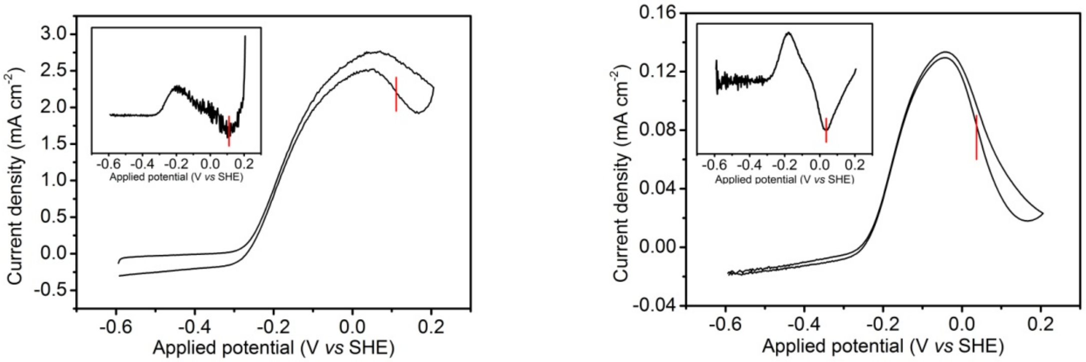

(i) Hyd-1 at the 3D electrode in the 89% H_2-11% air mixture

(ii) Hyd-1 at the 2D electrode in the 89% H_2-11% air mixture

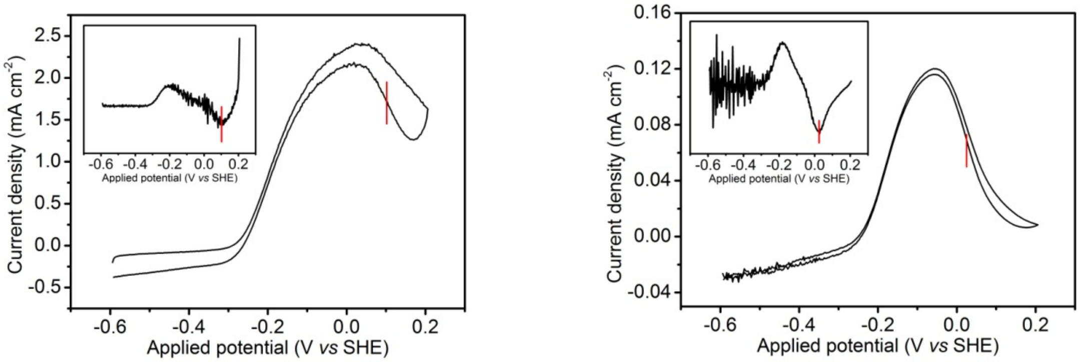

(iii) Hyd-1 at the 3D electrode in the 78% H_2-22% air mixture

(iv) Hyd-1 at the 2D electrode in the 78% H_2-22% air mixture

Figure 5.1. CVs of Hyd-1 at the compacted 60% GT-40% CNT electrode in the 89% H_2-11% air mixture (i), the PGE electrode in the 89% H_2-11% air mixture (ii), the compacted 60% GT-40% CNT electrode in the 78% H_2-22% air mixture (iii), and the PGE electrode in the 78% H_2-22% air mixture (iv). The current density is normalized to geometric base area of the corresponding electrodes (PGE: 0.03 cm^2, CPC: 0.2 cm^2). The insets show the first derivative plots (d*i*/d*E* *vs.* *E*) of the reductive sweep (towards more negative potentials) of the corresponding voltammograms. E_{switch} is determined by the minimum of the derivative,[212] marked by a vertical red bar. Other conditions: 0.1 M sodium phosphate buffer at pH 6.0 and 20°C, scan rate: 1 mV s^{-1}.

potentials: Hyd-1 at the 2D electrodes suffers from more severe aerobic inactivation than the 3D electrodes in the presence of air, as shown in Figure 5.1. What information can we get from such difference? Here, the term E_{switch} is used to characterize the CVs of Hyd-1 at the 3D and 2D electrodes. The E_{switch} value is a potential determined by the minimum of the first derivative (di/dE) of the reductive direction (towards more negative potentials) of the corresponding CV scan,[212] as shown in the insets of Figure 5.1. E_{switch} is dependent on the experimental conditions, such as pH, temperature, and scan rate.[212] Though the origin of E_{switch} is still unknown, it is a useful index of the O_2-tolerance degree for [NiFe]-hydrogenases (relating to the ease of reactivating the oxidized, inactive ready state Ni-B): a higher value of E_{switch} shows a less thermodynamically-favoured state of Ni-B and a higher degree of O_2 tolerance under the same experimental conditions.[254,265] From Figure 5.1, the E_{switch} value of Hyd-1 at the 3D compacted 60% GT-40% CNT electrode is +0.111 V *vs*. SHE and E_{switch} of Hyd-1 at the 2D PGE electrode is +0.037 V *vs*. SHE under the 89% H_2-11% air mixture, and the E_{switch} values of Hyd-1 at the 3D and 2D electrodes are +0.102 V and +0.025 V *vs*. SHE under the 78% H_2-22% air mixture, respectively. The same enzyme Hyd-1 under the same conditions exhibits a higher E_{switch} value at the 3D electrode, showing a higher degree of O_2 tolerance at the 3D electrode than the 2D electrode. Therefore, in addition to the substantial increase in the power density and the significant improvement in the stability of fuel cells, the 3D porous structures of electrodes can also bring about the third advantage: weakening the negative influence of hydrogenase aerobic inactivation during prolonged air exposure and increasing the degree of apparent O_2 tolerance of hydrogenases. The improvement in the apparent O_2 tolerance of Hyd-1 is important for the sustainability of enzyme-based hydrogen fuel cells for the reason that even for the O_2-tolerant Hyd-1, the activity of H_2 oxidation at the 2D electrode would still suffer from almost complete inactivation when the enzymes are exposed to air at high potentials (see Figure 5.1).

The effect of prolonged O_2 exposure on the H_2 oxidation activity of Hyd-1 at the 3D and 2D electrodes is conducted to understand how the active sites of Hyd-1 at the two electrodes react to the O_2 attack on a longer scale of time. Figure 5.2 shows the chronoamperograms of Hyd-1 at the 3D compacted 60% GT-40% CNT electrode and the 2D PGE electrode recorded at a high potential +0.206 V *vs.* SHE (more positive than E_{switch}) with the periodic rise and fall of H_2 levels in H_2-air mixtures. Because lower potentials have a stronger external driving force to provide enough electrons rapidly for the active site when it is attacked by O_2 and to reactivate Ni-B, to study the level of *spontaneous* recovery from aerobic inactivation of Hyd-1 at the 3D and 2D electrodes, the high potential +0.206 V which is not effective in driving this recovery is applied (a harsh condition for Hyd-1). The H_2 concentrations in the non-explosive H_2-air mixtures vary every 1200 s (20 min), and the sequence is 100% → 89% → 100% → 78% → 100%. From Figure 5.2, it can be found: *(1)* for Hyd-1 at the 3D electrode, 58% and 42% of currents are retained in 89% H_2-11% air and 78% H_2-22% air mixtures, respectively, whereas only 7.5% and 3.5% of currents are retained for Hyd-1 at the 2D electrode, showing that Hyd-1 at the 3D electrode can maintain much higher activity of H_2 oxidation in the presence of air than the 2D electrode; *(2)* after the H_2 concentration returns to 100%, the current at the 3D electrode recovers to the previous anaerobic level in 360 s and 400 s from the 89% H_2-11% air and 78% H_2-22% air mixtures, respectively, while the current at the 2D electrode cannot recover to the original level in 1200 s, showing that Hyd-1 at the 3D electrode

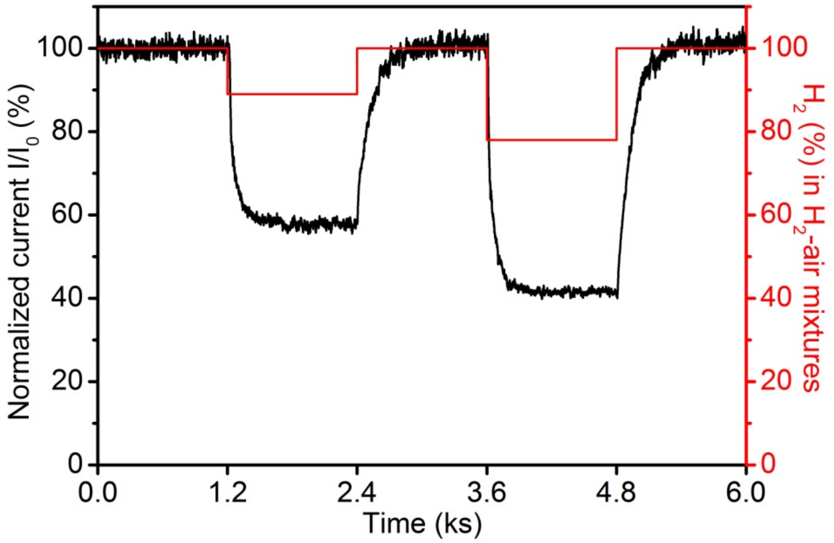

(i) Hyd-1 at the 3D compacted 60% GT-40% CNT electrode at +0.206 V *vs.* SHE

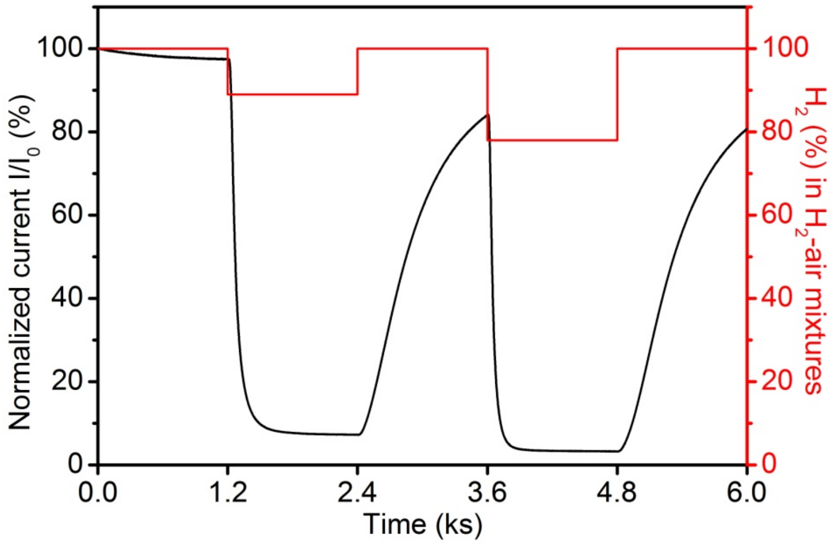

(ii) Hyd-1 at the 2D PGE electrode at +0.206 V *vs.* SHE

Figure 5.2. Chronoamperograms of Hyd-1 at the compacted 60% GT-40% CNT electrode (i) and the PGE electrode (ii) recorded at +0.206 V *vs.* SHE (ks = kilosecond). The H_2-air mixtures with different ratios are periodically (every 1200 s) applied, as indicated in red (100% H_2 → 89% H_2-11% air → 100% H_2 → 78% H_2-22% air → 100% H_2). Other conditions: 0.1 M sodium phosphate buffer at pH 6.0 and 20°C.

sustains a higher level of fast, spontaneous recovery of aerobically generated states than the 2D electrode; *(3)* 100% of the current is retained at the 3D electrode over an extended period of time (6000 s), while Hyd-1 at the 2D electrode loses 3% of its activity in 1200 s alone, showing that the enzyme is more sustainable at the 3D electrode than the 2D electrode. Therefore, it can be concluded that 3D porous structures can increase the apparent O_2-tolerant degree of Hyd-1 and partly ‘protect’ its H_2-oxidation activity from prolonged exposure to air, thus leading to the significant improvement in the sustainability and stability of fuel cells.

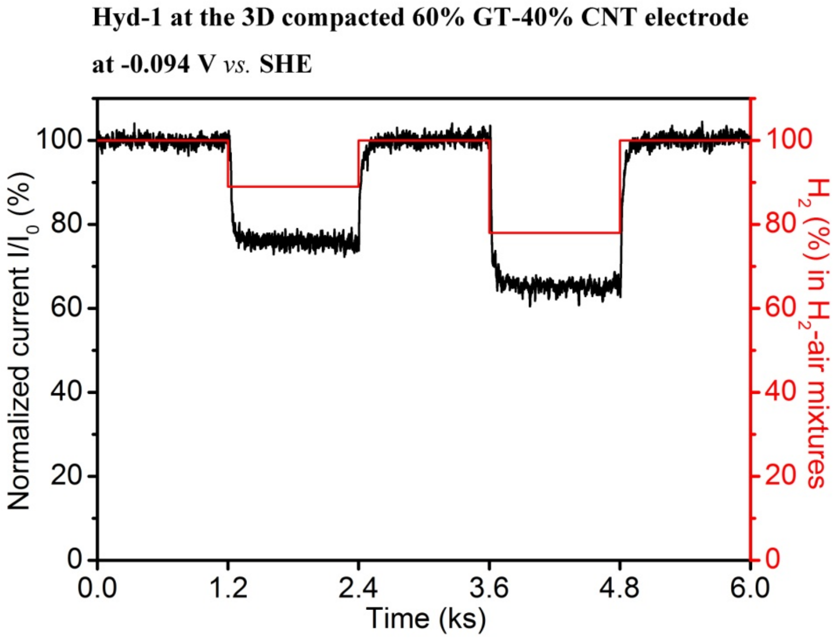

Figure 5.3. Chronoamperograms of Hyd-1 at the compacted 60% GT-40% CNT electrode recorded at –0.094 V *vs.* SHE (ks = kilosecond). The H_2-air mixtures with different ratios are periodically (every 1200 s) applied, as indicated in red (100% H_2 → 89% H_2-11% air → 100% H_2 → 78% H_2-22% air → 100% H_2). Other conditions: 0.1 M sodium phosphate buffer at pH 6.0 and 20°C.

Figure 5.3 shows the chronoamperogram of Hyd-1 at the 3D compacted 60% GT-40% CNT recorded at a relatively low potential -0.094 V *vs.* SHE (more negative than E_{switch}). As expected, Hyd-1 at a lower potential exhibits the improved O_2 tolerance: (1) 76% of the initial current is retained in the 89% H_2-11% air mixture and 65% of the current is retained in the 78% H_2-11% air mixture, sustaining higher activity of H_2 oxidation than at a higher potential; (2) upon returning to 100% H_2, the currents recover to the initial levels in 85 s from the 89% H_2-11% air and in 90 s from the 78% H_2-11% air, showing a much faster spontaneous recovery of the H_2-oxidation activity of Hyd-1 exposed to air at the lower potential than at the higher.

5.3 Effect of porous structures on the apparent O_2 tolerance of Hyd-1

In Chapter 4, it has been discussed that the pore volume and pore size distribution of the compacted 100% GT electrode are different from those of the compacted 60% GT-40% CNT electrode. To study the effect of porous structures of the 3D electrodes on the H_2-oxidation activity of Hyd-1 in the presence of O_2, the chronoamperogram of Hyd-1 at the 3D compacted 100% GT electrode recorded at +0.206 V *vs.* SHE is conducted, as shown in Figure 5.4 (the chronoamperogram of Hyd-1 at the 3D compacted 60% GT-40% CNT electrode at the same potential, as indicated in blue, is overlaid for the comparison of the two porous structures). It can be found that 47% of the initial current in the 89% H_2-11%

air mixture and 32% of the current in the 78% H_2-22% air mixtures are retained for Hyd-1 at the compacted 100% GT electrode, compared to 58% and 42% of the currents retained at the compacted 60% GT-40% CNT electrode, respectively. The degree of apparent O_2 tolerance of Hyd-1 at the compacted 100% GT electrode is lower than at the compacted 60% GT-40% CNT electrode, consistent with the order of their pore volumes. Moreover, after the H_2 concentration returns to 100%, the current at the compacted 100% GT electrode recovers to its initial level in 620 s from the 89% H_2-11% air atmosphere and in 730 s from

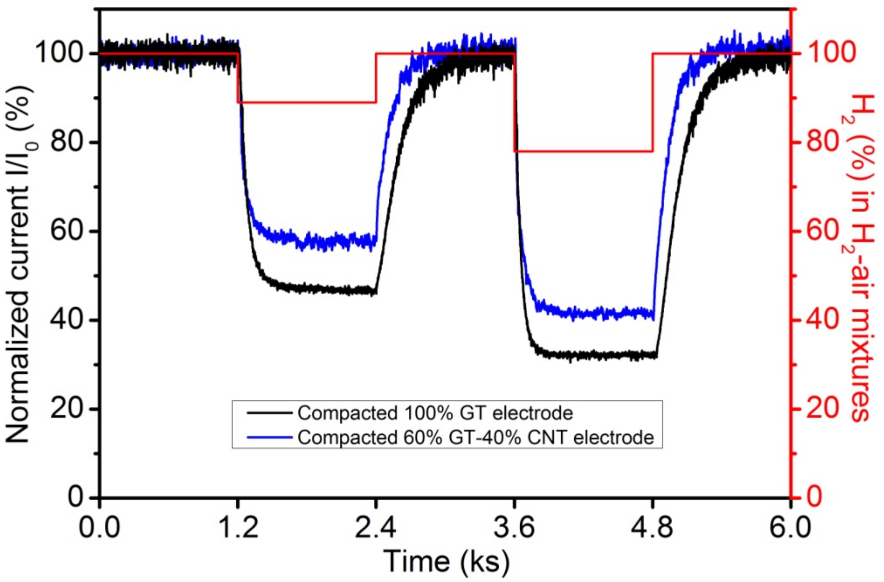

Figure 5.4. Chronoamperograms of Hyd-1 at the compacted 100% GT electrode (black) and the compacted 60% GT-40% CNT electrode (blue) recorded at +0.206 V *vs.* SHE (ks = kilosecond). The H_2-air mixtures with different ratios are periodically (every 1200 s) applied, as indicated in red (100% H_2 → 89% H_2-11% air → 100% H_2 → 78% H_2-22% air → 100% H_2). Other conditions: 0.1 M sodium phosphate buffer at pH 6.0 and 20°C.

78% H_2-22% air, while the recovery time at the compacted 60% GT-40% CNT electrode is 360 s and 400 s, respectively. Therefore, the porous structures with large pore volumes can allow Hyd-1 to maintain the high activity of H_2 oxidation under the aerobic conditions and enhance the apparent O_2 tolerance of Hyd-1.

5.4 Effect of the porous structure on the O_2-reduction activity of BOD

To understand how the porous structure influences O_2-reduction activity of BOD, the chronoamperograms (recorded at +0.606 V *vs.* SHE) of BOD at the compacted 60% GT-40% CNT and compacted 100% GT electrodes are conducted in the periodical fall of H_2 levels (or the rise of O_2 levels) in the H_2-air mixtures, as shown in Figure 5.5. The sequence of varied H_2 concentrations is 100% → 89% → 78% → 50% → 0%. The chronoamperogram curves of BOD at the two 3D electrodes are very similar. For the compacted 60% GT-40% CNT electrode, the currents increase to 14%, 25% and 54% of the steady-state level in 100% air when the air percentages in the H_2-air mixtures are 11%, 22% and 50%, respectively, and for the compacted 100% GT electrode, the currents increase to 16%, 28% and 57% of the steady-state level in 100% air when the air proportions are 11%, 22% and 50%, respectively, showing that BOD at the compacted 100% GT electrode maintains almost the same percentage of the currents as the compacted 60% GT-40% CNT electrode in the same level of air.

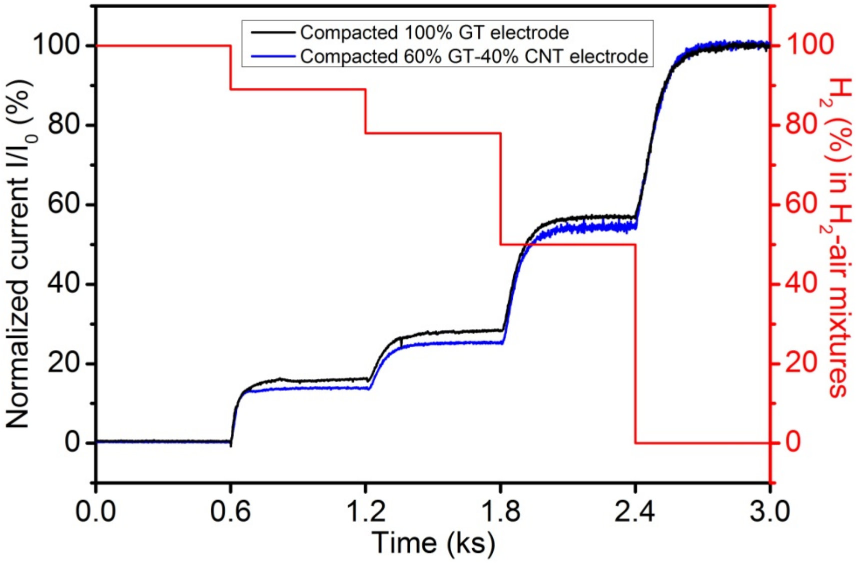

Figure 5.5. Chronoamperograms of BOD at the compacted 100% GT electrode (black) and the compacted 60% GT-40% CNT electrode (blue) recorded at +0.606 V *vs.* SHE (ks = kilosecond). The H_2-air mixtures with different ratios are periodically (every 600 s) applied, as indicated in red (100% H_2 → 89% H_2-11% air → 78% H_2-22% air → 50% H_2-50% air → 100% air). Other conditions: 0.1 M sodium phosphate buffer at pH 6.0 and 20°C.

Figure 5.6 shows the chronoamperograms of BOD at the 3D compacted 100% GT electrode recorded at +0.606 V *vs.* SHE with the periodic rise and fall of air levels in H_2-air mixtures. The air proportions in the H_2-air mixtures vary every 600 s in the order of 0% → 11% → 22% → 50% → 100% → 50% → 22% → 11% → 0%. At the same proportions of air in the H_2-air mixtures, the levels of currents in the two opposite directions of varying the H_2/air ratios are the same, showing the good reversibility of O_2-reduction activity of BOD.

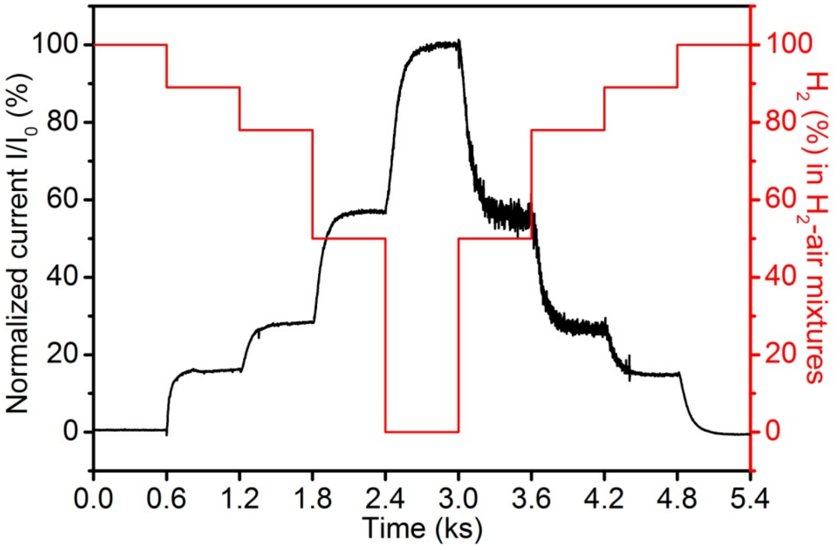

Figure 5.6. Chronoamperograms of BOD at the compacted 100% GT electrode recorded at +0.606 V *vs.* SHE (ks = kilosecond). The H_2-air mixtures with different ratios are periodically (every 600 s) applied, as indicated in red (100% H_2 → 89% H_2-11% air → 78% H_2-22% air → 50% H_2-50% air → 100% air → 50% H_2-50% air → 78% H_2-22% air → 89% H_2-11% air → 100% H_2). Other conditions: 0.1 M sodium phosphate buffer at pH 6.0 and 20°C.

5.5 Increasing the apparent O_2-tolerance degree of an O_2-sensitive hydrogenase

Since the 3D CPC electrodes can enhance O_2-tolerance degree of Hyd-1, consider an extreme case: can these electrodes also increase the degree of O_2 tolerance of O_2-sensitive enzymes and allow them to work under aerobic conditions? An O_2-sensitive enzyme – Hyd-2 is used to test this hypothesis. Figure 5.7(i) shows CVs of Hyd-2 at the 2D PGE

(i) Hyd-2 at the 2D PGE electrode

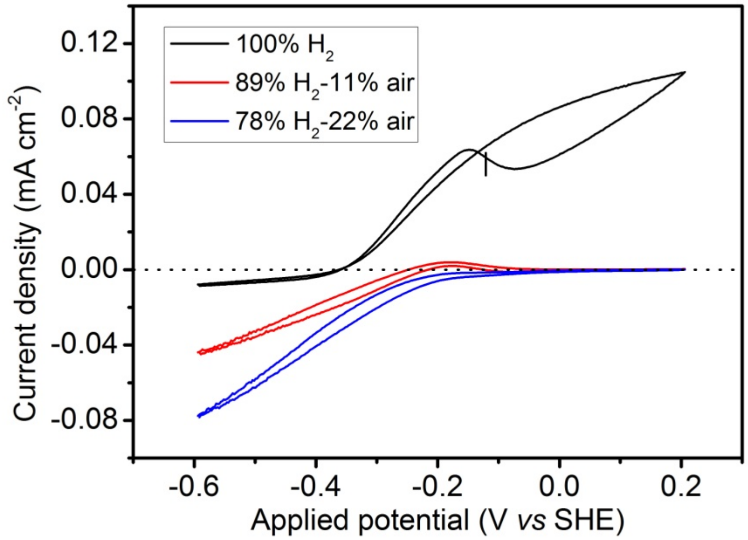

(ii) Hyd-2 at the 3D compacted 100% CNT electrode

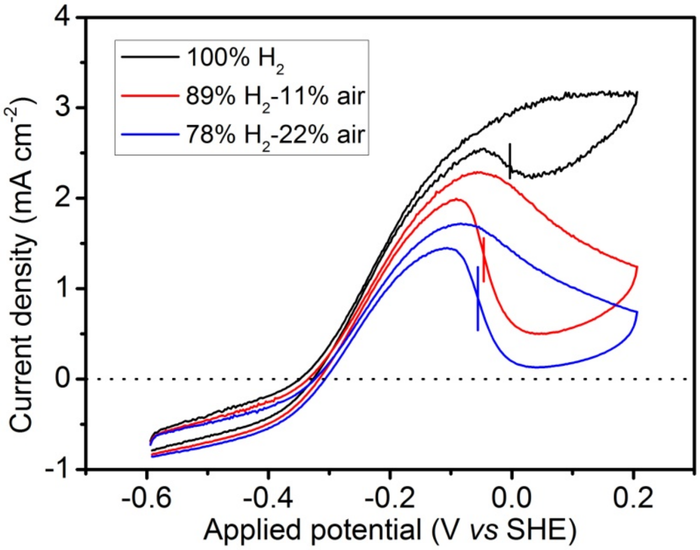

Figure 5.7. CVs of Hyd-2 at the PGE electrode (i) and the compacted 100% CNT electrode (ii) in the 100% H_2 (black), 89%H_2-11% air (red) and 78% H_2-22% air (blue) mixtures. The current density is normalized to geometric base area of the corresponding electrodes (PGE: 0.03 cm^2, CPC: 0.2 cm^2). The E_{switch} values are indicated by vertical bars. Other conditions: 0.1 M sodium phosphate buffer at pH 6.0 and 20°C, scan rate: 1 mV s^{-1}.

electrode in the 100% H_2, 89% H_2-11% air and 78% H_2-22% air mixtures. Compared to the anaerobic condition, Hyd-2 at the 2D electrode shows negligible H_2-oxidation activity and the onset potential of H_2 oxidation is shifted 112 mV more positive under the 89% H_2-11% air mixture, whereas it simply shows no H_2-oxidation activity under the 78% H_2-22% air mixture. Figure 5.7(ii) shows CVs of Hyd-2 at the 3D compacted 100% CNT electrode in the 100% H_2, 89% H_2-11% air and 78% H_2-22% air mixtures. Under the aerobic conditions, Hyd-2 at the 3D electrode can still maintain substantial H_2-oxidation activity and the onset for H_2 oxidation are shifted to more positive potentials by merely 13mV in 89% H_2-11% air and 23 mV in 78% H_2-22% air compared with the onset potential in 100% H_2.

Figure 5.8 shows the potential windows for H_2-oxidation activity of Hyd-2 at the 2D and 3D electrodes. The lower boundary of a potential window for activity is defined by the onset potential of H_2 oxidation and the upper boundary is by E_{switch}.[261] Under both anaerobic and aerobic conditions, Hyd-2 at the 3D electrode has a wider potential window for H_2-oxidation activity than the 2D electrode. Specifically, the potential window for H_2-oxidation activity of Hyd-2 at the 2D electrode narrows considerably to 106 mV in 89% H_2-11% air from 237 mV in 100% H_2 and disappears altogether in 78% H_2-22% air, whereas, for Hyd-2 at the 3D electrode, the potential window for H_2-oxidation activity is reduced from 343 mV under the anaerobic condition to 287 mV (89% H_2-11% air) and 267 mV (78% H_2-22% air). By comparison with the narrow or extinct potential window at the 2D electrode, the wide potential window for H_2-oxidation activity of Hyd-2 exposed to air shows that the 3D electrode can *thermodynamically* keep the O_2-sensitive enzyme active in H_2 oxidation under aerobic conditions. On the other hand, the current density of H_2 oxidation at the Hyd-2-modified 3D electrode sustains the scale of mA cm^{-2} in the presence of air, while that at the 2D electrode is as tiny as a few µA cm^{-2} in 89% H_2-11% air and becomes nought in 78% H_2-22% air, showing that the 3D electrode can *kinetically* permit Hyd-2 to work as an anodic catalyst in a membrane-less enzyme hydrogen fuel cell running on a non-explosive H_2-air mixture.

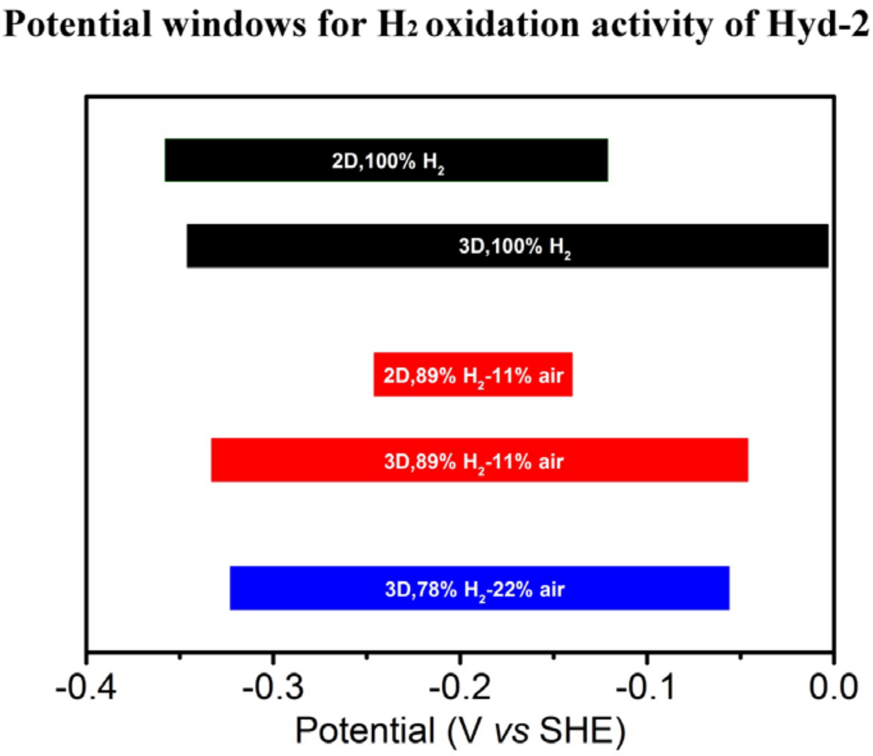

Figure 5.8. Potential windows for H_2-oxidation activity of Hyd-2 at different electrodes and H_2-air mixtures.

5.6 Effect of porous structures on the apparent O_2 tolerance of Hyd-2

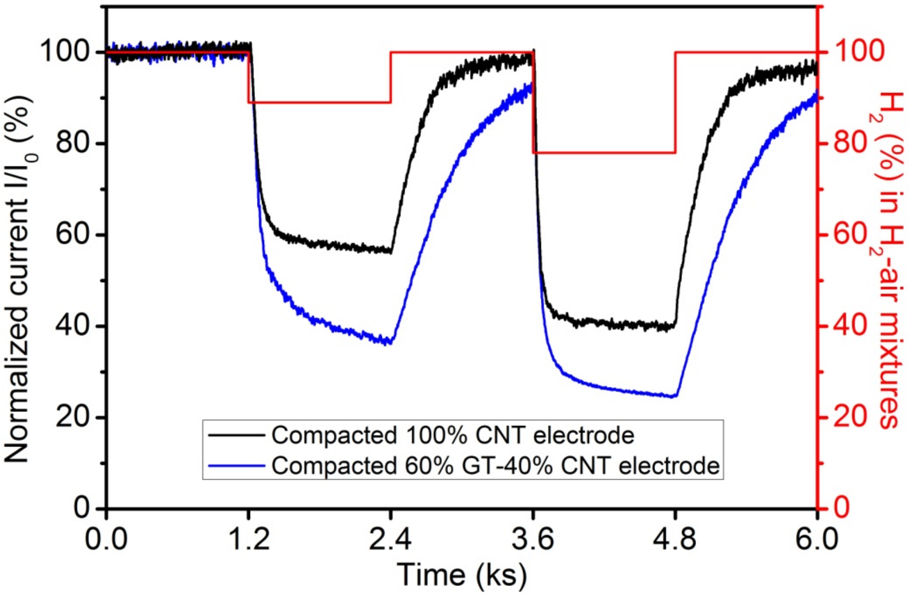

Figure 5.9. Chronoamperograms of Hyd-2 at the compacted 100% CNT (black) and 60% GT-40% CNT (blue) electrodes recorded at +0.006 V *vs.* SHE. The H_2-air mixtures with different ratios are periodically (every 1200 s) applied, as indicated in red (100% H_2 → 89% H_2-11% air → 100% H_2 → 78% H_2-22% air → 100% H_2). Other conditions: 0.1 M sodium phosphate buffer at pH 6.0 and 20°C.

Hyd-2 at different 3D CPC electrodes exhibits different levels of apparent O_2 tolerance. Figure 5.9 shows the chronoamperograms of Hyd-2 at the compacted 100% CNT and 60% GT-40% CNT electrodes recorded at +0.006 V *vs.* SHE (above their E_{switch} values, see Figure 5.8). Under the aerobic conditions, more currents are retained at the compacted 100% CNT electrode than the compacted 60% GT-40% CNT electrode, showing that Hyd-2 at the former can maintain higher H_2-oxidation activity than the latter in the presence of air. Moreover, Hyd-2 at the compacted 60% GT-40% CNT electrodes shows a ‘steep’ decrease in H_2 oxidation current in the presence of air, whereas Hyd-2 at the compacted 100% CNT electrode attains relatively steady currents (or slow decrease) under the aerobic conditions, showing that the H_2-oxidation activity of Hyd-2 at the compacted 100% CNT electrode achieves an improved balance between the rates of aerobic inactivation and re-activation. As the compacted 100% CNT electrode has the larger pore volume than the compacted 60% GT-40% CNT electrode, the levels of apparent O_2 tolerance of Hyd-2 at the two electrodes are consistent with their pore volumes. Upon returning to 100% H_2, the H_2-oxidation currents recover to 98% and 90% of the original values in 1200 s for Hyd-2 at the compacted 100% CNT and 60% GT-40% CNT electrodes, respectively, but neither of them return to the initial levels like Hyd-1 (see Figure 5.2(i)).

To understand whether part of Hyd-2 at the 3D CPC electrodes loses its ability of spontaneous recovery from O_2 inactivation at relatively high potentials, the chronoamperograms of Hyd-2 at the compacted 60% GT-40% CNT electrodes recorded at +0.006 V *vs.* SHE were conducted, as shown in Figure 5.10. The 78% H_2-22% air mixture was introduced after one-hour 100% H_2 exposure and lasted 18 hours. Hyd-2 shows a continual decrease in H_2-oxidation current in the presence of air (the spontaneous recovery cannot resist the aerobic inactivation), and the current can reach a much lower steady-state level and recover to about 60% of the initial value after returning to 100% H_2 for 5 hours. The control experiment without introducing O_2 during the chronoamperometry was conducted and shows that the current can retain 100% of the initial value after 24 hours (confirming again the good stability of catalytic currents based on the 3D CPC electrodes). Therefore, the H_2-oxidation activity of Hyd-2 will be impaired when exposed to air and the 3D CPC electrodes cannot prevent this process but 'postpone' it. The irreversible activity loss of Hyd-2 during exposure to O_2 is probably due to permanent damage of Fe-S clusters or the oxidation of sulphur atoms of cysteine residues close to the active site.[212,247]

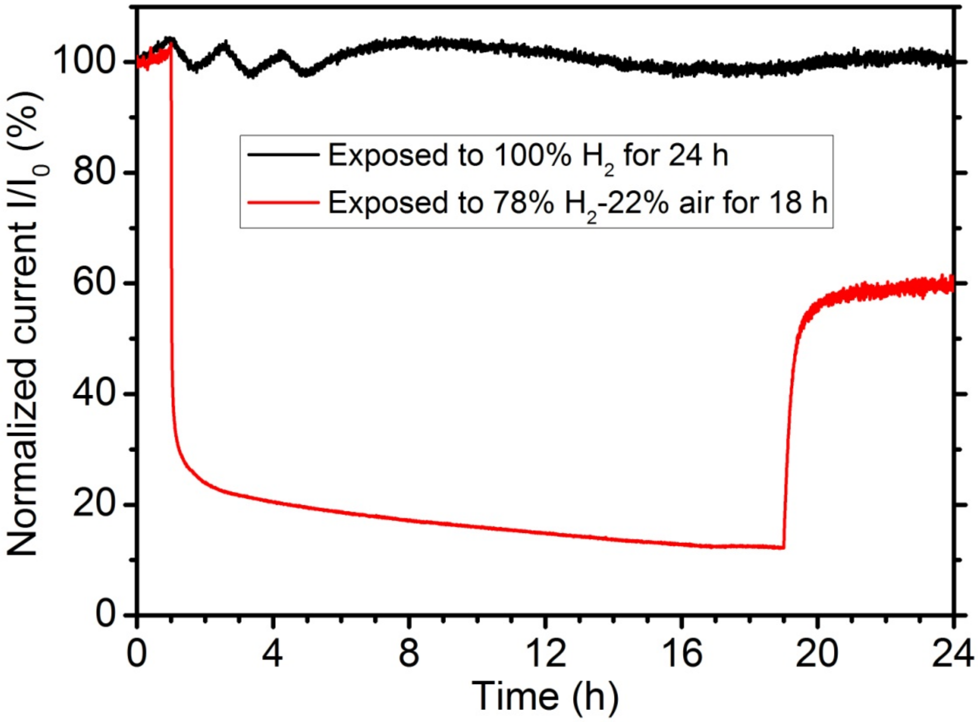

Figure 5.10. Chronoamperograms of Hyd-2 at the compacted 60% GT-40% CNT electrodes exposed to 100% H_2 for 24 h (black) and to 100% H_2 (1 h) → 78% H_2-22% air (18 h) → 100% H_2 (5 h) (red), recorded at +0.006 V *vs.* SHE. Other conditions: 0.1 M sodium phosphate buffer at pH 6.0 and 20°C.

5.7 Effect of electrode thickness on the apparent O_2 tolerance of Hyd-2

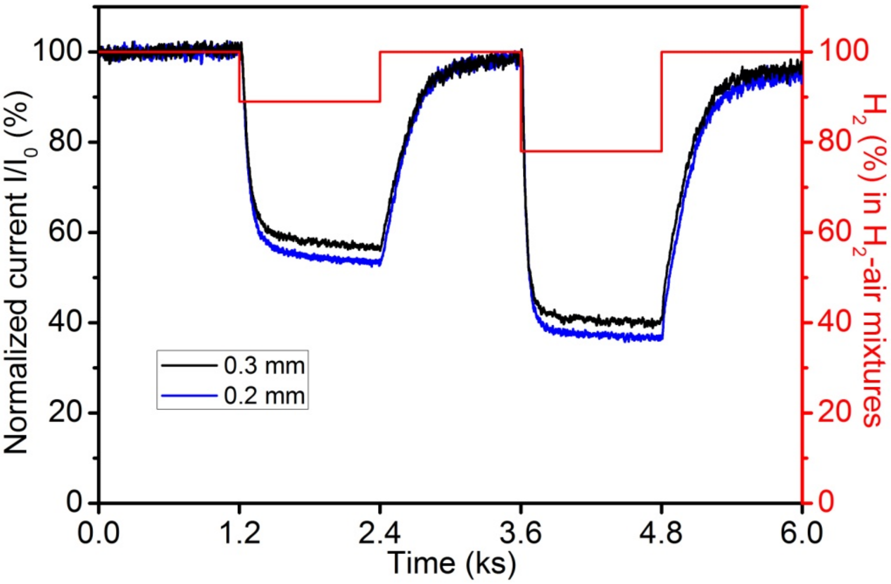

Figure 5.11. Chronoamperograms of Hyd-2 at the compacted 100% CNT having the thickness of 0.3 mm (black) and the thickness of 0.2 mm (blue) recorded at +0.006 V *vs.* SHE. The H_2-air mixtures with different ratios are periodically (every 1200 s) applied, as indicated in red (100% H_2 → 89% H_2-11% air → 100% H_2 → 78% H_2-22% air → 100% H_2). Other conditions: 0.1 M sodium phosphate buffer at pH 6.0 and 20°C.

As a characteristic of the 3D CPC electrodes, the thickness also plays a role in the apparent O_2-tolerance degree of Hyd-2. Figure 5.11 shows the chronoamperograms of Hyd-2 at the 0.2-mm and 0.3-mm compacted 100% CNT electrodes recorded at +0.006 V *vs.* SHE. Hyd-2 at the thicker electrode maintains the higher activity of H_2 oxidation under the aerobic conditions than the O_2-sensitive enzyme at the thinner electrode. Moreover, when the H_2 concentration returns to 100%, the spontaneous recovery of aerobically generated states at the 0.3-mm electrode is slightly faster than at the 0.2-mm electrode, and the H_2-oxidation current of Hyd-2 at the thinner electrode recovers to 95% of the original value in 1200 s compared to 97% at the thicker electrode, showing that the thicker electrode can better protect the catalytic activity of Hyd-2 in the presence of air. However, the 3D CPC electrodes with the thickness larger than 0.3 mm are prone to crumble away and become unstable, so the thickness is selected as 0.3 mm.

5.8 Mechanisms

Why can the 3D porous electrodes increase the apparent O_2 tolerance of Hyd-1 and Hyd-2? This is because effusion occurs inside the porous structure of the 3D electrodes. In the H_2-air mixtures, the main constituents are H_2, N_2 and O_2. The mean free paths (λ) for H_2, N_2 and O_2 at 293 K and 101325 Pa are calculated to be 100 nm, 64 nm and 70 nm, respectively, according to:[387]

$$\lambda = \frac{RT}{\sqrt{2}\pi d^2 LP} \tag{5.1}$$

where d is the collision diameter of a gas (H_2: 2.71 Å, N_2: 3.70 Å, O_2: 3.55 Å).[388] Furthermore, as shown in Figures 4.4(ii)-(iii), the volumes of the pores having diameters smaller than 70 nm make up >95%, 100%, and 100% of the total pore volumes of the compacted 100% CNT, 60% GT-40% CNT, and 100% GT electrodes, respectively (because N_2 is an inert gas, only the mean free paths for H_2 and O_2 are considered).

Effusion occurs when the pore size is smaller than the mean free path of a gas molecule, so the pore size distributions of the 3D CPC electrodes fulfil the effusion condition for H_2 and O_2.[387]

According to Graham's law of effusion, the rate of effusion of a gas is inversely proportional to the square root of its molecular weight.[387] Therefore, H_2 effuses 4 times as fast as O_2, which results in more H_2 molecules passing through effusion orifices per unit time. As a H_2-air mixture effuses through many pores, the proportion of H_2 will gradually increase. The 3D structure allows for effusion in depth and thus permits the H_2-air mixture to undergo such effusions enough frequencies to separate H_2 from O_2, thus Hyd-1 and Hyd-2 permeated to that depth and below are only exposed to H_2. In other words, the 3D porous structure 'sieves' the H_2-air mixture and sifts out H_2 from O_2 so that a fairly large number of hydrogenases immobilized in the internal electrode are not subject to aerobic inactivation, thereby leading to the substantial increase in the degree of apparent O_2 tolerance of Hyd-1 and Hyd-2 compared to the 2D electrode (see Figures 5.1, 5.2 and 5.7).

Moreover, the volumes of those pores having diameters between 10 nm and 70 nm are 0.959 $cm^3 \cdot g^{-1}$ and 0.422 $cm^3 \cdot g^{-1}$ for the compacted 100% CNT and 60% GT-40% CNT electrodes, respectively (see Figures 4.4(ii)-(iii)). Within the range of the pore sizes of 10 – 70 nm, the 3D CPC electrode with a larger pore volume has more effusion pores through which the H_2-air mixture can pass, thus resulting in a higher level of the separation of H_2 and O_2. Therefore, the compacted 100% CNT electrode can allow Hyd-2 to sustain the higher activity of H_2 oxidation in the presence of air and to maintain the higher degree of apparent O_2 tolerance than the compacted 60% GT-40% CNT electrodes (see Figure 5.9).

Similarly, increasing the thickness of the 3D porous electrode can increase effusion pores and thus increase apparent O_2 tolerance of hydrogenases. Hyd-2 at the compacted 100% CNT electrode with a thickness of 0.3 mm maintains the higher activity of H_2 oxidation under aerobic conditions than at the same type of electrode with a thickness of 0.2 mm (see Figure 5.11). On the other hand, the dimensions of the 3D CPC electrodes are after all limited, thus slow O_2 can finally reach the depths of the electrodes, leading to more and more Hyd-2 inactivation under prolonged exposure to air (see Figure 5.10). Since O_2 is ‘screened’ out, the porous structures of the 3D CPC electrodes have the minimal effect on the change in the O_2-reduction current, thereby the chronoamperogram curves of BOD at the compacted 100% GT and 60% GT-40% CNT electrodes are very similar (see Figure 5.5).

In summary, to increase the degree of apparent O_2 tolerance of hydrogenases, the 3D porous electrodes must meet one necessary condition: their pore sizes distributed between 10 nm and 70 nm. 10 nm is the minimum size for pores to be permeable to and accommodate macromolecular hydrogenases, while 70 nm is the maximum size for H_2 and O_2 to effuse through pores at ambient conditions. On the basis of such pores, increasing pore volume and electrode thickness (as long as it does not crumble away) can further improve the apparent O_2 tolerance of hydrogenases and the activity of H_2 oxidation under aerobic conditions.

5.9 A proof-of-concept experiment – O_2-sensitive hydrogenase as anodic catalyst in the membrane-less H_2 fuel cell

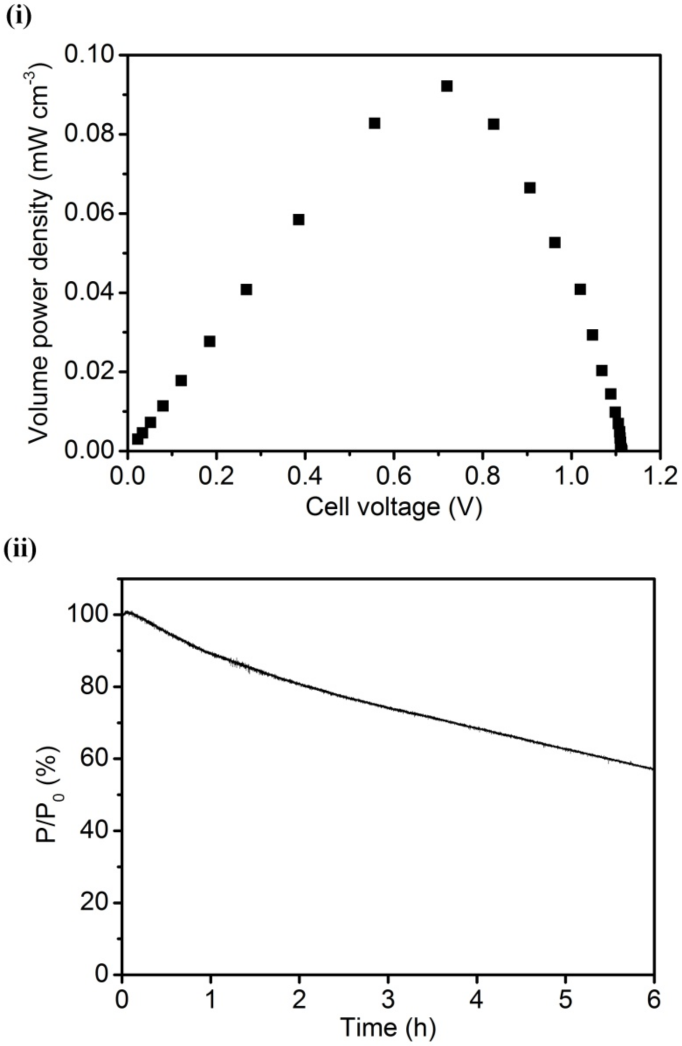

Figure 5.12. Dependence of volume power density on the cell voltage (i) and dependence of stability of power (%) with time at an applied constant potential of 0.75 V (ii) of the unit cell composed of the Hyd-2-modified compacted 100% CNT anode and the BOD-modified compacted 100% CNT cathode under an 89% H_2-11% air mixture at 20°C. Other conditions: 0.1 M sodium phosphate buffer, pH 6.0.

A proof-of-concept experiment in using the O_2-sensitive hydrogenase Hyd-2 as the anode catalyst has been conducted in the unit cell of the test bed under membrane-less, quiescent conditions in an 89% H_2-11% air mixture at 20 °C. Figure 5.12(i) shows the dependence of volume power density on the cell voltage of the unit cell composed of the Hyd-2-modified compacted 100% CNT anodes and the BOD-modified compacted 100% CNT cathodes. The OCV of this Hyd-2 fuel cell is 1.114 V, noticeably larger than that of the Hyd-1 fuel cell due to the more negative onset potential of Hyd-2. The maximum volume power density is 0.09 mW cm^{-3} (at the cell voltage of 0.72 V). Figure 5.12(ii) shows the dependence of stability of power with time for the Hyd-2 fuel cell at an applied constant potential of 0.75 V under the 89% H_2-11% air mixture at 20 °C. After continuously working for 6 hours, about 55% of the power was retained. Though the membrane-less fuel cell using Hyd-2 as the anode catalyst is inferior to its Hyd-1 counterpart, it is still interesting for an O_2-sensitive hydrogenase to work as an anode catalyst in a membrane-less fuel cell under aerobic conditions, simply based on the 3D CPC electrodes.

5.10 Conclusions

Owing to the pore size distribution of 10-70 nm, the 3D CPC electrode can separate H_2 from O_2 in its inner porous channels, thus enhancing the apparent O_2 tolerance of [NiFe]-hydrogenases. The improved O_2 tolerance of [NiFe]-hydrogenases in turn sustains the increased current/power density and lifetime due to the 3D CPC electrode. Moreover, by adjusting the pore size distribution, other gas inhibitors may be also screened out by the 3D CPC electrodes, thus capable of increasing the apparent enzyme tolerance towards those molecules. Furthermore, the enhanced apparent O_2 tolerance of [NiFe]-hydrogenases due to the 3D CPC electrode can expand the 'repertoire' in terms of fuel cell catalysts. At least, Hyd-2 can produce larger OCV than Hyd-1.

5.11 Methods

Materials: Graphite and multi-walled carbon nanotube were purchased from Sigma-Aldrich and used without further purification. Hyd-1 and Hyd-2 from *Escherichia coli* was isolated and purified as described previously.[254] Bilirubin oxidase from *Myrothecium verrucaria* was purchased from Amano Enzyme Inc and further purified by hydrophobic interaction chromatography with a HiTrap Phenyl HP hydrophobic column (GE Healthcare). Sodium dihydrogen orthophosphate and disodium hydrogen orthophosphate were purchased from Fisher Scientific and used to prepare the sodium phosphate buffer solution. The PGE electrode bases were made of pyrolytic graphite blocks (Momentive Performance Materials Ltd). Conductive silver paint (Agar Scientific) was used to glue the 3D CPC electrodes to the plates of the test bed. All aqueous solutions were prepared using deionized water from a Milli-Q water system (18 MΩ·cm).

Fabrication of the 3D CPC electrodes: A certain quantity of GT, CNT, or the mixtures of the two carbon allotropes was placed in a pellet die (Specac) and subjected to a pressure of 0.5 tonnes using a hydraulic press (Specac). Different quantities of GT, CNT, or the mixtures are required for a certain thickness of the 3D CPC electrodes. For the thickness of 0.3 mm, (1) the compacted 100% GT electrode needs 47 mg of GT; (2) the compacted 60% GT-40% CNT electrode needs 12 mg of GT and 8 mg of CNT; (3) the compacted 100% CNT electrode needs 11 mg of CNT. For the thickness of 0.2 mm, the compacted 100% CNT electrode needs 7 mg of CNT. The CPC discs were then cut to size for the required geometric area and attached to the test-bed plates using conductive silver paint. After the paint was dry, 30 µL of Hyd-1 (or Hyd-2) (4 mg mL^{-1}) was applied to the 3D CPC anode and a multiple of 30 µL (in proportion to the area ratio of cathode to anode) of BOD (6 mg mL^{-1}) was applied to the 3D CPC cathode. The enzyme-modified CPC electrodes were subsequently placed in a cold room (4 °C) for 1 h to allow sufficient permeation of enzymes into the electrodes before starting the electrochemical characterization and fuel cell tests. For the 2D carbon electrode, 5 µL of the enzyme solution (Hyd-1/Hyd-2: 4 mg mL^{-1}, BOD: 6 mg mL^{-1}) was pipetted onto the surface of the PGE electrode, which was subsequently placed in a cold room (4 °C) for 1 h and rinsed with deionized water before the electrochemical experiments.

Instrumentation: Electrochemical measurements were performed on an Ivium potentiostat (CompactStat, Ivium Technologies) in the the membrane-less fuel cell setup (Figures 5.1-5.11) as described previously[349] and the test bed (Figure 5.12) as described in Chapter 4.

All potentials were adjusted to the standard hydrogen electrode (SHE) using the relationship $E_{SHE} = E_{Ag/AgCl} + 0.206$ V at 25 °C. The ratios of H_2 to air were controlled by two mass flow controllers (Sierra Instruments).

References

1. *Energy to 2050: scenarios for a sustainable future*, Organization for Economic Co-operation and Development, 2003.

2. A. Goldthau, *The handbook of global energy policy*, Chichester: Wiley-Blackwell, 2013.

3. *World energy outlook 2008,* International Energy Agency, 2008.

4. J. Friedrichs, *The future is not what it used to be: climate change and energy scarcity*, Cambridge: MIT press, 2013.

5. F. Kreith and D. Y. Goswami, *Handbook of energy efficiency and renewable energy*, Boca Raton: CRC Press, 2007.

6. B. de Cries, *Sustainability science,* Cambridge: Cambridge University Press, 2013.

7. M. Diesendorf, *Sustainable energy solutions for climate change*, London: Routledge, 2014.

8. J. B. Heywood, *Internal combustion engine fundamentals*, New York: McGraw-Hill, 1988.

9. A. E. Lutz, R. S. Larson and J. O. Keller, *Int. J. Hydrogen Energy*, 2002, **27**, 1103-1111.

10. G. Hoogers, *Fuel cell technology handbook*, London: CRC Press, 2003.

11. *Prospects for hydrogen and fuel cells*, International Energy Agency, 2005.

12. R. H. Thring, *Fuel cells for automotive applications*, Bury St Edmunds: Professional Engineering Publishing, 2004.

13. E. Antolini, *Energy Environ. Sci.*, 2009, **2**, 915-931.

14. R. O'Hayre, S. W. Cha, W. Colella and F. B. Prinz, *Fuel cell fundamentals*, John Wiley & Sons, 2007.

15. J. S. Yi and T. V. Nguyen, *J. Electrochem. Soc.*, 1999, **146**, 38-45.

16. K. Scott, W. M. Taama and P. Argyropoulos, *J. Power Sources,* 1999, **79**, 43-59.

17. C. S. Kong, D. Y. Kim, H. K. Lee, Y. G. Shul and T. H. Lee, *J. Power Sources*, 2002, **108**, 185-191.

18. S. Um and C. Y. Wang, *J. Power Sources*, 2004, **125**, 40-51.

19. S. Litster and G. McLean, *J. Power Sources*, 2004, **130**, 61-76.

20. W.M. Qian, D. P. Wilkinson, J. Shen, H. J. Wang and J. J. Zhang, *J. Power Sources*, 2006, **154**, 202-213.

21. X. G. Li, I. Sabir and J. Park, *J. Power Sources*, 2006, **163**, 933-942.

22. L. Cindrella, A. M. Kannan, J. F. Lin, K. Saminathan, Y. Ho, C. W. Lin and J. Wertz, *J. Power Sources*, 2009, **194**, 146-160.

23. J. Kua and W. A. Goddard, *J. Am. Chem. Soc.*, 1999, **121**, 10928-10941.

24. V. Soukharev, N. Mano and A. Heller, *J. Am. Chem. Soc.*, 2004, **126**, 8368-8369.

25. Y. H. Bing, H. S. Liu, L. Zhang, D. Ghosh and J. J. Zhang, *Chem. Soc. Rev.*, 2010, **39**, 2184-2202.

26. F. Jaouen, E. Proietti, M. Lefevre, R. Chenitz, J. P. Dodelet, G. Wu, H. T. Chung. C. M. Johnston and P. Zelenay, *Energy Environ. Sci.*, 2011, **4**, 114-130.

27. Z. W. Chen, D. Higgins, A. P. Yu, L. Zhang and J. J. Zhang, *Energy Environ. Sci.*, 2011, **4**, 3167-3192.

28. Z. Yang, H. G. Nie, X. Chen, X. H. Chen and S. M. Huang, *J. Power Sources*, 2013, **236**, 238-249.

29. J. Ng, M. Tang and T. F. Jaramillo, *Energy Environ. Sci.*, 2014, **7**, 2017-2024.

30. M. Saito, N. Arimura, K. Hayamizu and T. Okada, *J. Phys. Chem. B*, 2004, **108**, 16064-16070.

31. R. Subbaraman, H. Ghassemi and T. A. Zawodzinski, *J. Am. Chem. Soc.*, 2007, **129**, 2238-2239.

32. L. M. Yan, S. H. Zhu, X. B. Ji and W. C. Lu, *J. Phys. Chem. B*, 2007, **111**, 6357-6363.

33. Y. K. Choe, E. Tsuchida, T. Ikeshoji, S. Yamakawa and S. Hyodo, *Phys. Chem. Chem. Phys.*, 2009, **11**, 3892-3899.

34. R. Jorn, J. Savage and G. A. Voth, *Acc. Chem. Res.*, 2012, **45**, 2002-2010.

35. Y. H. Zhou, J. Yang, H. B. Su, J. Zeng, S. P. Jiang and W. A. Goddard, *J. Am. Chem. Soc.*, 2014, **136**, 4954-4964.

36. D. P. Davies, P. L. Adcock, M. Turpin and S. J. Rowen, *J. Appl. Electrochem.*, 2000, **30**, 101-105.

37. J. W. Fergus, *Mater. Sci. Eng. A – Struct. Mater. Prop. Microstruct. Process*, 2005, **397**, 271-283.

38. S. Q. Hui, J. Roller, S. Yick, X. Zhang, C. Deces-Petit, Y. S. Xie, R. Maric and D. Ghosh, *J. Power Sources*, 2007, **172**, 493-502.

39. H. Rismani-Yazdi, S. M. Carver, A. D. Christy and I. H. Tuovinen, *J. Power Sources*, 2008, **180**, 683-694.

40. R. Anderson, M. Blanco, X. T. Bi and D. P. Wilkinson, *Int. J. Hydrogen Energy*, 2012, **37**, 16093-16103.

41. T. J. Mason, J. Millichamp, T. P. Neville, P. R. Shearing, S. Simons and D. Brett, *J. Power Sources*, 2013, **242**, 70-77

42. Y. B. Zhou, K. Jiao, Q. Du, Y. Yin and X. G. Li, *Int. J. Hydrogen Energy*, 2013, **38**, 12891-12903.

43. H. Y. Kim, S. Jeon, M. Song and K. Kim, *J. Power Sources*, 2014, **246**, 679-695.

44. S. Tanaka and T. Shudo, *J. Power Sources*, 2014, **248**, 524-532.

45. X. Li, *Principles of fuel cells*, London: Taylor & Francis, 2006.

46. P. W. Atkins and J. de Paula, *Atkins' Physical Chemistry (8th ed.)*, Oxford: Oxford University Press, 2006.

47. A. J. Appleby and F. R. Foulkes, *Fuel cell handbook*, New York: Van Nostrand Reinhold, 1989.

48. A. Wieckowski and J. K. Norskov, *Fuel cell science: theory, fundamentals and biocatalysis*, Hoboken, NJ: Wiley, 2010.

49. W. Vielstich, A. Lamm and H. A. Gasteiger, *Handbook of fuel cells: fundamentals, technology and applications*, Chichester: Wiley, 2003.

50. R. G. Compton and C. E. Banks, *Understanding voltammetry (2nd edition)*, London: Imperial College Press, 2011.

51. A. J. Bard and L. R. Faulkner, *Electrochemical methods: fundamentals and applications (2nd edition)*, New York: Wiley, 2001.

52. H. H. Girault, *Analytical and physical electrochemistry*, Lausanne: EPFL press, 2004.

53. C. G. Zoski, *Handbook of electrochemistry*, Amsterdam: Elsevier, 2007.

54. E. Santos and W. Schmickler, *Catalysis in electrochemistry: from fundamentals to strategies for fuel cell development*, Hoboken: Wiley, 2011.

55. J. Zhang, *PEM fuel cell electrocatalysts and catalyst layers: fundamentals and applications*, London: Springer, 2008.

56. M. Soustelle, *An introduction to chemical kinetics*, London: ISTE, 2011.

57. J. Larminie and A. Dicks, *Fuel cell systems explained (2nd edition)*, Chichester: Wiley, 2003.

58. A. M. Herring, T. A. Zawodzinski and S. J. Hamrock, *Fuel cell chemistry and operation*, Washington DC: American Chemical Society, 2010.

59. G. Dagan, *Flow and transport in porous formations*, London: Springer Verlag, 1989.

60. R. B. Bird, W. E. Stewart and E. N. Lightfoot, *Transport phenomena* (2nd edition), New York: Wiley, 2002.

61. K. Scott, W. M. Taama, S. Kramer, P. Argyropoulos and K. Sundmacher, *Electrochim. Acta*, 1999, **45**, 945-957.

62. S. H. Chan, C. F. Low and O. L. Ding, *J. Power Sources*, 2002, **103**, 188-200.

63. S. Um and C. Y. Wang, *J. Power Sources*, 2004, **125**, 40-51.

64. F. Zhao, F. Harnisch, U. Schrorder, F. Scholz, P. Bogdanoff and I. Herrmann, *Environ. Sci. Technol.*, 2006, **40**, 5193-5199.

65. M. Inaba, T. Kinumoto, M. Kiriake, R. Umebayashi, A. Tasaka and Z. Ogumi, *Electrochim. Acta*, 2006, **51**, 5746-5753.

66. J. T. Gostick, M. A. Ioannidis, M. W. Fowler and M. D. Pritzker, *J. Power Sources*, 2007, **173**, 277-290.

67. Y. S. Li, T. S. Zhao and Z. X. Liang, *J. Power Sources*, 2009, **187**, 387-392.

68. G. J. K. Acres, *J. Power Sources*, 2001, **100**, 60-66.

69. M. L. Perry and T. F. Fuller, *J. Electrochem. Soc.*, 2002, **149**, S59-S67.

70. E. Gulzow, *J. Power Sources*, 1996, **61**, 99-104.

71. G. F. McLean, T. Niet, S. Prince-Richard and N. Djilali, *Int. J. Hydrogen Energy*, 2002, **27**, 507-526.

72. T. Tomida and I. Nakabayashi, *J. Electrochem. Soc.*, 1989, **136**, 3296-3298.

73. M. A. Alsaleh, S. Gultekin, A. S. Alzakri and H. Celiker, *Int. J. Hydrogen Energy*, 1994, **19**, 713-718.

74. M. Schulze, E. Gulzow and G. Steinhiber, *Appl. Surf. Sci.*, 2001, **179**, 251-256.

75. F. Bidault, D. J. L. Brett, P. H. Middleton and N. P. Brandon, *J. Power Sources*, 2009, **187**, 39-48.

76. M. T. Ergul, L. Turker and I. Eroglu, *Int. J. Hydrogen Energy*, 1997, **22**, 1039-1045.

77. S. Gultekin, M. A. Alsaleh, A. S. Alzakri and K. A. A. Abbas, *Int. J. Hydrogen Energy*, 1996, **21**, 485-489.

78. V. Ahuja and R. Green, *Int. J. Hydrogen Energy*, 1998, **23**, 131-137.

79. A. Tewari, V. Sambhy, M. U. Macdonald and A. Sen, *J. Power Sources*, 2006, **153**, 1-10.

80. K. Joon, *J. Power Sources*, 1996, **61**, 129-133.

81. S. T. Kuk, Y. S. Song and K. Kim, *J. Power Sources*, 1999, **83**, 50-56.

82. B. Z. Fang and H. Chen, *J. Electroanal. Chem.*, 2001, **501**, 128-131.

83. P. Ganesan, H. Colon, B. Haran and B. N. Popov, *J. Power Sources*, 2003, **115**, 12-18.

84. N. J. Cherepy, R. Krueger, K. J. Fiet, A. F. Jankowski and J. F. Cooper, *J. Electrochem. Soc.*, 2005, **152**, A80-A87.

85. D. X. Cao, Y. Sun and G. L. Wang, *J. Power Sources*, 2007, **167**, 250-257.

86. A. C. Rady, S. Giddey, S. P. S. Badwal, B. P. Ladewig and S. Bhattacharya, *Energy Fuels*, 2012, **26**, 1471-1488.

87. R. J. Berger, E. B. M. Doesburg, J. G. van Ommen and J. R. H. Ross, *Appl. Catal. A-Gen.*, 1996, **143**, 343-365.

88. J. L. Silveira, E. M. Leal and L. F. Ragonha, *Energy*, 2001, **26**, 891-904.

89. N. Tomimatsu, H. Ohzu, Y. Akasaka and K. Nukagawa, *J. Electrochem. Soc.*, 1997, **144**, 4182-4186.

90. S. Terada, I. Nagashima, K. Higaki and Y. Ito, *J. Power Sources*, 1998, **75**, 223-229.

91. E. Antolini, *Appl. Energy*, 2011, **88**, 4274-4293.

92. G. Manzolini, S. Campanari, P. Chiesa, A. Giannotti, P. Bedont and F. Parodi, *J. Fuel Cell Sci. Technol.*, 2012, **9**, 0110181-0110188.

93. C. G. Lee, K. S. Ahn, H. C. Lim and J. M. Oh, *J. Power Sources*, 2004, **125**, 166-171.

94. S. Freni, S. Cavallaro, M. Aquino, D. Ravida and N. Giordano, *Int. J. Hydrogen Energy*, 1994, **19**, 337-341.

95. A. C. Schoeler, T. D. Kaun, I. Bloom, M. Lanagan and M. Krumpelt, *J. Electrochem. Soc.*, 2000, **147**, 916-921.

96. K. Takeuchi, A. Nishijima, K. Ui, N. Koura and C. K. Loong, *J. Electrochem. Soc.*, 2005, **152**, B364-B368.

97. A. J. Appleby, *J. Power Sources*, 1996, **58**, 153-176.

98. N. Sammes, R. Bove and K. Stahl, *Curr. Opin. Solid State Mat. Sci.*, 2004, **8**, 372-378.

99. D. R. Desena, E. R. Gonzalez and E. A. Ticianelli, *Electrochim. Acta*, 1992, **37**, 1855-1858.

100. D. Chu, *Electrochem. Acta*, 1998, **43**, 3711-3718.

101. T. Saito, M. Nishioka, Y. Itoh, Y. Miyake, S. Murakami and N. Furukawa, *J. Power Sources*, 1992, **37**, 347-354.

102. M. Ghouse, H. Abaoud, A. Al-Boeiz and M. AbdulHadi, *Appl. Energy*, 1998, **60**, 153-167.

103. E. Passalacqua, P. L. Antonucci, M. Vivaldi, A. Patti, V. Antonucci, N. Giordano and K. Kinoshita, *Electrochim. Acta*, 1992, **37**, 2725-2730.

104. L. D. Burke, J. K. Casey, J. A. Morrissey and J. F. Osullivan, *J. Appl. Electrochem.*, 1994, **24**, 30-37.

105. T. Torre, A. S. Arico, V. Alderucci, V. Antonucci and N. Giordano, *Appl. Catal. A-Gen.*, 1994, **114**, 257-272.

106. J. R. Chang, J. F. Lee, S. D. Lin and A. S. Lin, *J. Phys. Chem.*, 1995, **99**, 14798-14804.

107. D. T. Chin and P. D. Howard, *J. Electrochem. Soc.*, 1986, **133**, 2447-2450.

108. R. H. Song and D. R. Shin, *Int. J. Hydrogen Energy*, 2001, **26**, 1259-1262.

109. Q. F. Li, R. H. He, J. A. Gao, J. O. Jensen and N. J. Bjerrum, *J. Electrochem. Soc.*, 2003, **150**, A1599-A1605.

110. H. Hirata, T. Aoki and K. Nakajima, *J. Power Sources*, 2011, **196**, 8004-8011.

111. M. Wakizoe, O. A. Velev and S. Srinivasan, *Electrochim. Acta*, 1995, **40**, 335-344.

112. D. E. Curtin, R. D. Lousenberg, T. J. Henry, P. C. Tangeman and M. E. Tisack, *J. Power Sources*, 2004, **131**, 41-48.

113. R. Souzy and B. Ameduri, *Prog. Polym. Sci.*, 2005, **30**, 644-687.

114. K. A. Starz, E. Auer, T. Lehmann and R. Zuber, *J. Power Sources*, 1999, **84**, 167-172.

115. M. Oszcipok, M. Zedda, J. Hesselmann, M. Huppman, M. Wodrich, M. Junghardt and C. Hebling, *J. Power Sources*, 2006, **157**, 666-673.

116. Y. G. Yoon, G. G. Park, T. H. Yang, J. N. Han, W. Y. Lee and C. S. Kim, *Int. J. Hydrogen Energy*, 2003, **28**, 657-662.

117. D. Staschewski, *Int. J. Hydrogen Energy*, 1996, **21**, 381-385.

118. K. H. Choi, D. J. Park, Y. W. Rho, Y. T. Kho and T. H. Lee, *J. Power Sources*, 1998, **74**, 146-150.

119. P. Sridhar, R. Perumal, N. Rajalakshmi, A. Raja and K. S. Dhathathreyan, *J. Power Sources*, 2001, **101**, 72-78.

120. M. Murphy, M. Esayian, A. Hobson, S. MacKenzie, W. K. Lee and J. W. Van Zee, *J. Electrochem. Soc.*, 2001, **148**, A1141-A1147.

121. Z. G. Qi, C. Z. He and A. Kaufman, *J. Power Sources*, 2002, **111**, 239-247.

122. R. Mohtadi, W. K. Lee, S. Cowan, J. W. Van Zee and M. Murphy, *Electrochem. Solid State Lett.*, 2003, **6**, A272-A274.

123. W. Y. Shi, B. L. Yi, M. Hou and Z. G. Shao, *Int. J. Hydrogen Energy*, 2007, **32**, 4412-4417.

124. H. M. Yu, Z. J. Hou, B. L. Yi and Z. Y. Lin, *J. Power Sources*, 2002, **105**, 52-57.

125. D. C. Papageorgopoulos, M. Keijzer and F. A. de Bruijn, *Electrochim. Acta*, 2002, **48**, 197-204.

126. Y. H. Li, J. F. Chen, J. Ding, Z. Q. Mao, C. L. Xu and D. H. Wu, *J. Inorg. Mater.*, 2004, **19**, 629-633.

127. S. Mukerjee, R. C. Urian, S. J. Lee, E. A. Ticianelli and J. MeBreen, J. *Electrochem. Soc.*, 2004, **151**, A1094-A1103.

128. T. Lopes, V. A. Paganin and E. R. Gonzalez, Int. J. Hydrogen Energy, 2011, 36, 13703-13707.

129. S. H. Ge, X. G. Li and I. M. Hsing, *J. Electrochem. Soc.*, 2004, **151**, B523-B528.

130. J. Chen, T. Matsuura and M. Hori, *J. Power Sources*, 2004, **131**, 155-161.

131. K. T. Adjemian, S. Srinivasan, J. Benziger and A. B. Bocarsly, *J. Power Sources*, 2002, **109**, 356-364.

132. Q. F. Li, R. H. He, J. O. Jensen and N. J. Bjerrum, *Chem. Mater.*, 2003, **15**, 4896-4915.

133. M. Murphy, M. E. Esayian, W. K. Lee and J. W. Van Zee, *J. Electrochem. Soc.*, 2003, **150**, A29-A34.

134. J. L. Zhang, Z. Xie, J. J. Zhang, Y. H. Tanga, C. J. Song, T. Navessin, Z. Q. Shi, D. T. Song, H. J. Wang, D. P. Wilkinson, Z. S. Liu and S. Holdcroft, *J. Power Sources*, 2006, **160**, 872-891.

135. D. Gomes and S. P. Nunes, *J. Membrane Sci.*, 2008, **321**, 114-122.

136. B. Wang, *J. Power Sources*, 2005, **152**, 1-15.

137. N. P. Subramanian, S. P. Kumaraguru, H. Colon-Mercado, H. Kim, B. N. Popov, T. Black and D. A. Chen, *J. Power Sources*, 2006, **157**, 56-63.

138. Y. Y. Shao, J. H. Sui, G. P Yin and Y. Z. Gao, *Appl. Catal. B-Environ.*, 2008, **79**, 89-99.

139. G. S. Tasic, S. S. Miljanic, M. P. M. Kaninski, D. P. Saponjic and V. M. Nikolic, *Electrochem. Commun.*, 2009, **11**, 2097-2100.

140. Y. W. Ma, H. M. Zhang, H. X. Zhong, T. Xu, H. Jin, Y. F. Tang and Z. Xu, *Electrochim. Acta*, 2010, **55**, 7945-7950.

141. R. Othman, A. L. Dicks and Z. H. Zhu, *Int. J. Hydrogen Energy*, 2012, **37**, 357-372.

142. J. L. Zhang, H. M. Zhang, J. F. Wu and J. J. Zhang, *PEM fuel cell testing and diagnosis*, Amsterdam: Elsevier, 2013.

143. X. L. Cheng, B. L. Yi, M. Han, J. X. Zhang, Y. G. Qiao and J. R. Yu, *J. Power Sources*, 1999, **79**, 75-81.

144. G. G. Park, Y. J. Sohn, T. H. Yang, Y. G. Yoon, W. Y. Lee and C. S. Kim, *J. Power Sources*, 2004, **131**, 182-187.

145. M. Han, J. H. Xu, S. H. Chan and S. P. Jiang, *Electrochim. Acta*, 2008, **53**, 5361-5367.

146. T. Astill, Z. Xie, Z. Q. Shi, T. Navessin and S. Holdcroft, *J. Electrochem. Soc.*, 2009, **156**, B499-B508.

147. Z. G. Qi and A. Kaufman, *J. Power Sources*, 2002, **109**, 38-46.

148. S. Lertviriyapaisan and N. Tantavichet, *Int. J. Hydrogen Energy*, 2010, **35**, 10464-10471.

149. Y. G. Chun, C. S. Kim, D. H. Peck and D. R. Shin, *J. Power Sources*, 1998, **71**, 174-178.

150. Y. G. Yoon, T. H. Yang, G. G. Park, W. Y. Lee and C. S. Kim, *J. Power Sources*, 2003, **118**, 189-192.

151. X. W. Yu and S. Y. Ye, *J. Power Sources*, 2007, **172**, 145-154.

152. S. S. Zhang, X. Z. Yuan, J. N. C. Hin, H. J. Wang, K. A. Friedrich and M. Schulze, *J. Power Sources*, 2009, **194**, 588-600.

153. G. Bender, T. A. Zawodzinski and A. P. Saab, *J. Power Sources*, 2003, **124**, 114-117.

154. T. Frey and M. Linardi, *Electrochim. Acta*, 2004, **50**, 99-105.

155. M. Prasanna, E. A. Cho, T. H. Lim and I. H. Oh, *Electrochim. Acta*, 2008, **53**, 5434-5441.

156. D. Chu and R. Z. Jiang, *J. Power Sources*, 1999, **80**, 226-234.

157. E. A. Cho, U. S. Jeon, S. A. Hong, I. H. Oh and S. G. Kang, *J. Power Sources*, 2005, **142**, 177-183.

158. R. Stobart, *Fuel cell technology for vehicles*, Warrendale: Society of Automotive Engineers, 2001.

159. S. Y. Lee, E. Cho, J. H. Lee, H. J. Kim, T. H. Lim, I. H. Oh and J. Won, *J. Electrochem. Soc.*, 2007, **154**, B194-B200.

160. J. J. Hwang, D. Y. Wang and N. C. Shih, *J. Power Sources*, 2005, **141**, 108-115.

161. R. A. Bullen, T. C. Arnot, J. B. Lakeman and F. C. Walsh, *Biosens. Bioelectron.*, 2006, **21**, 2015-2045.

162. F. Davies and S. P. J. Higson, *Biosens. Bioelectron.*, 2007, **22**, 1224-1235.

163. N. Q. Minh, *Solid State Ion.*, 2004, **174**, 271-277.

164. H. Yanagida, K. Komoto, M. Miyayama and H. Yamada, *The chemistry of ceramics*, New York: Wiley, 1996.

165. F. T. Ciacchi, K. M. Crane and S. P. S. Badwal, *Solid State Ion.*, 1994, **73**, 49-61.

166. M. Brown, S. Primdahl and M. Mogensen, *J. Electrochem. Soc.*, 2000, **147**, 475-485.

167. S. P. Jiang and S. H. Chan, *J. Mater. Sci.*, 2004, **39**, 4405-4439.

168. C. W. Sun, R. Hui and J. Roller, *J. Solid State Electrochem.*, 2010, **14**, 1125-1144.

169. S. C. Singhal, *Solid State Ion.*, 2000, **135**, 305-313.

170. C. R. Xia, W. Rauch, F. L. Chen and M. L. Liu, *Solid State Ion.*, 2002, **149**, 11-19.

171. Q. L. Liu, K. A. Khor and S. H. Chan, *J. Power Sources*, 2006, **161**, 123-128.

172. X. G. Zhang, M. Robertson, S. Yick, C. Deces-Petit, E. Styles, W. Qu, Y. S. Xie, R. Hui, J. Roller, O. Kesler, R. Maic and D. Ghosh, *J. Power Sources*, 2006, **160**, 1211-1216.

173. B. E. Logan, B. Hamelers, R. A. Rozendal, U. Shrorder, J. Keller, S. Freguia, P. Aelterman, W. Verstraete and K. Rabaey, *Environ. Sci. Technol.*, 2006, **40**, 5181-5192.

174. Z. W. Du, H. R. Li and T. Y. Gu, *Biotechnol. Adv.*, 2007, **25**, 464-482.

175. D. Pant, G. van Bogaert, L. Diels and K. Vanbroekhoven, *Bioresource Technol.*, 2009, **101**, 1533-1543.

176. K. Rabaey and W. Verstraete, *Trends Biotechnol.*, 2005, **23**, 291-298.

177. D. R. Lovley, *Curr. Opin. Biotechnol.*, 2006, **17**, 327-332.

178. B. E. Logan, *Microbial fuel cells*, Hoboken: Wiley, 2008.

179. H. Liu, S. A. Cheng and B. E. Logan, *Environ. Sci. Technol.*, 2005, **39**, 5488-5493.

180. G. S. Jadhav and M. M. Ghangrekar, *Bioresource Technol.*, 2009, **100**, 717-723.

181. A. G. del Campo, J. Lobato, P. Canizares, M. A. Rodrigo and F. J. F. Morales, *Appl. Energy*, 2013, **101**, 213-217.

182. D. H. Park and J. G. Zeikus, *Appl. Environ. Microbiol.*, 2000, **66**, 1292-1297.

183. C. J. Sund, S. McMasters, S. R. Crittenden, L. E. Harrell and J. J. Sumner, *Appl. Microbiol. Biotechnol.*, 2007, **76**, 561-568.

184. M. Rahimnejad, G. D. Najafpour, A. A. Ghoreyshi, F. Talebnia, G. C. Premier, G. Bakeri, J. R. Kim and S. E. Oh, *J. Microbiol.*, 2012, **50**, 575-580.

185. J. K. Jang, T. H. Pham, I. S. Chang, K. H. Kang, H. Moon, K. S. Cho and B. H. Kim, *Process Biochem.*, 2004, **39**, 1007-1012.

186. H. J. Kim, H. S. Park, M. S. Hyun, I. S. Chang, M. Kim and B. H. Kim, *Enzyme Microb. Technol.*, 2002, **30**, 145-152.

187. S. K. Chaudhuri and D. R. Lovley, *Nat. Biotechnol.*, 2003, **21**, 1229-1232.

188. T. Zhang, C. Z. Cui, S. L. Chen, X. P. Ai, H. X. Yang, S. Ping and Z. R. Peng, Chem. Commun., 2006, 21, 2257-2259.

189. D. Prasad, S. Arun, A. Murugesan, S. Padmanaban, R. S. Satyanarayanan, S. Berchmans and V. Yegnaraman, *Biosens. Bioelectron.*, 2007, **22**, 2604-2610.

190. H. Liu, R. Ramnarayanan and B. E. Logan, *Environ. Sci. Technol.*, 2004, **38**, 2281-2285.

191. Z. He, S. D. Minteer and L. T. Angenent, *Environ. Sci. Technol.*, 2005, **39**, 5262-5267.

192. R. Cammack, M. Frey and R. Robson, *Hydrogen as a fuel: learning from nature*, London: Taylor & Francis, 2001.

193. C. Tard and C. J. Pickett, *Chem. Rev.*, 2009, **109**, 2245-2274.

194. M. L. Helm, M. P. Stewart, R. M. Bullock, M. R. DuBois and D. L. DuBois, *Science*, 2011, **333**, 863-866.

195. S. Ogo, K. Ichikawa, T. Kishima, T. Matsumoto, H. Nakai, K. Kusaka and T. Ohhara, *Science*, 2013, **339**, 682-684.

196. A. K. Jones, E. Sillery, S. P. J. Albracht and F. A. Armstrong, *Chem. Commun.*, 2002, 866-867.

197. T. W. Woolerton and K. A. Vincent, *Electrochim. Acta*, 2009, **54**, 5011-5017.

198. S. Schuler and R. Conrad, *FEMS Microbial. Ecol.*, 1990, **73**, 77-83.

199. R. Nandi and S. Sengupta, *Crit. Rev. Microbiol.*, 1998, **24**, 61-84.

200. D. Das and T. N. Veziroglu, *Int. J. Hydrogen Energy*, 2001, **26**, 13-28.

201. P. Tamagnini, R. Axelsson, P. Lindberg, F. Oxelfelt, R. Wunschiers and P. Lindbald, *Microbiol. Mol. Biol. Rev.*, 2002, **66**, 1-20.

202. P. C. Hallenbeck, *Water Sci. Technol.*, 2005, **52**, 21-29.

203. R. Conrad, *Microbiol. Rev.*, 1996, **60**, 609-640.

204. J. Sorensen, D. Christensen and B. B. Jorgensen, *Appl. Environ. Microbiol.*, 1981, **42**, 5-11.

205. D. R. Lovley, *Appl. Environ. Microbiol.*, 1985, **49**, 1530-1531.

206. H. D. Kluber, S. Lechner and R. Conrad, *FEMS Microbial. Ecol.*, 1995, 16, 167-175.

207. M. Ludwig, J. A. Cracknell, K. A. Vincent, F. A. Armstrong and O. Lenz, *J. Biol. Chem.*, 2009, **284**, 465-477.

208. M. Nemati, T. J. Mazutinec, G. E. Jenneman and G. Voordouw, *J. Ind. Microbiol. Biotechnol.*, 2001, **26**, 350-355.

209. P. M. Vignais and A. Colbeau, *Curr. Issues Mol. Biol.*, 2004, **6**, 159-188.

210. F. A. Armstrong, N. A. Belsey, J. A. Cracknell, G. Goldet, A. Parkin, E. Reisner, K. A. Vincent and A. F. Wait, *Chem. Soc. Rev.*, 2009, **38**, 36-51.

211. D. J. Evans and C. J. Pickett, *Chem. Soc. Rev.*, 2003, **32**, 268-275.

212. K. A. Vincent, A. Parkin and F. A. Armstrong, *Chem. Rev.*, 2007, **107**, 4366-4413.

213. W. Lubitz, H. Ogata, O. Rüdiger and E. Reijerse, *Chem. Rev.*, 2014, **114**, 4081-4148.

214. F. A. Armstrong, *Photosynth. Res.*, 2009, **102**, 541-550.

215. A. A. Hamdan, S. Dementin, P. P. Liebgott, O. Gutierrez-Sanz, P. Richaud, A. L. de Lacey, M. Rousset, P. Bertrand, L. Cournac and C. *Léger*, *J. Am. Chem. Soc.*, 2012, **134**, 8368-8371.

216. B. J. Murphy, F. Sargent and F. A. Armstrong, *Energy Environ. Sci.*, 2014, **7**, 1426-1433.

217. A. Parkin, G. Goldet, C. Cavazza, J. C. Fontecilla-Camp and F. A. Armstrong, *J. Am. Chem. Soc.*, 2008, **130**, 13410-13416.

218. M. Corr and J. A. Murphy, *Chem. Soc. Rev.*, 2011, **40**, 2279-2292.

219. P. M. Matias, C. M. Soares, L. M. Saraiva, R. Coelho, J. Morais, J. Le Gall and M. A. Carrondo, *J. Biol. Inorg. Chem.*, 2001, **6**, 63-81.

220. A. Volbeda, L. Martin, C. Cavazza, M. Matho, B. W. Faber, W. Roseboom, S. P. J. Albracht, E. Garcin, M. Rousset and J. C. Fontecilla-Camps, *J. Biol. Inorg. Chem.*, 2005, **10**, 239-249.

221. H. Ogata, S. Hirota, A. Nakahara, H. Komori, N. Shibata, T. Kato, K. Kano and Y. Higuchi, *Structure*, 2005, **13**, 1635-1642.

222. F. A. Cotton, *Advanced inorganic chemistry (6th edition)*, New York: Wiley, 1999.

223. A. Volbeda, E. Garcin, C. Piras, A. L. de Lacey, V. M. Fernandez, E. C. Hatchikian, M. Frey and J. C. Fontecilla-Camps, *J. Am. Chem. Soc.*, 1996, **118**, 12989-12996.

224. Y. Higuchi, T. Yagi and N. Yasuoka, *Structure*, 1997, **5**, 1671-1680.

225. M. Carepo, D. L. Tierney, C. D. Brondino, T. C. Yang, A. Pamplona, J. Telser, I. Moura, J. J. G. Moura and B. M. Hoffman, *J. Am. Chem. Soc.*, 2002, **124**, 281-286.

226. C. C. Page, C. C. Moser, X. X. Chen and P. L. Dutton, *Nature*, 1999, **402**, 47-52.

227. A. Voeda, M. H. Charon, C. Piras, E. C. Hatchikian, M. Frey and J. C. Fontecilla-Camps, *Nature*, 1995, **373**, 580-587.

228. J. Fritsch, P. Scheerer, S. Frielingsdorf, S. Kroschinsky, B. Friedrich, O. Lenz and C. M. T. Spahn, *Nature*, 2011, **479**, 249-252.

229. Y. Shomura, K. S. Yoon, H. Nishihara and Y. Higuchi, *Nature*, 2011, **479**, 253-256.

230. Y. Montet, P. Amara, A. Volbeda, X. Verneda, E. C. Hatchikian, M. J. Field, M. Frey and J. C. Fontecilla-Camps, *Nat. Struct. Biol.*, 1997, **4**, 523-526.

231. V. H. Teixeira, A. M. Baptista and C. M. Soares, *Biophys. J.*, 2006, **91**, 2035-2045.

232. H. Ogata, W. Lubitz and Y. Higuchi, *Dalton Trans.*, 2009, 7577-7587.

233. F. Leroux, S. Dementin, B. Burlatt, L. Cournac, A. Volbeda, S. Champ, L. Martin, B. Guigliarelli, P. Bertrand, J. C. Fontecilla-Camp, M. Rousset and C. Léger, *Proc. Natl. Acad. Sci. U. S. A.*, 2008, **105**, 11188-11193.

234. T. Buhrke, O. Lenz, N. Krauss and B. Friedrich, *J. Biol. Chem.*, 2005, **280**, 23791-23796.

235. S. Dementin, F. Leroux, L. Cournac, A. L. de Lacey, A. Volbeda, C. Léger, B. Burlat, N. Martinez, S. Champ, L. Martin, O. Sanganas, M. Haumann, V. M. Fernandez, B. Guigliarelli, J. C. Fontecilla-Camp and M. Rousset, *J. Am. Chem. Soc.*, 2009, **131**, 10156-10164.

236. V. H. Teixeira, C. M. Soares and A. M. Baptista, *Proteins: Struct. Funct. Bioinf.*, 2008, **70**, 1010-1022.

237. I. F. Galvan, A. Volbeda, J. C. Fontecilla-Camps and M. J. Field, *Proteins: Struct. Funct. Bioinf.*, 2008, **73**, 195-203.

238. J. E. Huyett, M. Carepo, A. Pamplona, R. Franco, I. Moura, J. J. G. Moura and B. M. Hoffman, *J. Am. Chem. Soc.*, 1997, **119**, 9291-9292.

239. W. Lubitz, E. Reijerse and M. van Gastel, *Chem. Rev.*, 2007, **107**, 4331-4365.

240. M. E. Pandelia, V. Fourmond, P. Tron-Infossi, E. Lojou, P. Bertrand, C. Léger, M. T. Giudici-Orticoni and W. Lubitz, *J. Am. Chem. Soc.*, 2010, **132**, 6991-7004.

241. C. Fichtner, C. Laurich, E. Bothe and W. Lubitz, *Biochemistry,* 2006, **45**, 9706-9716.

242. M. E. Pandelia, H. Ogata and W. Lubitz, *ChemPhysChem*, 2010, **11**, 1127-1140.

243. M. Horch, L. Lauterbach, M. Saggu, P. Hildebrandt, F. Lendzian, R. Bittl, O. Lenz and I. Zebger, *Angew. Chem. Int. Ed.*, 2010, **49**, 8026-8029.

244. A. A. Hamdan, B. Burlat, O. Gutiérrez-Sanz, P. P. Liebgott, C. Baffert, A. L. de Lacey, M. Rousset, B. Guigliarelli, *C.* Léger and S. Dementin, *Nat. Chem. Biol.*, 2013, **9**, 15-17.

245. P. E. M. Siegbahn, J. W. Tye and M. B. Hall, *Chem. Rev.*, 2007, **107**, 4414-4435.

246. F. A. Armstrong, *Curr. Opin. Chem. Biol.*, 2004, **8**, 133-140.

247. S. E. Lamle, S. P. J. Albracht and F. A. Armstrong, *J. Am. Chem. Soc.*, 2004, **126**, 14899-14909.

248. A. K. Jones, S. E. Lamle, H. R. Pershad, K. A. Vincent, S. P. J. Albracht and F. A. Armstrong, *J. Am. Chem. Soc.*, 2003, **125**, 8505-8514.

249. J. C. Fontecilla-Camps, A. Volbeda, C. Cavazza and Y. Nicolet, *Chem. Rev.*, 2007, **107**, 4273-4303.

250. S. E. Lamle, K. A. Vincent, L. M. Halliwell, S. P. J. Albracht and F. A. Armstrong, *J. Am. Chem. Soc.*, 2003, **21**, 4152-4157.

251. K. A. Vincent, N. A. Belsey, W. Lubitz and F. A. Armstrong, *J. Am. Chem. Soc.*, 2006, **128**, 7448-7449.

252. K. A. Vincent, J. A. Cracknell, O. Lenz, I. Zebger, B. Friedrich and F. A. Armstrong, *Proc. Natl. Acad. Sci. U. S. A.*, 2005, **102**, 16951-16954.

253. M. E. Pandelia, P. Infossi, M. T. Giudici-Orticoni and W. Lubitz, *Biochemistry*, 2010, **49**, 8873-8881.

254. M. J. Lukey, A. Parkin, M. M. Röβler, B. J. Murphy, J. Harmer, T. Palmer, F. Sargent and F. A. Armstrong, *J. Biol. Chem.*, 2010, **285**, 3928-3938.

255. S. V. Hexter, M. W. Chung, K. A. Vincent and F. A. Armstrong, *J. Am. Chem. Soc.*, 2014, **136**, 10470-10477.

256. Y. Higuchi, H. Ogata, K. Miki, N. Yasuoka and T. Yagi, *Struct. Fold. Des.*, 1999, **7**, 549-556.

257. M. Higuchi and T. Yagi, *Biochem. Biophys. Res. Commun.*, 1999, **255**, 295-299.

258. S. T. Stripp, G. Goldet, C. Brandmayr, O. Sanganas, K. A. Vincent, M. Haumann, F. A. Armstrong and T. Happe, *Proc. Natl. Acad. Sci. U. S. A.*, 2009, **106**, 17331-17336.

259. J. A. Cracknell, A. F. Wait, O. Lenz, B. Friedrich and F. A. Armstrong, *Proc. Natl. Acad. Sci. U. S. A.*, 2009, **106**, 20681-20686.

260. K. A. Vincent, J. A. Cracknell, J. R. Clark, M. Ludwig, O. Lenz, B. Friedrich and F. A. Armstrong, *Chem. Commun.*, 2006, **48**, 5033-5035.

261. K. A. Vincent, A. Parkin, O. Lenz, S. P. J. Albracht, J. C. Fontecilla-Camps, R. Cammack, B. Friedrich and F. A. Armstrong, *J. Am. Chem. Soc.*, 2005, **127**, 18179-18189.

262. T. Goris, A. F. Wait, M. Saggu, J. Fritsch, N. Heidary, M. Stein, I. Zebger, F. Lendzian, F. A. Armstrong, B. Friedrich and O. Lenz, *Nat. Chem. Biol.*, 2011, **7**, 310-318.

263. A. Volbeda, P. Amara, C. Darnault, J. M. Mouesca, A. Parkin, M. M. Röβler, F. A. Armstrong and J. C. Fontecilla-Camps, *Proc. Natl. Acad. Sci.*, 2012, **109**, 5305-5310.

264. M. M. Röβler, R. M. Evans, R. A. Davies, J. Harmer and F. A. Armstrong, *J. Am. Chem. Soc.*, 2012, **134**, 15581-15594.

265. R. M. Evans, A. Parkin, M. M. Röβler, B. J. Murphy, H. Adamson, M. J. Lukey, F. Sargent, A. Volbeda, J. C. Fontecilla-Camps and F. A. Armstrong, *J. Am. Chem. Soc.*, 2013, **135**, 2694-2707.

266. T. Toda, H. Igarashi, H. Uchida and M. Watanabe, *J. Electrochem. Soc.*, 1999, **146**, 3750-3756.

267. O. Antoine, Y. Bultel and R. Durand, *J. Electrochem. Soc.*, 2001, **499**, 85-94.

268. K. P. Gong, F. Du, Z. H. Xia, M. Durstock and L. M. Dai, *Science*, 2009, **323**, 760-764.

269. B. Lim, M. J. Jiang, P. H. C. Camargo, E. C. Cho, J. Tao, X. M. Lu, Y. M. Zhu and Y. N. Xia, *Science*, 2009, **324**, 1302-1305.

270. E. I. Solomon, P. Chen, M. Metz, S. K. Lee and A. E. Palmer, *Angew. Chem. Int. Ed.*, 2001, **40**, 4570-4590.

271. C. F. Blanford, C. E. Foster, R. S. Heath and F. A. Armstrong, *Faraday Discuss.*, 2008, **140**, 319-335.

272. L. dos Santos, V. Climent, C. F. Blanford and F. A. Armstrong, *Phys. Chem. Chem. Phys.*, 2010, **12**, 13962-13974.

273. F. Barriere, Y. Ferry, D. Rochefort and D. Leech, *Electrochem. Commun.*, 2004, **6**, 237-241.

274. L. Brunel, J. Denele, K. Servat, K. B. Kokoh, C. Jolivalt, C. Innocent, M. Cretin, M. Rolland and S. Tingry, *Electrochem. Commun.*, 2007, **9**, 331-336.

275. Y. Kamitaka, S. Tsujimura, N. Setoyama, T. Kajino and K. Kano, *Phys. Chem. Chem. Phys.*, 2007, **9**, 1793-1801.

276. X. Wu, F. Zhao, J. R. Varcoe, A. E. Thumser, C. Avignone-Rossa and R. C. T. Slade, *Biosens. Bioelectron.*, 2009, **25**, 326331.

277. F. Durand, C. H. Kjaergaard, E. Suraniti, S. Gounel, R. G. Hadt, E. I. Solomon and N. Mano, *Biosens. Bioelectron.*, 2012, **35**, 140-146.

278. J. P. Kallio, C. Gasparetti, M. Andberg, H. Boer, A. Loivula, K. Kruus, J. Rouvinen and N. Hakulinen, *FEBS J.*, 2011, **278**, 2283-2295.

279. J. A. Cracknell, T. P. McNamara, E. D. Lowe and C. F. Blanford, *Dalton Trans.*, 2011, **40**, 6668-6675.

280. E. I. Solomon, A. J. Augustine and J. Yoon, *Dalton Trans.*, 2008, 3921-3921.

281. C. F. Blanford, R. S. Heath and F. A. Armstrong, *Chem. Commun.*, 2007, 1710-1712.

282. K. Piontek, M. Antorini and T. Choinowski, *J. Biol. Chem.*, 2002, **277**, 37663-37669.

283. D. L. Johnson, J. L. Thompson, S. M. Brinkmann, K. A. Schuller and L. L. Martin, *Biochemistry*, 2003, **42**, 10229-10237.

284. P. Baldrian, *FEBS Microbiol. Rev.*, 2006, **30**, 215-242.

285. S. R. Couto and J. L. Toca, *Curr. Enzyme Inhib.*, 2006, **2**, 343-352.

286. F. Xu, *Biochemistry*, 1996, **35**, 7608-7614.

287. S. Tsujimura, B. Tatsumi, J. Ogawa, S. Shimizu, K. Kano and T. Ikeda, *J. Electrochem. Chem.*, 2001, **496**, 69-75.

288. N. Mano, H. H. Kim, Y. C. Zhang and A. Heller, *J. Am. Chem. Soc.*, 2002, **124**, 6480-6486.

289. N. Mano, F. Mao and A. Heller, *J. Am. Chem. Soc.*, 2003, 125, 6588-6594.

290. N. Mano, J. L. Fernandez, Y. Kim, W. Shin, A. J. Bond and A. Heller, *J. Am. Chem. Soc.*, 2003, 125, 15290-15291.

291. A. Heller, *Curr. Opin. Chem. Biol.*, 2006, **10**, 664-672.

292. J. Kim, H. F. Jia and P. Wang, *Biotechnol. Adv.*, 2006, **24**, 296-308.

293. M. J. Cooney, V. Svoboda, C. Lau, G. Martin and S. D. Martin, *Energy Environ. Sci.*, 2008, **1**, 320-337.

294. I. Willner, Y. M. Yan, B. Willner and R. Tel-Vered, *Fuel Cells*, 2009, **9**, 7-24.

295. S. A. Neto, J. C. Forti and A. R. de Andrade, *Electrocatalysis*, 2010, **1**, 87-94.

296. D. Leech, P. Kavanagh and W. Schuhmann, *Electrochim. Acta*, 2012, **84**, 223-234.

297. J. A. Cracknell, K. A. Vincent and F. A. Armstrong, *Chem. Rev.*, 2008, **108**, 2439-2461.

298. A. Heller, *Phys. Chem. Chem. Phys.*, 2004, **6**, 209-216.

299. F. A. Armstrong and J. Hirst, *Proc. Natl. Acad. Sci. U. S. A.*, 2011, **108**, 14049-14054.

300. S. D. Minteer, B. Y. Liaw and M. J. Cooney, *Curr. Opin. Biotech.*, 2007, **18**, 228-234.

301. X. Y. Yang, G. Tian, N. Jiang and B. L. Su, *Energy Environ. Sci.*, 2012, **5**, 5540-5563.

302. T. Nöll and G. Nöll, *Chem. Rev. Soc.*, 2011, **40**, 3564-3576.

303. J. Lee, J. Kim and T. Hyeon, *Adv. Mater.*, 2006, **18**, 2073-2094.

304. L. Bayne, R. V. Ulijn and P. J. Halling, *Chem. Soc. Rev.*, 2013, **42**, 9000-9010.

305. M. J. Moehlenbrock and S. D. Minteer, *Chem. Soc. Rev.*, 2008, **37**, 1188-1196.

306. R. C. Rodrigues, C. Ortiz, A. Berenguer-Murcia, R. Torres and R. Fernandez-Lafuente, *Chem. Soc. Rev.*, 2013, **42**, 6290-6307.

307. A. de Poulpiquet, A. Ciaccafava and E. Lojou, *Electrochem. Acta*, 2014, **126**, 104-114.

308. D. Leech, P. Kavanagh and W. Schuhmann, *Electrochim. Acta*, 2012, **84**, 223-234.

309. U. Hanefeld, L. Gardossi and E. Magner, *Chem. Soc. Rev.*, 2009, **38**, 453-468.

310. H. H. Kim, N. Mano, X. C. Zhang and A. Heller, *J. Electrochem. Soc.*, 2003, **150**, A209-A213.

311. N. Mano and A. Heller, *J. Electrochem. Soc.*, 2003, **150**, A1136-A1138.

312. F. Barriere, Y. Ferry, D. Rochefort and D. Leech, *Electrochem. Commun.*, 2004, **6**, 237-241.

313. S. Boland and D. Leech, *Analyst*, 2012, **137**, 113-117.

314. S. Rengaraj, P. Kavanagh and D. Leech, *Biosens. Bioelectron.*, 2011, **30**, 294-299.

315. S. Rengaraj, V. Mani, P. Kavanagh, J. Rusling and D. Leech, *Chem. Commun.*, 2011, **47**, 11861-11863.

316. P. Kavanagh and D. Leech, *Phys. Chem. Chem. Phys.*, 2013, **15**, 4859-4869.

317. F. Sato, M. Togo, M. K. Islam, T. Matsue, J. Kosuge, N. Fukasaku, S. Kurosawa and M. Nishizawa, *Electrochem. Commun.*, 2005, **7**, 643-647.

318. H. Sakai, T. Nakagawa, Y. Tokita, T. Hatazawa, T. Ikeda, S. Tsujimura and K. Kano, *Energy*. *Environ. Sci.*, 2009, **2**, 133-138.

319. J. Kim and K. H. Yoo, *Phys. Chem. Chem. Phys.*, 2013, **15**, 3510-3517.

320. S. C. Wang, F. Wang, M. Silva, A. Zarow, Y. B. Wang and Z. Iqbal, *Electrochem. Commun.*, 2009, **11**, 34-37.

321. C. Liu, S. Alwarappan, Z. F. Chen, X. X. Kong and C. Z. Li, *Biosens. Bioelectron.*, 2010, **25**, 1829-1833.

322. C. Tanne, G. Gobel and F. Lisdat, *Biosens. Bioelectron.*, 2010, **26**, 530-535.

323. J. Filip, J. Sefcovicova, P. Gemeiner and J. Tkac, *Electrochim. Acta*, 2013, **87**, 366-374.

324. X. Wu, F. Zhao, J. R. Varcoe, A. E. Thumser, C. Avignone-Rossa and R. C. T. Slade, *Biosens. Bioelectron.*, 2009, **25**, 326-331.

325. X. J. Wang, M. Falk, R. Ortiz, H. Matsumura, J. Bobacka, R. Ludwig, M. Bergelin, L. Gorton and S. Shleev, *Biosens. Bioelectron.*, 2012, **31**, 219-225.

326. D. Sokic-Lazic, R. L. Arechederra, B. L. Treu and S. D. Minteer, *Electrocatalysis*, 2010, **22**, 757-764.

327. M. J. Moehlenbrock, T. K. Toby, L. N. Pelster and S. D. Minteer, *ChemCatChem*, 2011, **3**, 561-570.

328. Z. G. Zhu, F. F. Sun, X. Z. Zhang and Y. H. P. Zhang, *Biosens. Bioelectron.*, 2012, **36**, 110-115.

329. Z. G. Zhu, T. K. Tam, F. F. Sun, C. You and Y. H. P. Zhang, *Nat. Commun.*, 2014, **5**, 3026, doi: 10.1038/ncomms4026.

330. S. Xu and S. D. Minteer, *ACS Catal.*, 2012, **2**, 91-94.

331. D. P. Hickey, F. Giroud, D. W. Schmidtke, D. T. Glatzhofer and S. D. Minteer, *ACS Catal.*, 2013, **3**, 2729-2737.

332. S. Kerzenmacher, J. Ducree, R. Zengerle and F. von Stetten, *J. Power Sources*, 2008, **182**, 1-17.

333. S. C. Barton, J. Gallaway and P. Atanassov, *Chem. Rev.*, 2004, **104**, 4867-4886.

334. M. Falk, C. W. N. Villarrubia, S. Babanova, P. Atanassov and S. Shleev, *ChemPhysChem*, 2013, **14**, 2045-2058.

335. L. Halamkova, J. Halamek, V. Bocharova, A. Szczupak, L. Alfonta and E. Katz, *J. Am. Chem. Soc.*, 2012, **134**, 5040-5043.

336. A. Szczupak, J. Halamek, L. Halamkova, V. Bocharova, L. Alfonta and E. Katz, *Energy Environ. Sci.*, 2012, **5**, 8891-8895.

337. K. MacVitte, J. Halamek, L. Halamkova, M. Southcott, W. D. Jemison, R. Lobeld and E. Katz, *Energy Environ. Sci.*, 2013, **6**, 81-86.

338. J. A. Castorena-Gonzalez, C. Foote, K. MacVitte, J. Halamek, L. Halamkova, L. A. Martinez-Lemus and E. Katz, *Electroanalysis*, 2013, **25**, 1579-1584.

339. G. T. R. Palmore, H. Bertschy, S. H. Bergens and G. M. Whitesides, *J. Electroanal. Chem.*, 1998, **443**, 155-161.

340. P. K. Addo, R. L. Arechederra and S. D. Minteer, *Electroanalysis*, 2010, **22**, 807-812.

341. N. L. Akers, C. M. Moore and S. D. Minteer, *Electrochim. Acta*, 2005, **50**, 2521-2525.

342. S. Topcagic and S. D. Minteer, *Electrochim. Acta*, 2006, **51**, 2168-2172.

343. L. Deng, L. Shang, D. Wen, J. F. Zhai and S. J. Dong, *Biosens. Bioelectron.*, 2010, **26**, 70-73.

344. J. C. Forti, S. A. Neto, V. Zucolotto, P. Ciancaglini and A. R. de Andrade, *Biosens. Bioelectron.*, 2011, **26**, 2675-2679.

345. R. L. Arechederra, B. L. Treu and S. D. Minteer, *J. Power Sources*, 2007, **173**, 156-161.

346. R. L. Arechederra and S. D. Minteer, *Fuel cells*, 2009, **9**, 63-69.

347. K. A. Vincent, J. A. Cracknell, J. R. Clark, M. Ludwig, O. Lenz, B. Friedrich and F. A. Armstrong, *Chem. Commun.*, 2006, 5033-5035.

348. A. F. Wait, A. Parkin, G. M. Morley, L. dos Santos and F. A. Armstrong, *J. Phys. Chem. C*, 2010, **114**, 12003-12009.

349. S. Krishnan and F. A. Armstrong, *Chem. Sci.*, 2012, 3, 1015-1023.

350. A. Cornish-Bowden, *Fundamentals of enzyme kinetics (4th edition)*, Weinheim: Wiley, 2012.

351. V. Schroder, B. Emonts, H. Janssen and H. P. Schulze, *Chem. Eng. Technol.*, 2004, **27**, 847-851.

352. A. Ciaccafava, A. de Poulpiquet, V. Techer, M. T. Giudici-Orticoni, S. Tingry, C. Innocent and E. Lojou, *Electrochem. Commun.*, 2012, **23**, 25-28.

353. L. Xu and F. A. Armstrong, *Energy Environ. Sci.*, 2013, **6**, 2166-2171.

354. W. J. Gao, Y. Wan, Y. Q. Dou and D. Y. Zhao, *Adv. Energy Mater.*, 2011, **1**, 115-123.

355. Y. P. Zhai, Y. Q. Dou, D. Y. Zhao, P. F. Fulvio, R. T. Mayes and S. Dai, *Adv. Mater.*, 2011, **23**, 4828-4850.

356. Y. M. Yan, W. Zheng, L. Su and L. Q. Mao, *Adv. Mater.*, 2006, **18**, 2639-2643.

357. F. Gao, L. Viry, M. Maugey, P. Poulin and N. Mano, *Nat. Commun.*, 2010, 1:2 doi: 10.1038/ncomms1000.

358. T. Miyake, S. Yoshino, T. Yamada, K. Hata and M. Nishizawa, *J. Am. Chem. Soc.*, 2011, **133**, 5129-5134.

359. V. Flexer, N. Brun, R. Backov and N. Mano, *Energy. Environ. Sci.*, 2010, **3**, 1302-1306.

360. V. Flexer, N. Brun, O. Courjean, R. Backov and N. Mano, *Energy. Environ. Sci.*, 2011, **4**, 2097-2106.

361. L. Deng, F. Wang, H. J. Chen, L. Shang, L. Wang, T. Wang and S. J. Dong, *Biosens. Bioelectron.*, 2008, **24**, 329-333.

362. K. Murata, K. Kajiya, N. Nakamura and H. Ohno, *Energy. Environ. Sci.*, 2009, **2**, 1280-1285.

363. O. Yehezkeli, R. Tel-Vered, S. Reichlin and I. Willner, *ACS Nano*, 2011, **5**, 2385-2391.

364. Y. Liu, M. K. Wang, F. Zhao, B. F. Liu and S. J. Dong, *Chem.-Eur. J.*, 2005, **11**, 4970-4974.

365. P. Cinquin, C. Gondran, F. Giroud, S. Mazabrard, A. Pellissier, F. Boucher, J. P. Alcaraz, K. Gorgy, F. Lenouvel, S. Mathe, P. Porcu and S. Cosnier, *PLoS One*, 2010, **5**, No. e10476.

366. A. Zebda, C. Gondran, A. Le Goff, M. Holzinger, P. Cinquin and S. Cosnier, *Nat. Commun.*, 2011, 2:370 doi: 10.1038/ncomms1365.

367. C. S. Kong, D. Y. Kim, H. K. Lee, Y. G. Shul and T. H. Lee, *J. Power Sources*, 2002, **108**, 185-191.

368. K. S. W. Sing, *Pure Appl. Chem.*, 1982, **54**, 2201-2218.

369. Y. G. Guo, J. S. Hu and L. J. Wan, *Adv. Mater.*, 2008, **20**, 2878-2887.

370. A. Ermete, *Appl. Catal. B – Environ.*, 2009, **88**, 1-24.

371. D. Bell, *Fundamentals of electric circuits (7th edition)*, Oxford: Oxford University Press, 2009.

372. P. Aelterman, K. Rabaey, H. T. Pham, N. Boon and W. Verstraete, *Environ. Sci. Technol.*, 2006, **40**, 3388-3394.

373. I. Ieropoulos, J. Greenman and C. Melhuish, *Int. J. Energy Res.*, 2008, **32**, 1228-1240.

374. Y. Kim, M. C. Hatzell, A. J. Hutchinson and B. E. Logan, *Energy Environ. Sci.*, 2011, **4**, 4662-4667.

375. S. J. Andersen, I. Pikaar, S. Freguia, B. C. Lovell, K. Rabaey and R. A. Rozendal, *Environ. Sci. Technol.*, 2013, **47**, 5488-5494.

376. S.H. Shin, Y. Choi, S. H. Na, S. Jung and S. Kim, *Bull. Korean Chem. Soc.*, 2006, **27**, 281-285.

377. A. Dekker, A. T. Heijne, M. Saakes, H. V. M. Hamelers and C. J. N. Buisman, *Environ. Sci. Technol.*, 2009, **43**, 9038-9042.

378. D. Kim, J. An, B. Kim, J. K. Jang, B. H. Kim and I. S. Chang, *ChemSusChem*, 2012, **5**, 1086-1091.

379. J. An, B. Kim, J. K. Jang, H. S. Lee and I. S. Chang, *Biosens. Bioelectron.*, 2014, **59**, 28-34.

380. Y. Zuo, S. Cheng, D. Call and B. E. Logan, *Environ. Sci. Technol.*, 2007, **41**, 3347-3353.

381. L. Zhuang and S. Zhou, *Electrochem. Commun.*, 2009, **11**, 937-940.

382. J. R. Kim, J. Rodriguez, F. R. Hawkes, R. M. Dinsdale, A. J. Guwy and G. C. Premier, *Energy Environ. Sci.*, 2011, **4**, 459-465.

383. L. Zhuang, Y. Zheng, S. Zhou, Y. Yuan, H. Yuan and Y. Chen, *Bioresource Technol.*, 2012, **106**, 82-88.

384. L. Zhuang, Y. Yuan, Y. Wang and S. Zhou, *Bioresource Technol.*, 2012, **123**, 406-412.

385. C. F. Blanford and F. A. Armstrong, *J. Solid State Electrochem.*, 2006, **10**, 826-832.

386. P. Scherz and S. Monk, *Practical electronics for inventors (3rd edition)*, New York: McGraw Hill, 2013.

387. K. J. Laidler and J. M. Meiser, *Physical Chemistry*, Menlo Park: Benjamin/Cummings Publishing, 1982.

388. D. R. Lide, *CRC Handbook of Chemistry and Physics (86th edition)*, Boca Raton: CRC Press, 2005.